MAX-PLANCK-INSTITUT FÜR QUANTENOPTIK

Coulomb Explosion and Intense-Field Photodissociation of Ion-Beam H_2^+ and D_2^+

Domagoj Pavičić

MPQ-Report
295

MPQ 295 Juli 2004

Dieser MPQ Bericht ist als Manuskript des Autors gedruckt
Alle Rechte vorbehalten

This MPQ Report has been printed as author's manuscript
All rights reserved

Max Planck Institut für Quantenoptik
85748 Garching, Bundesrepublik Deutschland

To my parents,
my brother
and
Helena

Abstract

As the simplest molecule in nature, the hydrogen molecular ion provides a unique system for studying molecules in intense laser fields. In this thesis, the Coulomb explosion and photodissociation channel of H_2^+ and D_2^+ have been investigated with 790-nm, sub-100-fs laser pulses by employing a high-resolution photofragment imaging technique. Unlike most experiments, where neutral molecules were used as a target, in this work molecular ions were prepared by an electric discharge, providing well-defined starting conditions and allowing experiments at lower intensities.

At intensities close to the threshold for Coulomb explosion ($<10^{14}$ W/cm^2), we observed a peak structure in the Coulomb explosion kinetic energy spectra in both H_2^+ and D_2^+. We show that the observed peaks can be attributed to the different dissociation energies of vibrationally excited molecules. Furthermore, this preservation of the vibrational structure during the Coulomb explosion suggests ionization at one well-defined critical internuclear distance. Moreover, when using pulses with durations of 200–500 fs, we found three Coulomb explosion kinetic energy groups with different angular distributions in both molecular ions. The groups in D_2^+ at a pulse duration of 350 fs and an intensity of 1×10^{14} W/cm^2 strongly suggest critical internuclear distances of 8, 11 and 15 a.u.

In the one-photon photodissociation study of D_2^+ at intensities below 2×10^{14} W/cm^2, we obtained vibrationally resolved fragment velocity distributions. With increasing intensity, we observed the effects of bond softening – narrowing of the angular distributions and vibrational level shifting. These effects were also found in H_2^+ and are in agreement with the model of light-induced potentials. In addition, in the kinetic energy spectra of D_2^+, we found the smaller widths of the vibrational peaks, which we interpret as being due to the longer lifetimes of the vibrational states of D_2^+ against photodissociation. Moreover, we observed fragments with near-zero kinetic energies with broad angular distributions, indicating dissociation through a vibrational trapping mechanism. In the two-photon bond softening process (above-threshold dissociation) of H_2^+, we identified fragments from the single vibrational level $v = 3$. At higher intensities, lower-energy fragments with increasing alignment were observed, suggesting dissociation of the levels $v < 3$ through the barrier lowering mechanism.

These results provide a basis for quantum mechanical simulations that could lead to a better understanding of the molecular dynamics in intense fields.

Zusammenfassung

Das elementarste Molekül in der Natur, das Wasserstoff-Molekülion, stellt ein einzigartiges System für die Untersuchung von Molekülen in intensiven Laserfeldern dar. In dieser Dissertation wurden die Coulomb-Explosion und die Photodissoziation des H_2^+ und D_2^+ mit 790-nm, sub-100-fs Laserpulsen unter Verwendung einer hochauflösenden Photofragment Abbildungstechnik untersucht. Im Gegensatz zu den meisten Experimenten, in denen neutrale Moleküle als Ausgangsmoleküle benutzt wurden, wurden in dieser Arbeit die Molekülionen durch eine elektrische Gasentladung erzeugt, was zu wohldefinierten Ausgangsbedingungen führte und Experimente mit relativ niedrigen Laserintensitäten ermöglichte.

Bei Intensitäten nahe der Schwelle der Coulomb-Explosion ($<10^{14}$ W/cm^2), beobachten wir eine Peak-Struktur in den kinetischen Energiespektren der Fragmente der Coulomb-Explosion sowohl bei H_2^+ als auch bei D_2^+. Wir stellen fest, dass die beobachteten Peaks den unterschiedlichen Dissoziationsenergien der vibrationsangeregten Moleküle zugeordnet werden können. Die Erhaltung der Vibrationsstruktur bei der Coulomb-Explosion deutet darauf hin, dass die Ionisation bei einem scharfen kritischen internuklearen Abstand stattfindet. Als wir Laserpulse mit einer Dauer von 200–500 fs verwendeten, entdeckten wir drei Coulomb-Explosions Zentren in den kinetischen Energiespektren mit unterschiedlichen Winkelverteilungen bei beiden molekularen Isotopomeren. So entsprechen die Gruppen bei D_2^+ bei einer Pulsdauer von 350 fs und einer Intensität von 1×10^{14} W/cm^2 kritischen internuklearen Abständen von 8, 11 und 15 a.u.

Bei der Untersuchung der 1-Photonen Photodissoziation des D_2^+ beobachten wir bei einer Intensität unterhalb 2×10^{14} W/cm^2 vibrationsaufgelöste Geschwindigkeitsverteilungen der Fragmente. Mit zunehmender Intensität beobachten wir auch Effekte des bond softenings – Einengung der Winkelverteilung und Verschiebung der Vibrationsniveaus. Diese Effekte wurden auch schon vorher bei H_2^+ beobachtet und finden ihre Erklärung in dem Modell der lichtinduzierten Potenziale. Insbesondere finden wir in den kinetischen Energiespektren von D_2^+ kleinere Breiten der Vibrationspeaks, deren Ursache längere Lebensdauern der Vibrationszustände von D_2^+ bei der Photodissoziation sein sollten. In dem Prozess des 2-Photonen bond softenings von H_2^+ identifizieren wir Fragmente des einzelnen Vibrationsniveaus $v = 3$. Bei höheren Intensitäten wurden niederenergetische Fragmente mit zunehmender Ausrichtung in Polarisationsrichtung beobachtet, die auf Dissozation durch eine Barriereabsenkung hinweisen.

Diese experimentellen Ergebnisse können durch quantenmechanische Rechnungen simuliert werden, die zu einem besseren Verständnis der Molekulardynamik in intensiven Laserfeldern führen werden.

Contents

Abstract vii

Zusammenfassung ix

1 Introduction 1

2 H_2^+ in intense laser fields 5
2.1 Photodissociation in intense laser fields 5
2.1.1 Theoretical approaches 5
2.1.2 Floquet picture 7
2.1.3 Bond softening, trapping and above-threshold dissociation 12
2.1.4 Molecular alignment 13
2.2 Strong-field ionization and Coulomb explosion 13
2.2.1 Photoionization mechanisms 13
2.2.2 Semiclassical model of enhanced ionization 16
2.2.3 Charge-resonant enhanced ionization (CREI) 17

3 Experimental 19
3.1 Ion beam apparatus 19
3.1.1 Ion source 20
3.1.2 Mass selection 22
3.1.3 Ion optics 22
3.1.4 Ion current 24
3.1.5 Detection system 25
3.1.6 Data acquisition 26
3.1.7 Collimation of the ion beam 28
3.1.8 Vacuum system 30
3.2 Imaging of fragments 30
3.2.1 Principle of fragment imaging 31
3.2.2 Inverse Abel transform 33
3.2.3 Comparison of inversion algorithms 33
3.2.4 Velocity and energy resolution 35
3.3 Femtosecond laser system 37

3.3.1 Laser setup . . . 37
3.3.2 Beam and pulse characterization . . . 40
3.3.3 Laser intensity . . . 45
3.4 Intensity distribution in the interaction region . . . 45
3.4.1 Interaction volume . . . 45
3.4.2 Contribution of the intensity shells to the measured signal . . . 48

4 Photodissociation of the deuterium molecular ion **51**
4.1 Vibrationally resolved velocity distributions . . . 51
4.2 Kinetic energy distributions of the fragments . . . 53
4.3 Angular distributions of the fragments . . . 58
4.3.1 One-photon bond softening . . . 58
4.3.2 Vibrational trapping and two-photon bond softening . . . 61
4.4 Comparison with measurements on H_2^+ at lower intensities . . . 64

5 Photodissociation of the hydrogen molecular ion **69**
5.1 Fragment velocity and kinetic energy distributions . . . 69
5.2 Angular distributions of the fragments: alignment . . . 77
5.2.1 Dependence on the peak laser intensity . . . 77
5.2.2 Angular distributions of the one- and net two-photon processes . . . 78
5.3 Fragment yields of the one- and the net two-photon process . . . 81

6 Coulomb explosion **85**
6.1 Measurements with sub-100-fs pulses . . . 86
6.1.1 Mechanism of Coulomb explosion . . . 86
6.1.2 Coulomb explosion at near-threshold intensities . . . 91
6.2 Measurements with pulses of longer durations . . . 99
6.3 Fragment yield of the Coulomb explosion channel . . . 105

7 Conclusion and perspectives **107**

A Unit conversion **109**

B Molecular data on H_2^+ and D_2^+ **111**
B.1 Constants . . . 111
B.2 Energies and populations of vibrational levels . . . 111

List of symbols and acronyms **115**

Bibliography **117**

Acknowledgments **127**

Chapter 1

Introduction

Over the past century, understanding of interaction of light with matter has been one of the central themes of research in physics. Early investigations of emission and absorption spectra of atoms and molecules have already provided a wealth of knowledge about their electronic structure. With the availability of coherent and monochromatic laser radiation and development of high-resolution laser spectroscopy techniques, our knowledge of the structure of atoms and molecules has been revolutionized.

Moreover, the advent and continued development of pulsed lasers also made it possible to investigate ultrafast dynamical processes in different systems, ranging from small molecules to complex biological systems. Using the pump-probe technique with ultrashort laser pulses, one can monitor molecular motion (such as vibrations, or making and breaking of molecular bonds) occurring on the femtosecond timescale (1 femtosecond = 10^{-15} s). This concept has led to the birth of femtochemistry, for which the 1999 Nobel Prize in chemistry was awarded to Ahmed Zewail [1].

Recent progress in ultrafast optics has made available laser pulses as short as a few femtoseconds in the visible spectral range [2]. Since such pulse durations are limited by the oscillation period of the electromagnetic field in the pulse, generation of shorter pulses requires coherent sources of higher-frequency radiation. High-order harmonics of the fundamental laser radiation generated in noble gas atoms can provide coherent radiation in the extreme ultraviolet (XUV) and soft x-ray range (e.g., [3]). Recently, such radiation has been successfully used for generating trains of pulses with durations in the attosecond range (1 attosecond = 10^{-18} s) [4, 5]. Single, isolated attosecond pulses [6] have already been applied to time-resolved spectroscopy of atomic inner-shell electrons [7]. Simultaneously, theoretical and experimental efforts have been made to characterize the duration of attosecond XUV pulses [8–12].

Few-cycle pulses in the optical range have also provided evidence that laser-matter interaction is sensitive to the phase of the oscillating laser electric field with respect to the pulse envelope [13]. Nowadays, intense few-cycles pulses with stabilized carrier-envelope phase can readily be generated [14] and the phase can be accurately determined [15]. This permits directed emission and steering of the electron wave packets on the sub-femtosecond timescale.

In addition to short pulse durations, femtosecond laser pulses are characterized by high peak intensities. At present, laboratory-scale lasers can deliver pulses shorter than 10 fs with peak powers in the terawatt (1 terawatt = 10^{12} W) range at a kilohertz repetition rate [16]. By focusing such pulses it is possible to investigate a variety of intense-field phenomena in atoms, molecules, clusters, plasmas and solid materials occurring in the intensity range of $10^{13} - 10^{18}$ W/cm^2 (e.g., [3, 17, 18]).

Most of the attention to strong field-matter interaction has been concentrated on atoms. At an intensity of about 10^{16} W/cm^2, the laser electric field strength becomes of the same magnitude as the field binding a 1s electron in a hydrogen atom (known as atomic unit of electric field, 5×10^9 V/cm). At these and already at lower intensities, light-atom interaction is so strong that normal perturbative approaches break down, leading to novel phenomena collectively termed as multiphoton processes. These processes include above-threshold ionization (ATI) — absorption of more photons than the minimum number required for ionization [19], non-sequential or direct double ionization — simultaneous emission of more electrons [20, 21] and high harmonic generation [22, 23].

In addition to the effects observed in atoms, molecules in strong fields exhibit new phenomena associated with additional vibrational and rotational degrees of freedom. In 1990, Bucksbaum *et al* found that the molecular bond is softened by strong laser fields, resulting in photodissociation of the molecules in strongly bound vibrational states [24]. The same study also revealed that molecules can absorb more photons than necessary for dissociation, which, by analogy with ATI, is termed above-threshold dissociation (ATD) [25]. The theoretically predicted effects of bond hardening or trapping in the potentials induced by the laser fields [26] were recently observed [27, 28]. Alignment of molecules by strong laser fields has also been extensively studied [29–32].

Besides photodissociation, ionization dynamics of molecules in strong laser fields has attracted great interest. Early experiments showed that the kinetic energies of the charged nuclear fragments formed after ionization are significantly smaller than had been expected, assuming that ionization and Coulomb repulsion occur at the equilibrium internuclear separation [33]. The solution was offered by several models [34–36], predicting that this Coulomb explosion takes place at large internuclear separations through charge-resonance enhanced ionization (CREI) [36]. This model found high ionization rates at particular, so-called critical, internuclear separations. Despite the numerous experiments carried out, there has hitherto been no clear evidence of the existence of critical distances.

Much attention has been focused on the role of re-collision of the ionized electron with the parent ion [37]. Recent experiments have shown that non-sequential double ionization in atoms and molecules is caused by such re-scattered electrons [21, 38]. As a consequence, Coulomb explosion protons with high kinetic energies are produced [39, 40]. The correlation between nuclear and re-colliding electron wave packets was successfully exploited to probe molecular dynamics with attosecond resolution [41].

The simplest molecule in nature is the hydrogen molecular ion, consisting of two protons bound by an electron. As a model system, H_2^+ is of fundamental importance for understanding the physics of molecules as well as atomic clusters in intense laser fields. Though the dissociation and ionization dynamics of H_2^+ have been extensively studied theoretically (e.g., [26, 42]), there is only limited experimental insight into them. Because of the difficulties involved in preparing H_2^+, nearly all experiments to date have used H_2 and its isotopic variant D_2 as primary target [42]. The molecular ions have thus been produced by ionizing the neutral molecules by the same laser pulse as used for molecular ion–laser interaction. The interplay between the first ionization step and the later ionization and dissociation dynamics of H_2^+ has hindered clear interpretation of the experimental results [26]. Moreover, the phenomena occurring at intensities below 10^{14} W/cm^2 were not accessible owing to the relatively high intensities required for ionization of H_2. Intense-field effects in H_2^+ have been investigated only in two recent experiments employing fast ion beams [28, 43].

The photofragment velocity distributions of Sändig *et al* [28] neatly demonstrated the effects of strong fields for molecules in single vibrational levels. Molecular bond softening was manifested in the appearance of fragments from lower-lying vibrational states with increasing intensity, their alignment along the laser polarization axis and shifting towards lower kinetic energies with respect to the weak-field case. This experiment was, however, limited to study of the photodissociation process at relatively moderate intensities below about 10^{14} W/cm^2.

In this thesis, intense-field photodissociation and Coulomb explosion of H_2^+ and D_2^+ are studied. The main objective of this work is to investigate the Coulomb explosion channel in H_2^+ with the aim of elucidating the question of the existence of critical distances in enhanced ionization. Molecular ions in fast beams were used [28], allowing investigation at intensities close to the threshold for this process. A high-resolution fragment imaging method was employed, yielding direct information about both the kinetic energy and angular distribution of the photofragments. Furthermore, the photodissociation channel in H_2^+ is studied at intensities above 10^{14} W/cm^2 in order to investigate the mechanisms of one- and two-photon bond softening.

Finally, photodissociation of D_2^+ is investigated at the intermediate intensity range with the intention of obtaining vibrationally resolved velocity distributions of the fragments. Together with measurements on H_2^+ at similar intensities [28], such an experiment can provide valuable insights into the role of isotope effects in photodissociation. This part of the study is also motivated by recent theoretical simulations of the experimental results on H_2^+ [44, 45]. Similar calculations on D_2^+ would add to our understanding of the dynamics of single vibrational levels in strong laser fields. The third isotopic variant, HD^+, has also been studied, these results being presented in the framework of the diploma thesis of Kiess [46].

The thesis is organized as follows. Chapter 2 gives the theoretical background for interpretation of the results. In Chapter 3, various aspects of the experiment are discussed. Chapter 4 presents the study of photodissociation of D_2^+ at the intermediate intensities. In Chapter 5, photodissociation of H_2^+ at higher intensities is investigated. In Chapter 6, the Coulomb explosion channel in H_2^+ and D_2^+ is explored. Finally, in Chapter 7, the conclusion and perspectives for future work are given.

Chapter 2

H_2^+ in intense laser fields

This chapter presents the theoretical background that provides a basis for understanding of the experimental results. Section 2.1 deals with the mechanism of photodissociation of H_2^+ in intense laser fields. First, a definition of a strong field is given and different theoretical approaches used to describe H_2^+ in intense fields are discussed. Here, a picture of molecular "dressed" states is presented, which leads to an intuitive description of the light-molecule system in terms of light-induced potential curves. Predicted effects such as molecular bond softening, vibrational trapping and above-threshold dissociation will be described, as well as geometric and dynamic alignment. At laser intensities beyond 10^{14} W/cm^2, the dissociation process is increasingly accompanied by molecular ionization followed by Coulomb explosion of the nuclei. This mechanism of fragmentation is discussed in Section 2.2. First, a simple semiclassical model of ionization is given, which can explain the kinetic energies of the fragments that were observed in experiments. The results of quantum mechanical calculations predicting ionization at particular, so-called critical internuclear distances are presented in the last section.

2.1 Photodissociation in intense laser fields

2.1.1 Theoretical approaches

The interaction of laser radiation with the simplest molecular system H_2^+ can be described within different frameworks. Some extensive reviews of theoretical methods describing H_2^+ in intense laser fields can be found in references [47, 42, 26]. Most of the approaches are valid only in a certain range of parameters characterizing the radiation field, such as intensity, wavelength and pulse duration. In this section, different regimes specified by these parameters will be discussed.

At low intensities the interaction can be described by using perturbation theory. In this regime the dissociation rate is proportional to laser intensity, what is known as Fermi's golden rule (e.g., [48]). At higher laser intensities, multiphoton processes take place, resulting in various nonlinear effects. These intensity regimes can be characterized with the Rabi

frequency ω_R (see, e.g., [49, 47]), which measures the strength of the radiative coupling:

$$\hbar\omega_R\,[\mathrm{cm}^{-1}] = \boldsymbol{E_0}\cdot\boldsymbol{d} = 1.17\times10^{-3}\sqrt{I\,[\mathrm{W/cm}^2]}\;d\,[\mathrm{a.u.}]\,, \tag{2.1}$$

$$I = \frac{1}{2}\,c\varepsilon_0 E_0^2\,. \tag{2.2}$$

Here $\boldsymbol{d}$ is the transition dipole moment in atomic units (a.u.) and E_0 is the amplitude of the electric field $\boldsymbol{E}(t) = \boldsymbol{E_0}\cos(\omega t)$, which is related to intensity I via Eq. (2.2). The classification between strong- and weak-coupling regime can be specified by comparing the Rabi frequency with the frequency of the nuclear vibrational motion, ω_v.

In the case of H_2^+, the radiation couples the two lowest electronic states: the attractive ground state $1s\sigma_g$ and the repulsive first excited state $2p\sigma_u$. These states are illustrated in Fig. 2.1 with potential curves $V_g(R)$ and $V_u(R)$, where R denotes the internuclear separation. Energetically higher states will not be considered here since they lie more than 11 eV higher in energy, which is much larger than the photon energy of 1.6 eV corresponding to the wavelength of 790 nm, which was used in the experiment. The two lowest states are resonantly coupled at an internuclear distance of 4.8 a.u. If the Rabi transition frequency is small compared to the vibrational frequency ω_v, the probability of the molecule to absorb a photon during the time spent near the resonance will be low. On the other hand, in the case of $\omega_R \gg \omega_v$, the molecule will very probably absorb a photon from the radiation field when it approaches the resonance. The Franck-Condon factor for this transition is largest for the vibrational level $v = 9$, since the outer turning point almost coincides with the resonant internuclear separation. The vibrational energy $\hbar\omega_v$ of this level is approximately 1200 cm^{-1} (~0.3 eV) [1], with the vibrational period of 29 fs (Section 4.2). The Rabi frequency approaches the vibrational frequency at an intensity of 10^{11} W/cm^2, for which $\hbar\omega_R$ is about 800 cm^{-1} (according to Eq. (2.1) using the dipole moment $d = 2.3$ a.u. [50]). Thus, at intensities $I > 10^{11}$ W/cm^2, the perturbation theory is no longer applicable and different approaches must be used. When only a few states are coupled by radiation, as in H_2^+, a useful description can be obtained applying the Floquet or molecular "dressed" state formalisms [51, 47], which describe the molecule-light system in terms of new light-induced molecular potentials [52–54].

Considering the duration of laser pulses, the methods can be divided into time-dependent and time-independent ones. For laser pulses long on the timescale of the molecular vibrational motion and the dissociation process, which is on the order of 10 fs, the evolution of the system can be considered as adiabatic. In this case, time-independent methods, such as the Floquet approach, may be employed. For ultrashort pulses in the femtosecond regime, the laser intensity varies on the timescale of molecular motion, and hence time-dependent methods must be used. Most of the calculations nowadays use wave packet propagation methods based on direct integration of the time-dependent Schrödinger equation.

[1] Traditionally, the energies E of states are expressed in units of wave numbers according to the relation $E/(hc) = 1/\lambda$. In this work energies will be given in electronvolts (1 eV = 8065.5 cm^{-1}).

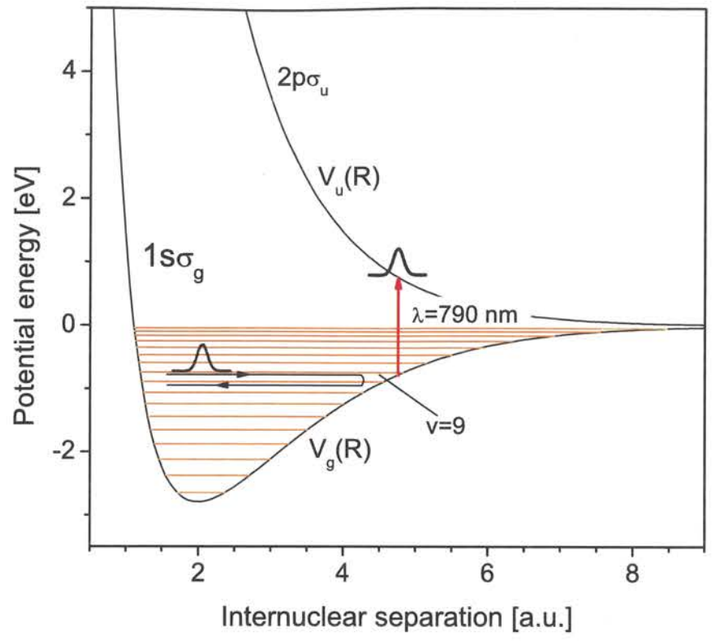


Figure 2.1: The two lowest electronic states of H_2^+ coupled by laser radiation centered at a wavelength of 790 nm. The Franck-Condon factor is maximal for the vibrational level $v = 9$ at an internuclear separation of 4.8 a.u.

The frequency of the laser radiation becomes more important in processes involving the electron motion. Its influence on the ionization process will be discussed in Section 2.2.1.

Although the methods based on the time-dependent Schrödinger equation lead to more accurate results, in this work the Floquet method will be preferred, since it offers a more intuitive description of the physical phenomena in strong fields.

2.1.2 Floquet picture

The time-dependent Schrödinger equation for a molecular system in the light field is

$$H(\boldsymbol{r}, R, t)\Psi(\boldsymbol{r}, R, t) = \mathrm{i}\hbar\frac{\partial}{\partial t}\Psi(\boldsymbol{r}, R, t)\,, \tag{2.3}$$

where $\boldsymbol{r}$ denotes the electronic coordinate and R is the internuclear separation. The total Hamiltonian $H(\boldsymbol{r}, R, t)$ consists of the time-independent field-free Hamiltonian $H_0(\boldsymbol{r}, R)$ and the interaction term $V(\boldsymbol{r}, t)$ [55]:

$$H(\boldsymbol{r}, R, t) = H_0(\boldsymbol{r}, R) + V(\boldsymbol{r}, t)\,, \tag{2.4}$$

$$H_0(\boldsymbol{r}, R) = T_R + H_{el}(\boldsymbol{r}, R)\,, \tag{2.5}$$

where T_R is the nuclear kinetic energy operator and H_{el} is the electronic Hamiltonian.

For a linearly polarized monochromatic electric field $\boldsymbol{E}(t) = \boldsymbol{e_z} E_0 \cos(\omega t)$ the interaction in the dipole approximation is equal to

$$V(\boldsymbol{r}, t) = -e\boldsymbol{r} \cdot \boldsymbol{E}(t) = \frac{eE_0 z}{2}\left(\mathrm{e}^{\mathrm{i}\omega t} + \mathrm{e}^{-\mathrm{i}\omega t}\right) = V_- \,\mathrm{e}^{\mathrm{i}\omega t} + V_+ \,\mathrm{e}^{-\mathrm{i}\omega t}\,, \tag{2.6}$$

where $e\boldsymbol{r}$ is the dipole moment. Here it was assumed that the molecule is perfectly aligned with the laser electric field.

Since the only time dependence comes from the interaction term $V(\boldsymbol{r}, t)$, the total Hamiltonian is periodic in time $H(t) = H(t+T)$ with the period $T = 2\pi/\omega$. According to the Floquet theorem [55, 56], the solutions can then be written in the form

$$\Psi(\boldsymbol{r}, R, t) = \mathrm{e}^{\mathrm{i}Et/\hbar} F(\boldsymbol{r}, R, t)\,, \tag{2.7}$$

where E is called quasi-energy. The function $F(\boldsymbol{r}, R, t)$ is periodic with period T, thus it can be expanded in the Fourier series

$$F(\boldsymbol{r}, R, t) = \sum_{n=-\infty}^{n=+\infty} \mathrm{e}^{-\mathrm{i}n\omega t} F_n(\boldsymbol{r}, R)\,. \tag{2.8}$$

Using Eqs. (2.7) and (2.8), the wave function now reads

$$\Psi(\boldsymbol{r}, R, t) = \mathrm{e}^{\mathrm{i}Et/\hbar} \sum_{n=-\infty}^{n=+\infty} \mathrm{e}^{-\mathrm{i}n\omega t} F_n(\boldsymbol{r}, R)\,. \tag{2.9}$$

Inserting the Floquet Ansatz (2.9) into the Schrödinger equation (2.3), and using Eqs. (2.4) and (2.6), the time-dependent Schrödinger equation is transformed into a set of time-independent differential equations, in which neighbouring Fourier components are coupled:

$$[E + n\hbar\omega - H_0(\boldsymbol{r}, R)]\, F_n(\boldsymbol{r}, R) = V_+ \, F_{n-1}(\boldsymbol{r}, R) + V_- \, F_{n+1}(\boldsymbol{r}, R)\,. \tag{2.10}$$

The wave functions $F_n(\boldsymbol{r}, R)$ are solutions of the field-free Hamiltonian H_0, which are now "dressed" with the phase factors $\mathrm{e}^{-\mathrm{i}n\omega t}$. For the fixed nuclei ($T_R = 0$), the field-free Hamiltonian is equal to the electronic Hamiltonian. Hence, for H_2^+ the functions $F_n(\boldsymbol{r}, R)$ are the wave functions $\Phi_g(\boldsymbol{r}, R)$ and $\Phi_u(\boldsymbol{r}, R)$ of the electronic states $1s\sigma_g$ and $2p\sigma_u$, respectively:

$$\begin{aligned} H_{el}(\boldsymbol{r}, R)|\Phi_{g,n}(\boldsymbol{r}, R)\rangle &= V_g(R)|\Phi_{g,n}(\boldsymbol{r}, R)\rangle \\ H_{el}(\boldsymbol{r}, R)|\Phi_{u,m}(\boldsymbol{r}, R)\rangle &= V_u(R)|\Phi_{u,m}(\boldsymbol{r}, R)\rangle\,. \end{aligned} \tag{2.11}$$

From Eq. (2.9) it is clear that identical solutions exist for quasi-energies E, $E \pm \hbar\omega$, $E \pm 2\hbar\omega$, etc. The field-free solutions $F_n(\boldsymbol{r}, R)$, that is $\Phi_g(\boldsymbol{r}, R)$ and $\Phi_u(\boldsymbol{r}, R)$, can be interpreted

as being "dressed" with n photons of the radiation field and are labelled in Eq. (2.11) with indices n. Such dressed states are illustrated in Fig. 2.2(a) and are called adiabatic potential curves. With this interpretation, V_+ in Eq. (2.10) is responsible for one-photon absorption and V_- for emission of one photon. Since only the states of different symmetry can be coupled, i.e., $g \leftrightarrow u$, the neighbouring functions with indices n and $n \pm 1$ in Eq. (2.10) must correspond to different electronic states, as shown in Fig. 2.2(a). Taking this into account, Eq. (2.10) becomes

$$\begin{aligned} [E + n\hbar\omega - V_g(R)]\,|\Phi_{g,n}(\boldsymbol{r}, R)\rangle &= V_+|\Phi_{u,n-1}(\boldsymbol{r}, R)\rangle + V_-|\Phi_{u,n+1}(\boldsymbol{r}, R)\rangle \\ [E + (n+1)\hbar\omega - V_u(R)]\,|\Phi_{u,n+1}(\boldsymbol{r}, R)\rangle &= V_+|\Phi_{g,n}(\boldsymbol{r}, R)\rangle + V_-|\Phi_{g,n+2}(\boldsymbol{r}, R)\rangle\,. \end{aligned} \tag{2.12}$$

Light-induced potential curves

The infinite set of differential equations (2.12) can be written as a matrix and the quasi-energies are then obtained by diagonalizing the matrix

$$\begin{bmatrix} & \vdots & \vdots & \vdots & \vdots & \\ \cdots & V_{gu}(R) & 0 & 0 & 0 & \cdots \\ \cdots & V_u(R) - (n-1)\hbar\omega & V_{gu}(R) & 0 & 0 & \cdots \\ \cdots & V_{gu}(R) & V_g(R) - n\hbar\omega & V_{gu}(R) & 0 & \cdots \\ \cdots & 0 & V_{gu}(R) & V_u(R) - (n+1)\hbar\omega & V_{gu}(R) & \cdots \\ \cdots & 0 & 0 & V_{gu}(R) & V_g(R) - (n+2)\hbar\omega & \cdots \\ \cdots & 0 & 0 & 0 & V_{gu}(R) & \cdots \\ & \vdots & \vdots & \vdots & \vdots & \end{bmatrix} \tag{2.13}$$

, where

$$V_{ug}(R) = V_{gu}(R) \equiv \langle 2p\sigma_u|V_\pm|1s\sigma_g\rangle = \frac{E_0}{2}\langle 2p\sigma_u|ez|1s\sigma_g\rangle = \frac{\hbar\omega_R}{2}\,. \tag{2.14}$$

In practical calculations matrix (2.13) must be truncated to a finite one. The smallest matrix consists of a single 2×2 Floquet block. The eigenvalues are in this case obtained by solving the equation

$$\begin{vmatrix} V_g(R) - E & V_{gu}(R) \\ V_{gu}(R) & V_u(R) - \hbar\omega - E \end{vmatrix} = 0\,, \tag{2.15}$$

where for simplicity the photon number n in Eq. (2.13) was set to zero. The results are so-called adiabatic potential curves $E_-(R)$ and $E_+(R)$:

$$E_\pm(R) = \frac{V_g(R) + V_u(R) - \hbar\omega}{2} \pm \frac{1}{2}\sqrt{[V_g(R) + \hbar\omega - V_u(R)]^2 + (\hbar\omega_R)^2}\,. \tag{2.16}$$

Figure 2.3(b) shows the adiabatic curves calculated from Eq. (2.16) for different intensities. The data for unperturbed curves can be found in [58] and dipole transition moments needed

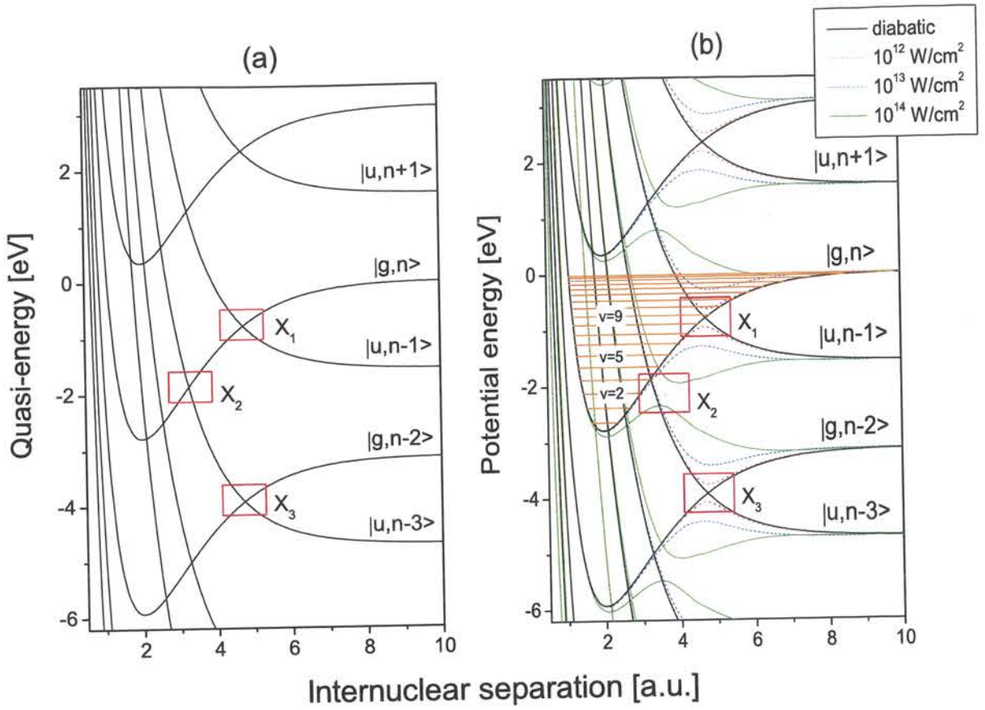


Figure 2.2: (a) Potential curves of the electronic states $1s\sigma_g$ and $2p\sigma_u$ "dressed" with photons (diabatic potential curves). The rectangles labelled X_1, X_2 and X_3 outline the curve-crossing regions. (b) Field-dressed diabatic and adiabatic potential curves for three different intensities [57]. The horizontal lines indicate the free-field energies of the vibrational levels.

for Rabi frequencies from [50]. For the field-free case, the non-diagonal matrix elements in Eq. (2.15) are zero and the eigenvalues are diabatic curves $V_g(R)$ and $V_u(R) - \hbar\omega$. The curves therefore cross at the resonant internuclear separation $R = X_1$, where the energy difference is equal to the photon energy. For non-zero intensities, the curve crossing is avoided, resulting in a "gap" between the adiabatic curves $E_-(R)$ and $E_+(R)$. The width of the gap at $R = X_1$ is proportional to the Rabi frequency, i.e., to the square root of the laser intensity. The light field induces a potential barrier below the avoided crossing and a potential well above it.

The adiabatic curves describe the molecule-light system as a whole. For $R < X_1$, the system has predominantly the attractive ground-state character, whereas the excited state character dominates for $R > X_1$. At the resonant point $R = X_1$, the molecular wave function is composed of same portions of the "dressed" ground-state and the excited wave

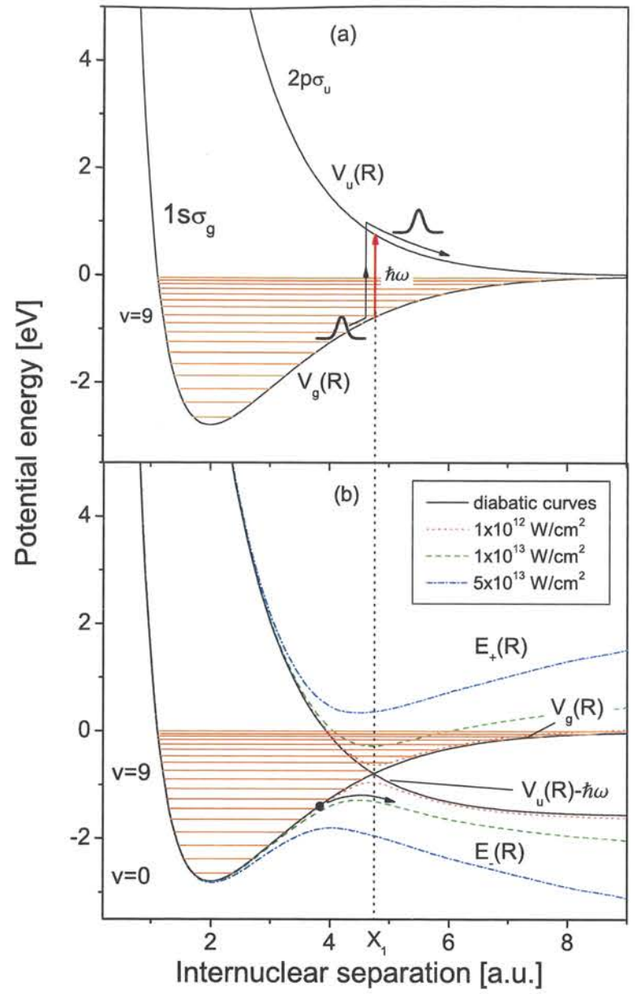


Figure 2.3: (a) Field-free potential curves for the $1s\sigma_g$ and $2p\sigma_u$ states. (b) Field-dressed diabatic and adiabatic potential curves for different intensities obtained by diagonalizing one Floquet block [Eq. (2.16)]. Diabatic curves can be obtained from the field-free potential curves by shifting the curve $V_u(R)$ by the energy of one photon. The avoided crossing X_1 opens at the resonant internuclear separation. The molecule-light system experiences an attractive potential at the left of the crossing and a repulsive potential at the right side of the crossing.

functions, i.e., [59]

$$\Psi(\boldsymbol{r}, R) = \frac{1}{\sqrt{2}} \left[\Phi_{g,n}(\boldsymbol{r}, R) + \Phi_{u,n-1}(\boldsymbol{r}, R)\right].$$

Here almost the entire electronic charge oscillates between the protons. This is known as charge-resonance [60] and will be discussed in Section 2.2.3.

The interpretation of the adiabatic curves can be illustrated using the example of a nuclear wave packet moving on the curve $V_g(R)$ and approaching the point X_1 from the left, as discussed earlier in Fig. 2.1. In the representation for weak fields [Fig. 2.3(a)], the molecule absorbs one photon and ends up on the repulsive curve $V_u(R)$. In the adiabatic picture [Fig. 2.3(b)], this process is described as follows. If the protons move slowly apart, the electron-field system (illustrated now by a black dot) follows the lower adiabatic curve $E_-(R)$. As the internuclear separation reaches the point X_1, the attractive potential changes to a repulsive one. Consequently, the molecule photodissociates, while the field loses one photon being absorbed by the molecule.

The adiabatic curves in Fig. 2.3(b) include only the one-photon process as they result from diagonalization of one Floquet block. Furthermore, the curves $E_+(R)$ and $E_-(R)$ in the dissociation limit do not converge to energies zero and $-\hbar\omega$, respectively. The correct treatment requires inclusion of couplings between many diabatic curves, as illustrated in Fig. 2.2(a). The adiabatic potential curves resulting from diagonalization of matrix (2.13) with 20 Floquet blocks are shown in Fig. 2.2(b). In addition to the gap at the one-photon crossing (X_1), at higher intensities a gap also opens at the three-photon crossing (X_3). Its actual position is somewhat lower with respect to the three-photon diabatic crossing and it almost coincides with the energy of the level $v = 2$. The one-photon gap at these intensities is so large that it is no longer recognized.

2.1.3 Bond softening, trapping and above-threshold dissociation

The light-induced potential curves [Fig. 2.2(b)] account for several new phenomena in intense laser fields. The fate of a particular molecule depends on its vibrational state energy with respect to the avoided crossings:

- The vibrational levels at or above the energy of the one-photon crossing are little influenced by the field and will easily dissociate already at relatively low intensities. This is particularly the case for the level $v = 9$, for which the Franck-Condon factor is maximal.

- The levels above the one-photon crossing can be "trapped" in the upper light-induced potential well. This effect should occur whenever there is a coincidence of diabatic (zero-field) and adiabatic (field-induced) vibrational levels [61]. This phenomenon is called vibrational trapping, molecular stabilization or bond hardening [62, 63, 54, 64, 27].

- The vibrational levels below the one-photon crossing can dissociate either by passing over the top of the barrier or by tunnelling through it, what is known as bond softening [24, 65, 66, 54]. The photodissociation probability for these levels increases nonlinearly with intensity. The lowest vibrational level for which dissociation via one-photon is energetically allowed is $v = 5$, as can be seen in Fig. 2.2(b).

- The vibrational levels at or below the three-photon crossing X_2 can dissociate by absorption of three photons. A molecule in one of these levels follows the lower branch of the adiabatic curve $|u, n-3\rangle$. It encounters then the avoided crossing X_3, where it emits one photon and ends up adiabatically in the state $|g, n-2\rangle$. The total result of the three-photon absorption followed by one-photon emission is a net two-photon absorption. Since more photons were absorbed than it was necessary, this process is often called above-threshold dissociation (ATD) [25, 65] or two-photon bond softening.

2.1.4 Molecular alignment

The adiabatic potential curves displayed in Fig. 2.2 were calculated for the electric field parallel to the molecular internuclear axis. In most of the experiments, however, the molecular orientation is isotropic. The photodissociation dynamics of molecules at an angle θ with respect to the laser polarization axis can be described with the aid of three-dimensional adiabatic potential surfaces [65, 30]. Figure 2.4 shows a lower adiabatic potential surface in the vicinity of the one-photon avoided crossing at an intensity of 7.5×10^{12} W/cm^2.

At smaller internuclear separations, which corresponds to a shorter timescale, the dynamics of the molecules in the vibrational levels below the avoided crossing will be determined by the light-induced potential barrier. The potential barrier is lowest for molecules parallel to the electric field ($\theta = 0°$), whereas its height increases with larger angles. Correspondingly, the dissociation probability decreases with the increasing angle, leading to angular distributions of the fragments peaked along the laser polarization axis. This alignment process is usually termed as geometric alignment, since it is mainly determined by the angular dependence of the photodissociation probability. However, it can also be considered dynamically in terms of a wave packet skirting around the hardly penetrable potential barrier around $\theta = 90°$ [67, 30]. Classically, the electric field exerts a torque on the laser-induced molecular dipole moment. On a longer timescale, i.e., at larger internuclear separations, the wave packet evolving on the lower potential surface will tend to end up in the potential valley centered at $\theta = 0°$, resulting in dynamic alignment of the dissociating molecule.

2.2 Strong-field ionization and Coulomb explosion

2.2.1 Photoionization mechanisms

When an atom or a molecule absorbs a photon of energy $h\nu$ exceeding the ionization potential I_p, it is ionized and the excess energy is carried away by the electron in the form of translational kinetic energy. In the case that the ionization potential is much greater

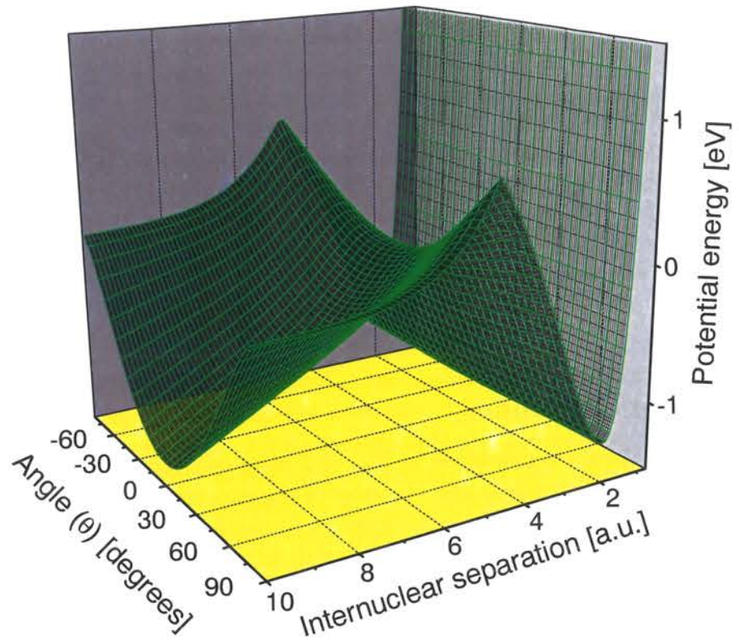


Figure 2.4: Field-dressed lower adiabatic potential surface of H_2^+ in the vicinity of the one-photon avoided crossing (X_1). The peak intensity is 7.5×10^{12} W/cm^2. The graph is adapted from [45].

than the photon energy, different ionization mechanisms can occur. They can be classified according to the Keldysh parameter, which is a measure of the ratio of the energies of a bound electron in the atom and of a free electron in the oscillating electric field of the laser. An alternative description includes the ratio of the timescales characterizing the electric field and the potential, i.e., the optical period T_{laser} and the tunnelling time T_{tunnel}, respectively. The Keldysh parameter [68] is defined as

$$\gamma = \sqrt{\frac{I_p}{2U_p}} \propto \frac{T_{tunnel}}{T_{laser}} . \tag{2.17}$$

U_p is called ponderomotive potential, which is equal to the average energy of the electron's quiver motion in the electric field:

$$U_p = \frac{e^2 E_0^2}{4 m_e \omega^2} \propto I\lambda^2 , \tag{2.18}$$

where E_0 is the amplitude, ω the angular frequency and λ the wavelength of the electric field. The electric field strength is related to the intensity I through Eq. (2.2). Thus

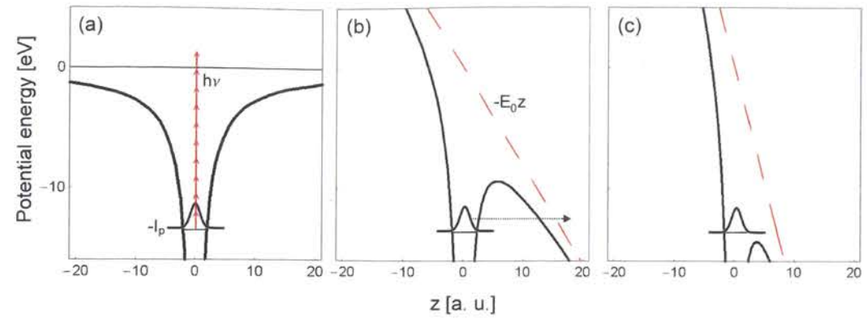


Figure 2.5: Schematic illustration of different mechanisms of atomic ionization: (a) multiphoton ionization, (b) tunnelling ionization and (c) over-the-barrier ionization.

the expression for U_p scales as $I\lambda^2$, which is a parameter commonly found in intense field phenomena.

Figure 2.5 illustrates different ionization mechanisms for the atomic case. They can be classified according to the value of the Keldysh parameter as following:

(a) $\gamma \gg 1$, *multiphoton ionization*
This mechanism is dominant at large ionization potentials, high laser frequencies and intensities in the range of $10^{13} - 10^{14}$ W/cm^2. The molecule absorbs multiple photons within the lifetime of intermediate states (real or virtual), as illustrated in Fig. 2.5(a). Thus, high photon densities are necessary, which have become available only after the development of intense ultrashort lasers. The ionization rate Γ follows a power-law dependence $\Gamma = \alpha I^n$. In this mechanism, the electron oscillating in phase with the electric field gradually builds up kinetic energy with every cycle of the electric field, until it becomes sufficient for leaving the atom. The process is assisted through the electron scattering on the nuclei. If a multiple of the photon energy is equal to the ionization potential, the ionization probability is greatly enhanced. The process in which the atom or molecule absorbs more photons than it is required for ionization is called above-threshold ionization (ATI) [19].

(b) $\gamma \sim 1$, *tunnelling (field) ionization*
This regime is dominant at low frequencies and intensities in the range of $10^{14} - 10^{15}$ W/cm^2. The probabilities for ionization during different cycles of the electric field are independent from each other. The electric field, which can be be considered as quasi-static, distorts the potential barrier, allowing tunnelling of the electron [Fig. 2.5(b)]. The ionization rate is determined by the width of the barrier and increases with intensity. Here the electron does not scatter on the molecule, but it is drawn towards the edge of the molecular orbital, from which it can escape by tunnelling.

(c) $\gamma \ll 1$, *over-the-barrier ionization*
This is the limiting case of field ionization where the barrier is lowered by the strong laser field (intensity $>10^{15}$ W/cm^2) to such an extent that the electron can pass over the top of the barrier without tunnelling [Fig. 2.5(c)]. In this regime the ionization probability approaches unity within one laser cycle [69].

The classification of the ionization mechanisms described above is not strict and the ionization processes often fall in an intermediate regime where the process is described by a combination of the ionization mechanisms.

In the case of the hydrogen molecular ion, the ionization potential depends on the internuclear separation R [70, 71]

$$I_p \sim I_p\,(\mathrm{H\,atom}) + 1/R\,. \tag{2.19}$$

Here all the quantities are in atomic units. The ionization potential of the hydrogen atom is $I_p\,(\mathrm{H\,atom}) = 0.5$ a.u. For the internuclear separation $R = 10$ a.u., where the ionization rate is enhanced (Section 2.2.3), the ionization potential is $I_p \sim 0.6$ a.u. ($\sim$16 eV). With $\lambda = 790$ nm ($h\nu \sim 1.6$ eV) and $I = 10^{14}$ W/cm^2, the Keldysh parameter [Eq. (2.17)] is $\gamma \sim 1.2$. Thus the molecular ionization is best described by the electron tunnelling.

2.2.2 Semiclassical model of enhanced ionization

In the case of H_2^+, the ionization process results in formation of two protons starting to repel each other by Coulomb force. During this process, which is known as Coulomb explosion, each of the protons gains the half of the Coulomb energy $E_{CE} = 1/(2R)$ (in atomic units), where R is the internuclear separation at the moment of ionization. The measured kinetic energies of the Coulomb explosion protons of 1–4 eV (e.g., [64]) are considerably smaller than the energy of about 7 eV that is expected if ionization would take place at the equilibrium internuclear separation $R_{eq} \sim 2$ a.u. This discrepancy can be explained by a semiclassical model of the electron in the electrostatic potential of two protons and the constant electric field [34, 35]:

$$V(z, R, E_0) = -\frac{1}{\sqrt{(z - R/2)^2}} - \frac{1}{\sqrt{(z + R/2)^2}} - E_0 z\,. \tag{2.20}$$

Figure 2.6 illustrates the potential defined by Eq. (2.20) for four different internuclear separations R. The horizontal lines mark the position of the two lowest electronic states in such a potential. These are Stark shifted and their separation is $E_0 R$ at large R. For small internuclear separations, the electron can oscillate freely between the nuclei [Fig. 2.6(a)]. The probability for ionization is here similar to that of the hydrogen atom due to the broad outer potential barrier. As the internuclear separation increases, the inner barrier starts to rise, impeding the charge transfer between the wells [Fig. 2.6(b)]. The probability for tunnelling through the inner barrier during a half of an optical cycle decreases and the electron becomes localized at one proton. This localization of the electron is a crucial element

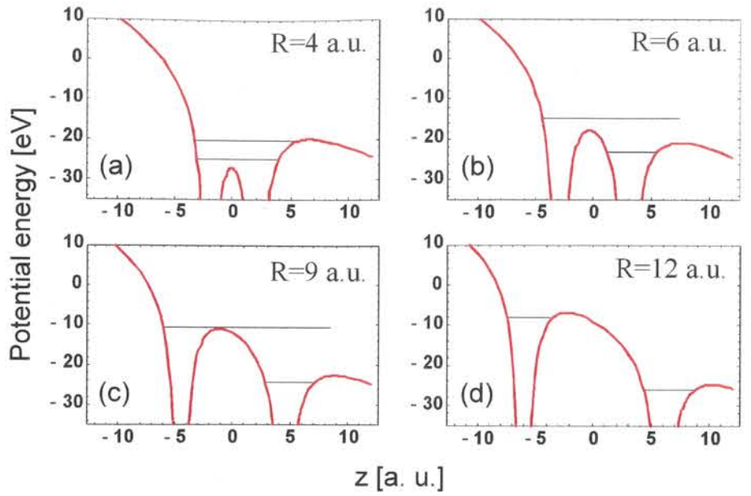


Figure 2.6: Potential energy of the electron in the combined field of two protons (located at $-R/2$ and $R/2$) and a static electric field [Eq. (2.20)]. The amplitude of the electric field is $E_0 = 0.06$ a.u. ($I \sim 1.2 \times 10^{14}$ W/cm^2). The horizontal lines mark the energies of the two lowest electronic states of H_2^+ in the resulting potential.

of the model. Since the electric field changes its direction each half-period, the localized electron will be periodically raised and lowered with the maximum shift of $E_0 R/2$. Thus the upper and lower states will be equally populated. At the times when the electron is in the upper state, it can escape with high probability by tunnelling directly into continuum through the inner barrier [Fig. 2.6(c)]. Ionization will be therefore enhanced in the intermediate range of internuclear separations. For larger R, the inner barrier becomes broad and hardly penetrable, so the ionization probability is again atomiclike.

The exact values of ionization rates as a function of internuclear separation R were calculated in numerous calculations by solving the time-dependent Schrödinger equation in the fixed-nuclei approximation [36, 72–75]. In other approaches, the one-dimensional nuclear motion was taken into account and solutions were obtained by using wave packet propagation methods [76–79]. In the following section, the results of the quantum mechanical calculations by Zuo and Bandrauk are presented [36].

2.2.3 Charge-resonant enhanced ionization (CREI) [36]

Figure 2.7 shows the calculated ionization rates as a function of internuclear separation for a wavelength of 1064 nm and an intensity of 1×10^{14} W/cm^2. The three-dimensional time-dependent Schrödinger equation was solved numerically for different internuclear separations. The linearly polarized laser field was assumed to be parallel with the molecular axis. The field was turned on linearly in five optical cycles and then kept constant.

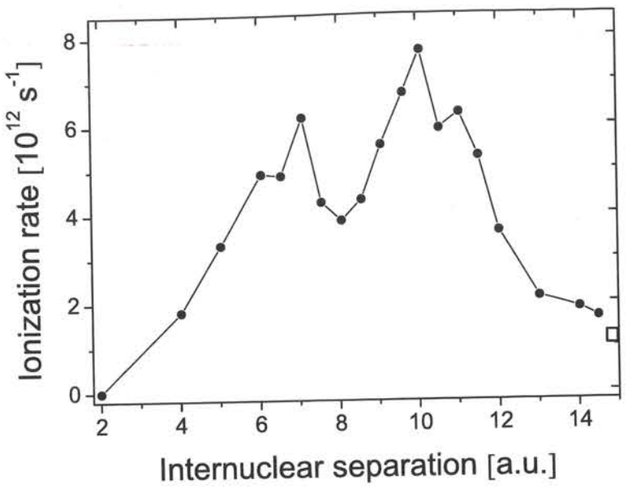


Figure 2.7: Ionization rate of H_2^+ as a function of internuclear separation for a wavelength of 1064 nm and an intensity of 1×10^{14} W/cm^2. The square on the right vertical axis marks the ionization rate of the hydrogen atom. The data were taken from [36].

The results show that the ionization rate is enhanced in the range from 5 to 12 a.u., with two maxima (critical distances) around 7 and 10 a.u. The maximum around 10 a.u. can be explained in the static-field model as ionization from the upper state (see Fig. 2.6). Here, it is important that the dipole matrix element $\langle 2p\sigma_u|ez|1s\sigma_g\rangle$ diverges as $R/2$ for large internuclear separations. The two states are thus strongly coupled for large R and are known as charge-resonant states [60]. At $R \sim 10$ a.u., the states are approximately equally populated, resulting in the maximum in the ionization rate. For smaller R, the population of the upper level is smaller. Hence, the ionization rate is smaller, even though the upper level is already at $R \sim 6$ a.u. above the top of the inner barrier. For large internuclear separations, on the other hand, the broad inner and outer barrier inhibit ionization. The ionization rate approaches the rate of the hydrogen atom (marked with a square in Fig. 2.7).

The maximum around 7 a.u. is attributed to the asymmetric charge distribution in the two wells in the presence of the oscillating electric field. This effect is known as laser-induced electron localization due to the tunnelling suppression. For the wavelength and intensity used in the calculation, the maximum difference in population of the two states is found to be at $R \sim 7$ a.u. The ionization rate is determined by the competition between ionization from the upper electronic state and the tunnelling between the wells. Therefore, the maximum electron localization around 7 a.u. will lead to an enhancement in ionization.

Chapter 3

Experimental

The two intense-field fragmentation mechanisms discussed in the previous chapter — photodissociation

$$H_2^+ + nh\nu \rightarrow H + H^+ \tag{3.1}$$

and ionization followed by Coulomb explosion

$$H_2^+ + n'h\nu \rightarrow H^+ + H^+ + e^- \tag{3.2}$$

were investigated by measuring the velocity distributions of the nuclear fragments. The molecular ions were investigated in fast, mass-selected and well collimated ion beams. The ions were exposed to intense ultrashort pulses produced in an amplified femtosecond laser system. The velocity distribution of the nuclear fragments from both channels were imaged on a position sensitive detector.

The ion beam apparatus and the detection system are described in detail in Section 3.1. In Section 3.2 the method of fragment imaging is explained and procedures of retrieving the original three-dimensional (3D) velocity distribution from the experimental images are described. The femtosecond laser system and the characterization of laser pulses are presented in Section 3.3. The intensity distribution in the interaction region and its implication for measured data is the topic of Section 3.4.

3.1 Ion beam apparatus

The ion beam apparatus used in this work was in previous experiments first applied by Figger *et al* for the investigation of the emission spectra of rare gas hydrides (HeH, ArH, etc.) and triatomic hydrogen molecules (H_3, D_3, H_2D and D_2H) [80–82]. An upgrade of the apparatus for the purposes of fragment imaging was carried out by Wunderlich *et al*, who investigated light-induced potential curves in Ar_2^+ [59, 83–85]. In the study of H_2^+ in intense laser fields, Sändig *et al* improved the ion beam collimation, which enabled them to resolve fragments from single vibrational levels [28, 86].

A schematic of the ion beam apparatus is presented in Fig. 3.1. The apparatus consists of three vacuum chambers, which are each pumped by a turbomolecular pump. The main

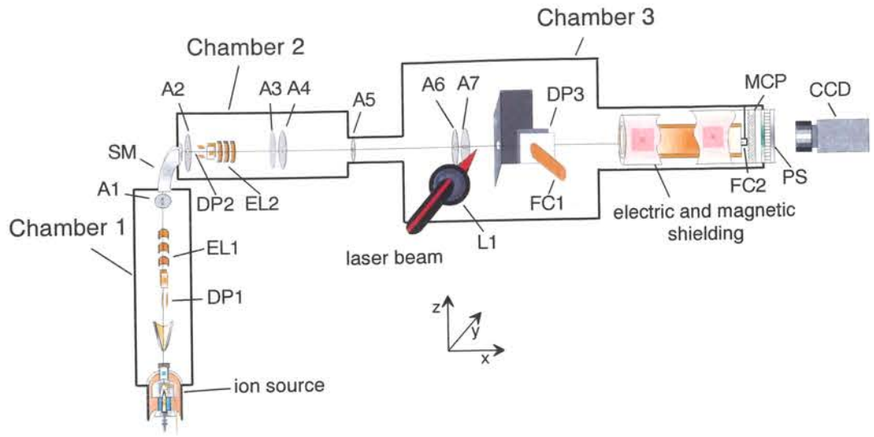


Figure 3.1: Schematic diagram of the ion beam apparatus. DP, deflection plates; EL, Einzel lenses; SM, sector magnet; A, apertures; L1, focusing lens; FC, Faraday cups; MCP, multichannel plate detector; PS, phosphor screen; CCD, CCD (charge-coupled device) camera.

components of the apparatus include ion source, mass-selection magnet, ion optics and apertures for beam steering and collimation, and Faraday cups for measuring the ion current.

3.1.1 Ion source

The molecular ions were generated in a duoplasmatron ion source [87, 80] by a dc electric discharge. A drawing of the ion source is shown in Fig. 3.2. Neutral H_2 gas is introduced in the region between a hollow cathode and an anode through an opening in an intermediate electrode. The cathode and the anode are made of stainless steel, and the intermediate electrode is made of soft iron. The electrons emitted from the hollow cathode are accelerated towards the anode by a potential difference of 300–600 V. The electrons are electrostatically focused by the intermediate electrode, which is held on a potential of about -100 V with respect to the anode. In addition, the plasma is constricted by the magnetic field formed by both the ferromagnetic intermediate electrode and a solenoid magnet surrounding the ion source. The magnet current (typically in the range of 0.5 to 1.5 A) was electronically stabilized. The strength of the magnetic field increases towards the anode, and thus, as the electrons approach the anode, their radial velocity component increases, whereas the axial component decreases. The density of the electrons is hence highest near the anode, intensifying ionization of neutral H_2 molecules.

Molecular ions produced in the plasma are extracted and accelerated by a high potential difference between the anode and a conical shaped extraction electrode. To extract the positive ions, the whole ion source was held on a positive acceleration voltage U_a in the

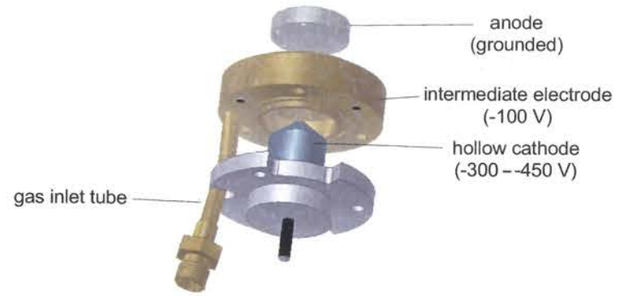


Figure 3.2: Drawing of the duoplasmatron ion source. Neutral gas introduced in the ion source through the inlet tube is ionized by electrons emitted from the hollow cathode. The produced plasma is confined by the electric field of the intermediate electrode and a nonuniform magnetic field of the intermediate electrode and a solenoid magnet. The electrodes are insulated by intermediate ceramic rings (not shown in the figure).

range of 3–12 kV, whereas the rest of the apparatus was grounded. The extracted current of ions is roughly proportional to the area of the anode aperture. Although the extracted current could be greatly enhanced with anodes with apertures of 300 and 400 μm in diameter, only a small portion could be collimated. Sufficient and more stable current was achieved using an anode with an aperture of 200 μm. The extracted current was typically around 100 μA and could be varied by adjusting the current of the solenoid magnet. The electrodes in the ion source deteriorate with time due to their high temperature and electron sputtering. This usually manifested itself in an increased discharge voltage and an unstable extracted current. In this case the hollow cathode was replaced and the intermediate electrode and anode were thoroughly cleaned.

To ensure a constant flow of H_2 gas into the ion source, a two-stage pressure regulator[1] was installed on a gas container. A fine regulation of the flow was achieved by means of a dosing valve[2]. To ignite the discharge, the pressure in the ion source is increased to about 100 Pa for a few seconds. Then it is gradually decreased to a value slightly above the threshold at which the discharge extinguishes (about 10 Pa). Usually about half an hour after ignition is needed for stable ion source operation. The pressure in the ion source was indirectly monitored by measuring the pressure in Chamber 1.

The main formation process of H_2^+ in the ion source is electron impact ionization of H_2 [88]. For the ion source temperature of about 100° C [80], the thermal energy kT is much smaller than the vibrational separation, and thus only the ground vibrational level $v = 0$ of H_2 is populated. In different types of ion sources it was found that the vibrational population of H_2^+ is well described by the Franck-Condon factors between the vibrational levels of H_2^+ in the $1s\sigma_g$ state and the ground vibrational level of H_2 in the electronic ground

[1] Messer Griesheim, Spectron FE 62
[2] Balzers, EVN 116

state [89–91]. The vibrational population of H_2^+ and D_2^+ obtained by von Busch *et al* for an electron bombardment-type ion source is listed in Appendix B. A similar vibrational distribution was also reported for a monoplasmatron ion source, which is similar to the ion source used in our experiment [92].

The rotational temperature of the vibrational ground state of H_2 is approximately 200 K [86], yielding a Maxwell-Boltzmann distribution of the rotational population with maximum for the rotational quantum number $J = 0$ [93]. In the ionization process, the rotational quantum number does not undergo large changes, and thus H_2^+ is formed in the rotational ground state. The smallest allowed change $\Delta J = \pm 2$ occurs with a much lower probability [90].

3.1.2 Mass selection

After extraction from the ion source, molecular ions are directed into a sector magnet[3] (SM) through entrance slit A1 (width of 5 mm) by means of a set of horizontal and vertical electrostatic deflection plates (DP1) and an Einzel lens (EL1). By adjusting the magnetic field B of the magnet, the molecular ions of mass m_m and charge q are deflected by 90° to pass through exit slit A2 (width of 5 mm). The ions selected in this way satisfy the relation

$$\frac{m_m v_0^2}{r} = B v_0 q\,, \tag{3.3}$$

where $r = 150$ mm is the curvature radius of the magnet and v_0 is the velocity of the molecular ions given by

$$v_0 = \sqrt{\frac{2qU_a}{m_m}}\,. \tag{3.4}$$

For an acceleration voltage of $U_a = 11$ kV, which was measured at the ion source by a high voltage probe[4], the velocity of H_2^+ ions is $v_0 = 1 \times 10^6$ m/s. From Eqs. (3.3) and (3.4), the magnetic field reads

$$B = \frac{\sqrt{2U_a m_m/q}}{r}\,. \tag{3.5}$$

In order to select the desired molecular ion, the current after the mass selection was recorded as a function of the voltage on the magnet, which is proportional to the magnetic field B. Such a mass spectrum is shown in Fig. 3.3. The peaks were ascribed to the molecular ions by comparing their masses with measured voltages (i.e., magnetic fields) according to Eq. (3.5).

3.1.3 Ion optics

After exiting the sector magnet, the mass selected ion beam is further steered by a second set of electrostatic deflection plates (DP2). It enters Einzel lens EL2, which in combination

[3] Drusch et Cie, EA 1590 A
[4] Tektronix, P 6015

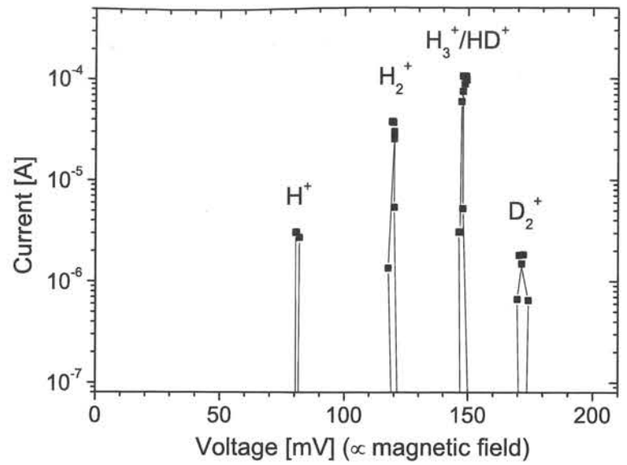


Figure 3.3: Ion current measured at apertures A3 and A4 as a function of the voltage (i.e., magnetic field) on the sector magnet. The ions result from ionization and recombination processes in a H_2 plasma. The acceleration voltage was $U_a = 12$ kV.

with Einzel lens EL1 serves as an electrostatic telescope that collimates and maximizes the flux of the ion beam. The voltages applied to the Einzel lenses were $U_1 \sim 8$ kV and $U_2 \sim -12$ kV. The beam divergence is restricted by apertures A4 and A7 separated by a distance a of 53 cm.

The apertures were composed of two mutually perpendicular slits[5] of different widths. Since a better velocity resolution was needed along the laser polarization axis (z axis), narrower slits were used for collimation along this axis (see Fig. 3.1). In different experiments, the widths of the slits along the z axis were $h_4 = 75 - 200$ μm and $h_7 = 25 - 50$ μm for apertures A4 and A7, respectively (as shown in Fig. 3.6). Such small values of h_7 were also important to reduce intensity variations in the interaction region, as it will be discussed in Section 3.4. Sufficient intensity of the ion current was provided by using slits of widths of 200–300 μm along the laser propagation axis (y axis).

For strongest ion currents and optimal beam collimation, the alignment of the apertures is crucial. For this purpose a helium-neon (HeNe) laser was used, whose propagation axis is first fixed with slit A2 at one end and the center of the multichannel plate (MCP) detector at the other end. After that, a movable Faraday cup in front of the MCP detector (FC2) is adjusted to cover the HeNe beam. After the axis of the HeNe beam is fixed, the attenuated femtosecond laser beam is focused at right angle on it. At this point, the focal position is adjusted only roughly by observing the position of the laser-induced breakdown in air. Overlap of the two beams is provided by a 50 μm pinhole placed under 45° with respect to the both beams. First, the transmission of the HeNe beam through

[5] Melles Griot

the pinhole is maximized by positioning the pinhole along the y and z axes by means of a translational stage and a mechanical feedthrough, respectively. After that, the femtosecond beam is passed through the pinhole by adjusting the x and y position of the focusing lens. After positioning the crossing aperture, aperture A7 and then aperture A4 is aligned by maximizing the signal on a photodiode placed behind the apertures. The procedure described assured that the laser beam will cross the ion beam passing through apertures A4 and A7. The precise adjustment of the overlap of the ion and laser beams along all three axes is done by maximizing the detected fragment signal before each measurement.

3.1.4 Ion current

The alignment of the ion beam is achieved by measuring the ion current at different points along the beam. In front of each of collimating apertures A4 and A7, auxiliary pre-apertures A3 and A6 with diameters of 3 mm and 0.6 mm, respectively, were placed to make the alignment easier (Fig. 3.1). Additionally, aperture A5 with a diameter of 3 mm positioned between Chamber 2 and Chamber 3 could be used for alignment. All apertures as well as Faraday cups FC1 and FC2 were insulated and connected to an electrometer[6]. The current is first optimized on aperture A4 and its pre-aperture by finding a right combination of voltages on the deflection plates, ion lenses and sector magnet. After that, the same procedure is done for aperture A7 and its pre-aperture. Finally, the current is maximized on Faraday cup FC2. Often, it is necessary to repeat the whole procedure several times with similar or different initial voltages, until no further increase in the current could be achieved.

With a 200 μm circular aperture A4 and a 300×25 μm aperture A7, the current of a 11 keV H_2^+ beam measured on Faraday cup FC2 could be optimized up to 3–4 nA, which is by factor 2–3 higher than in the previous experiment [86]. This was achieved by enabling extraction of higher currents from the ion source as well as the better optimization of the currents measured on the apertures. Thereby, the width of the beam was reduced to 25 μm (instead of 50 μm), which increased the collimation and reduced intensity variations in the interaction region (Section 3.4).

During measurements the current was read out from the electrometer by a personal computer via an IEEE interface. The average current measured on Faraday cup FC2 integrated over time is proportional to the number of molecular ions in the interaction region. For a typical current in the interaction region of about 100 nA, a laser beam diameter of 60 μm and a velocity of molecular ions of 10^6 m/s, the momentary number of molecules in the interaction region can be roughly estimated to ∼40.

The stability of the ion current is influenced by several factors. The most important of them were found to be a good ion beam alignment, stable operation of the ion source and elimination of discharges. Discharges observed between the anode and the tip of the extraction electrode could be eliminated by smoothing and cleaning the surfaces. Frequent discharges occurring on lens EL2 probably resulted from charge accumulation and sputtering on the ceramic holder rings caused by the ion beam. The problem was solved by constructing a new lens with an additional aperture added at its entrance. Also clean surfaces and better evacuation through additional openings were beneficial. In addition, a new design provided easier alignment of the lens axes [46].

[6]Keithley Instruments, model 617

The horizontal deflection plates DP3, placed after the molecule-laser interaction region, could be used to deflect the ion beam and positive fragments into Faraday cup FC1 (see also Fig. 3.5). In this way the remaining neutral fragments could be separately detected on the MCP detector. For detection of both charged and neutral fragments, no voltage was applied to deflection plates DP3. In order to protect the detector and to measure the current, Faraday cup FC2 was placed into the beam in front of the detector. This, however, prevented the detection of fragments with small deflections off the ion beam axis. To minimize this effect, a Faraday cup with a diameter of 4 mm was constructed, which provided a secure capture of fast molecular ions.

The deflection plates DP3 were enclosed in a metal housing to restrict the electric fields to the region inside the housing. The path of the fragments between deflection plates DP3 and the detector was shielded against electric and magnetic stray fields using a copper cylinder and two concentric cylindrical sheets of a high-permeability metal [59].

3.1.5 Detection system

A two-dimensional (2D) position sensitive detector was mounted on a CF-100 flange of a nipple used as path for fragments (Figs. 3.1 and 3.5). The detector was centered on the ion beam axis with the surface perpendicular to it. The distance between the interaction region and the detector was varied between 55 and 95 cm by using nipples of different lengths. The detector assembly[7] consisted of a photocathode, two multichannel plates and a phosphor screen (Fig. 3.4). The active surface of the detector had a radius of 40 mm and comprised millions of microchannels with diameters of 10 μm. A photon or a high energy fragment impinging onto the detector causes secondary electron emission from the photocathode. The electrons, accelerated by a strong electric field, enter a microchannel, where they are multiplied. Upon leaving the multichannel plates, the electron bunches are accelerated towards the phosphor screen. There they produce light flashes, whose 2D position corresponds to the position of the impinging particle on the photocathode. The phosphor screen employed here (P43) is characterized by high efficiency and a slow decay time of approximately 1 ms.

The phosphor screen was held at a constant voltage of 6.0 kV (Fig. 3.4). The MCP detector was operated in a gated mode in which a voltage of -1.4 kV was applied between the front and the rear side of the MCP detector. In order to keep the voltage between the MCP and the phosphor screen constant during the detection period, the rear side of the MCP, which faces the phosphor screen, was grounded and the voltage was applied to the front side of the MCP. The electric field of the MCP was shielded by mounting a grounded stainless steel grid on the vacuum side of the detector. The diameter of the mesh wires

[7]Proxitronic, OD 4062 Z-V

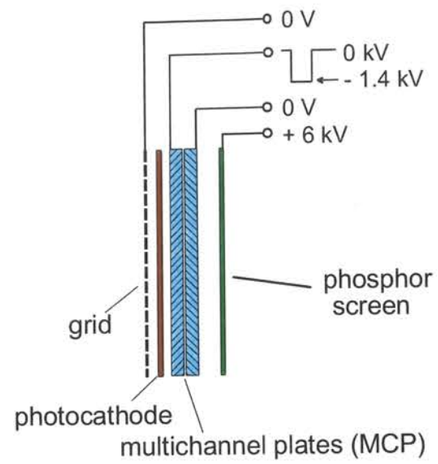


Figure 3.4: Schematic of the two-stage multichannel plate detector with the typical operating voltages.

was 28 μm and their separation was 224 μm [59].

The pattern on the phosphor screen was recorded by a Peltier cooled CCD (charge-coupled device) camera[8]. The optical coupling of the 40-mm diameter phosphor screen and a 8.8×6.6 mm CCD chip with 384×286 pixels was achieved by a $f = 25$ mm objective lens[9]. The imaging system was calibrated by taking an image of a ruler placed across the phosphor screen. If the whole area of the phosphor screen is imaged, the separation between two adjacent pixels corresponded to a distance of 107 μm on the phosphor screen. The resolution of the MCP detector is mainly determined by the diameter and the spacing of the microchannels. An additional factor is radial spread of electrons in the acceleration gaps between the photocathode and MCP, and the MCP and phosphor screen, which limits resolution to 25 line pairs of 5% contrast per mm. This corresponds to 40 μm on the phosphor screen, which is smaller than the size that can be resolved by the CCD camera. In order to increase the resolution, in the Coulomb explosion experiments (Chapter 6) only about a half of the detector was imaged with the CCD camera. The magnification factor was increased by adding additional extension tubes between the lens and the CCD chip, which decreased the "pixel size" to about 55 μm.

3.1.6 Data acquisition

The detection occurred during a 120 ns long time window centered around the arrival time of the fragments. A CCD camera recorded the pattern on the phosphor screen after the signal from usually 2500 laser shots had been accumulated. In the same way a background

[8]LaVision, FlameStar
[9]Schneider Optics, Xenon 0.95/25mm

image was taken while no fragments were arriving on the detector (2 μs after the first time window). For an efficient data acquisition, three foreground images were followed by one such background image.

The detection process is illustrated in Fig. 3.5. The sequence is initiated by a laser pulse triggering a fast photodiode (PD) with the laser repetition frequency of 1 kHz. A pulsed signal from the photodiode is amplified[10] and sent as a trigger to two delay generators[11] (DG). The first pulse generator produces two 120 ns long rectangular signals with different delay times with respect to the triggering signal – pulse A for the foreground signal and pulse B for the background signal. Depending on the state of relay R, either signal A or signal B is sent to a high-voltage switch[12] (HVS). Following that, a high voltage pulse of -1.4 kV is applied to the MCP with the laser repetition frequency. The second pulse generator sends a signal to a 1/10 frequency divider (FD). The divider transmits the pulses with a repetition rate of 100 Hz to a personal computer (PC1), where pulses are counted. In the case the preset number of pulses is achieved (250 in this case), PC1 sends a signal to the CCD camera controlling unit. An image of the phosphor screen is captured by a CCD camera. The image is then transferred to PC1 and added digitally to the previously captured images. After an image was recorded, PC1 sends a signal to a two-bit counter (C). On every fourth signal, when a background image should be taken, the state of the counter and thus the state of relay R changes. The high-voltage switch receives delayed signal B and the MCP is activated for the background signal. The image captured after the same number of laser shots (i.e., 2500) is added to previously recorded background images. After typically about 100 such cycles, which correspond to $100\times3\times2500 = 7.5\times10^5$ laser shots, the summed background image is multiplied by 3 and then subtracted from the summed foreground image.

In order to roughly estimate the number of counts corresponding to a single proton fragment, images with separable single-fragment events were recorded. The measurements showed large fluctuations in the number of counts corresponding to single protons. The average number of counts per proton summed over the exposed pixels could be approximated by a value of 1000 with an uncertainty of 50%. Thereby the acceleration voltage was 11.1 kV and the voltages applied to the MCP and phosphor screen were -1.4 kV and 6.0 kV, respectively.

The sensitivity of the detector area was checked by exposing it to UV radiation of a mercury-argon spectral calibration lamp[13]. For this purpose the detector was mounted on one side of a vacuum chamber, while the light from the lamp was entering through a quartz window mounted on the other side of the chamber. The image obtained showed a uniform intensity distribution over the detector with a few "bad" spots outside the area used in the experiments. The maximum difference in the intensity of single pixels was 8%. When the signal was integrated over about 20 pixels, as for the images in the Coulomb explosion channel (e.g., Fig. 6.7), the maximum difference was about 2%.

[10]Stanford research, SR440
[11]Stanford research, DG535
[12]Behlke electronics, GHTS 60
[13]Lot-Oriel, model 6035 Hg(Ar)

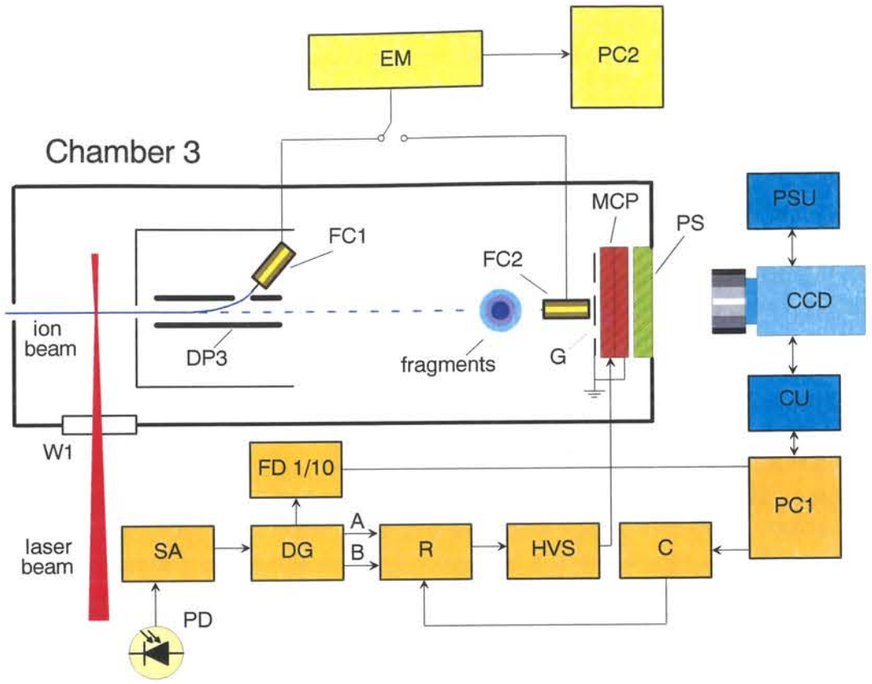


Figure 3.5: Schematic of Chamber 3 and the components used in the detection. W1, window; PD, photodiode; SA, signal amplifier; DG, delay generator; FD, frequency divider; R, relay; HVS, high-voltage switch; C, 2-bit counter; PC, personal computer; CU, CCD control unit; PSU, Peltier stabilization unit; EM, electrometer; DP, deflection plates; FC, Faraday cup; G, grid; MCP, multichannel plate detector; PS, phosphor screen.

3.1.7 Collimation of the ion beam

In addition to the characteristics of the detection system discussed in Section 3.1.5, the experimental resolution is influenced by the width and divergence of the ion beam. These quantities could be estimated by considering the sizes of the apertures along the laser polarization axis (z axis) and the position of the apertures and detector along the ion beam axis (x axis). The schematic diagram of the collimation geometry in the x-z plane is shown in Fig. 3.6. The inner pair of rays illustrates an optimally collimated ion beam, whereas a beam with a maximum allowed divergence is indicated by the outer pair. The widths of the corresponding "shadows" on the detector are designated by letters s and S. The angle α is found from similarity of triangles

$$\tan\alpha = \frac{h_4/2}{a+q} = \frac{h_7/2}{q}\,, \tag{3.6}$$

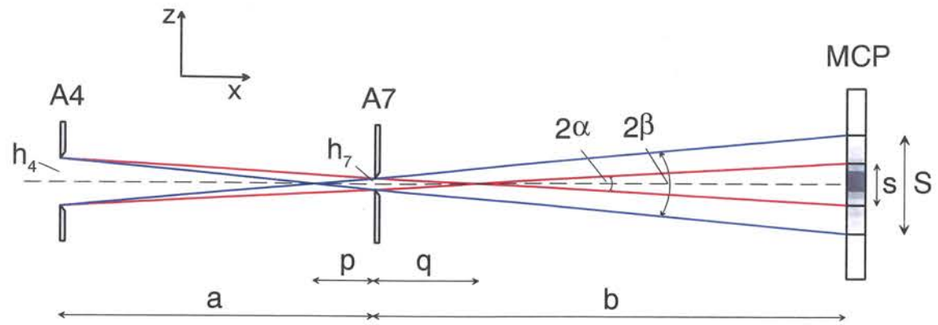


Figure 3.6: Schematic diagram of the geometry employed for collimation along the z axis. Apertures A4 and A7 are not drawn to scale.

which after eliminating q reads

$$\tan\alpha = \frac{h_4 - h_7}{2a}\,. \tag{3.7}$$

The width s is given by

$$s = 2(b-q)\tan\alpha = h_4\,\frac{b}{a} - h_7\left(1+\frac{b}{a}\right)\,. \tag{3.8}$$

In a similar way one obtains

$$\tan\beta = \frac{h_4 + h_7}{2a}\,, \tag{3.9}$$

and

$$S = 2(b+p)\tan\beta = h_4\,\frac{b}{a} + h_7\left(1+\frac{b}{a}\right)\,. \tag{3.10}$$

For illustration, the divergence angles α and β as well as the corresponding widths s and S were calculated for the parameters from the experiments on D_2^+ (Chapter 4). The values are listed in Table 3.1. The data show that the ion beam can spread to a width of about 450 μm at the detector, although its width in the interaction region was only 50 μm. A significantly better collimation of the beam can be realized with a smaller aperture A4, providing that the number of fragments is sufficient. The stronger signal in measurements on H_2^+ (Chapter 5), which was due to higher laser intensities and a higher acceleration voltage used, allowed a smaller aperture A4 with a width of $h_4 = 75$ μm.

In order to verify the above estimation, the ion beam was imaged onto the MCP detector for a short period of about 2 μs with a relatively low voltage of 1.0 kV applied to the multichannel plates. As expected, the image shown in Fig. 3.7 is narrower along the better collimated z axis. A Gaussian fit to the profile along this axis yields a full width at half maximum (FWHM) of 430 μm. The measured width becomes closer to the estimated value when additional broadening occurring in the MCP is taken into account.

Table 3.1: The divergence angles and widths of the ion beam at the detector calculated for the parameters from the D_2^+ measurements (Chapter 4).

a [cm]	b [cm]	h_4 [μm]	h_7 [μm]	α [mrad]	β [mrad]	s [μm]	S [μm]
53	85	200	50	0.14	0.24	190	450

3.1.8 Vacuum system

The three vacuum chambers were pumped by separate turbomolecular pumps backed by rotary pumps. The differential pumping and small apertures between the chambers assure that a relatively high pressure in the ion source region is reduced stepwise towards the detection region. The pumping speeds of the turbomolecular pumps and the typical pressures in the chambers are given in Table 3.2. A vacuum of $\sim 2\times10^{-8}$ mbar in the interaction and detection region was achieved by installing a 700 l/s turbomolecular pump. Bayard-Alpert ionization gauges[14] were used to measure the pressures in the vacuum chambers and Pirani thermal conductivity gauges[15] for the pressures between each rotary and turbomolecular pump. Gate valves between the chambers enabled their separate venting with nitrogen. In order to suppress vibrations, the rotary pumps were placed on damping rubber blocks and bellows were attached to massive metal blocks.

Table 3.2: Pumping speeds of turbomolecular pumps and typical pressures in the vacuum chambers.

vacuum chamber	Chamber 1	Chamber 2	Chamber 3
pumping speed for N_2 [l/s]	345[a]	500[b]	680[c]
pressure [mbar]	2×10^{-5}	2×10^{-6}	2×10^{-8}

[a] Leybold, Turbovac 360
[b] Pfeiffer, TPU 510
[c] Leybold, Turbovac TW 700

3.2 Imaging of fragments

Imaging the fragment velocity distribution can provide information on both the kinetic energy and the angular distributions of fragments. The principle of this technique is explained in the first subsection. Next, methods of retrieving the original 3D velocity

[14] Leybold, Ionivac IE 414
[15] Leybold, Thermovac TM 21

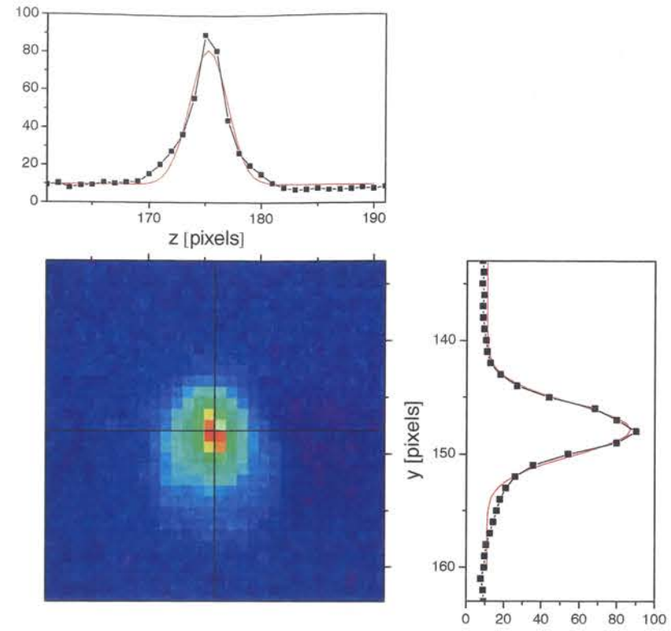


Figure 3.7: The ion beam profile obtained by imaging the beam on the MCP detector. A voltage of 1.0 kV was applied to the MCP detector for a total period of about 2 μs. The data in the horizontal and vertical profiles were interpolated and then fitted by a Gaussian distribution. The FWHMs of the z- and y-profiles are 430 and 570 μm, respectively ("pixel size" is 107 μm). The widths of the apertures were $h_4 = 200$ μm and $h_7 = 25$ μm.

distribution are described and their results are compared on an example of an experimental image. Finally, the upper limit on the velocity and kinetic energy resolution is estimated.

3.2.1 Principle of fragment imaging

The principle of imaging is illustrated in Fig. 3.8(a). At time $t = 0$, molecular ions in the beam interact with a vertically polarized laser pulse, resulting in fragmentation via photodissociation or Coulomb explosion. For the case of homonuclear molecules H_2^+ and D_2^+, the energy E gained during the process is equally shared between the fragments. From the conservation of momenta, it follows that the fragments recoil in opposite directions along the molecular axis with velocities $v = \sqrt{E/m}$, where m is the mass of the fragment. The monoenergetic fragments are thus found on the surface of a sphere that expands while travelling towards the detector. In the case of fragments with different kinetic energies, their spatial distribution will comprise nested spheres of different radii, thus reflecting the 3D velocity distribution of the fragments. The density of the fragments on a sphere is generally not isotropic because of the angular dependence of the fragmentation probability.

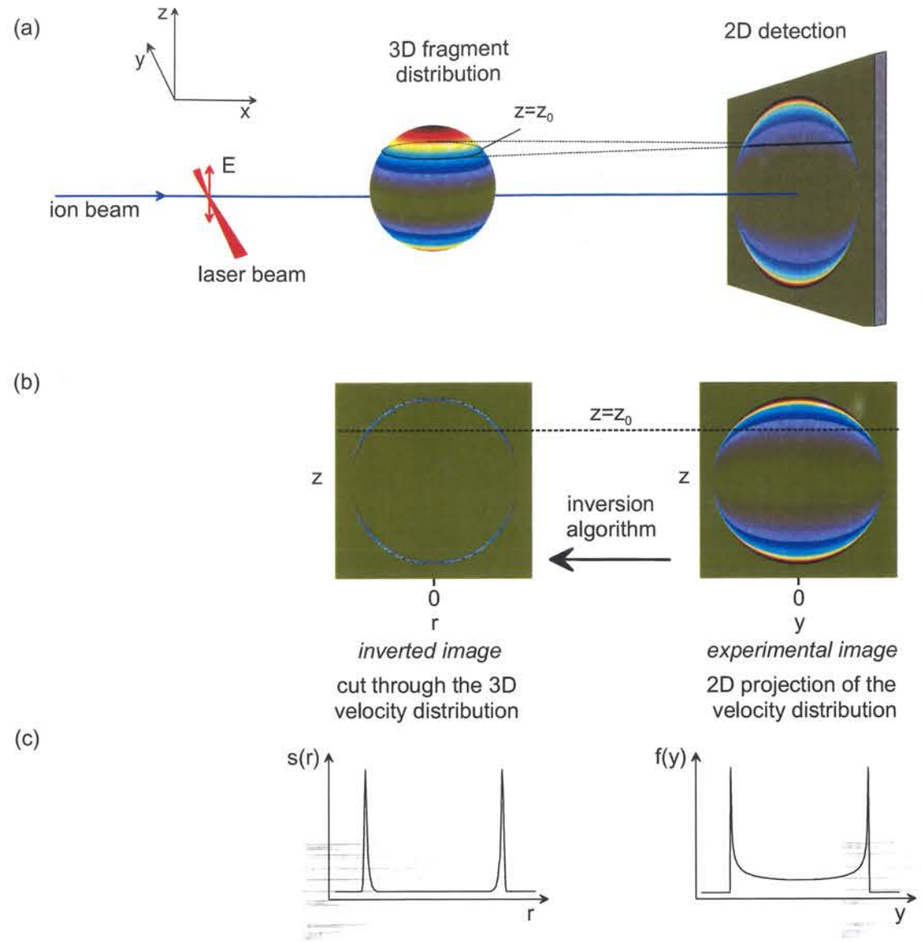


Figure 3.8: Schematic overview of the fragment imaging. (a) Monoenergetic fragments created after molecule-laser interaction are distributed on the surface of an expanding sphere. The density of the fragments on the sphere (indicated by different colours) reflects the fragment 3D velocity distribution. The sphere is projected onto the plane of the MCP detector, yielding a 2D projection of the 3D velocity distribution of the fragments. (b) A cut through the 3D velocity distribution containing the symmetry axis is obtained from the experimental image by means of an inversion algorithm. Here the experimental image was simulated by the projection of a $\cos^2\theta$ distribution (θ is the polar angle). (c) Cuts through the experimental and inverted images at $z = z_0$. The distribution $f(y)$ is the projection of a slice distribution $s(r)$ onto the y axis (see Fig. 3.9). Here $s(r)$ was reconstructed from the simulated 2D projection.

Since this probability depends only on the relative angle between the molecular and laser polarization axis, the distribution of the fragments will be cylindrically symmetric with respect to the laser polarization axis. After the time $t \sim L/v_0$, where L is the distance between the interaction region and the detector, the sphere is projected onto the plane of the detector. The resulting experimental image (usually called "raw" image) presents a 2D projection of the 3D velocity distribution of the fragments.

3.2.2 Inverse Abel transform

The original 3D velocity distribution of fragments can be recovered from its projection, provided the detector plane contains an axis of symmetry. From Fig. 3.8(a) it can be seen that each slice through the 3D velocity distribution perpendicular to the symmetry axis is projected onto one horizontal line of the experimental image. Thus, the 2D inversion problem can be reduced to a 1D problem by inverting each line separately. Figure 3.9 shows the projection of a slice at $z = z_0$ onto the y axis of the detection plane. The distribution of the slice is described by a function $s(x, y)$, which is for the case of monoenergetic fragments non-zero on the circle only. The distribution $f(y)$ is obtained from

$$f(y) = \int_{-\infty}^{\infty} s(x, y)\,\mathrm{d}x = 2\int_{0}^{\infty} s(x, y)\,\mathrm{d}x\,. \tag{3.11}$$

Using the substitution $r^2 = x^2 + y^2$, Eq. (3.11) becomes

$$f(y) = 2\int_{y}^{\infty} \frac{s(r)r\,\mathrm{d}r}{\sqrt{r^2 - y^2}}\,. \tag{3.12}$$

The right side of Eq. (3.12) is known as the Abel transform of the function $s(r)$, and hence $s(r)$ can be retrieved using its inverse Abel transform [94]

$$s(r) = -\frac{1}{\pi}\int_{r}^{\infty} \frac{\mathrm{d}f(y)/\mathrm{d}y}{\sqrt{y^2 - r^2}}\,\mathrm{d}y\,. \tag{3.13}$$

By evaluating Eq. (3.13) line by line, the functions $s(r)$ are calculated for all slices. The inverted image is then built up of horizontal lines displaying $s(r)$ for different values of z. In Fig. 3.8(b), the experimental image was simulated by the projection of a $\cos^2\theta$ distribution (θ is the polar angle). The image was inverted using the algorithm of Vrakking, which is described in the next section. The inverted image is a cut through the 3D velocity distribution containing the symmetry axis. The original 3D distribution illustrated by the sphere in Fig. 3.8 can be obtained by rotating the inverted image along the symmetry axis. The plots in Fig. 3.8(c) show the distributions $s(r)$ and $f(y)$ as cuts through the inverted and experimental images at $z = z_0$.

3.2.3 Comparison of inversion algorithms

The inverse Abel transform described in the previous section is in practice difficult to solve because of the singularity in the integral at the lower limit, and because the derivative tends to magnify noise. In order to obtain reliable inverted images with a low noise,

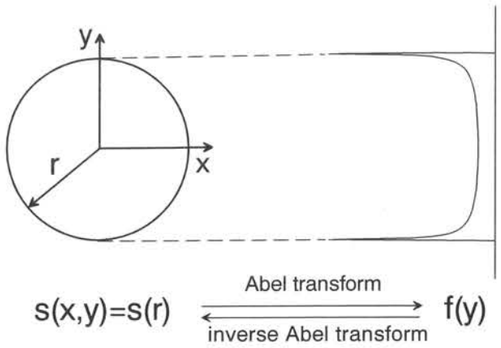


Figure 3.9: The Abel projection of a slice through the 3D velocity distribution at $z = z_0$ onto the y axis. The distribution $s(r)$ on the slice can be retrieved from the projected distribution $f(y)$ using the inverse Abel transform.

three inversion procedures have been tested on an example of an experimental image [Fig. 3.10(a)]. In comparison with the model example in Fig. 3.8, where all fragments have the same kinetic energy, in the experimental image Fig. 3.10(a) the fragments with different kinetic energies were recorded, corresponding to molecules in different vibrational levels. In the inverted images Figs. 3.10(b)-(d), the "rings" associated with the single vibrational levels are more clearly resolved. Moreover, the contribution of the narrowly distributed fragments at lower velocities is more pronounced. In the experimental image, these fragments are overshadowed by the higher-energetic fragments distributed on larger radii on the same slice, and are thus projected at the same position on the detector.

Until recently, the most commonly used procedure for calculating the inverse Abel transform [Eq. (3.13)] was the Fourier-Hankel technique [95]. The method is based on a representation of the inverse Abel transform by the Hankel transform of the Fourier transform of the projection. Although the problems associated with noise are reduced using this representation, reconstructed images are particularly noisy around the symmetry axis. The image shown in Fig. 3.10(b) was reconstructed using the Fourier-Hankel method provided by the AbelWin package [96].

Recently, several methods with better performances have been developed [99], of which the best results are obtained by BASEX (basis-set expansion Abel transform) method [97] and the iterative procedure of Vrakking [98]. The BASEX method is based on expanding the projected image in a basis set of functions that are Abel transforms of known functions. The original 3D velocity distribution can be reconstructed as a linear combination of these functions, with the same expansion coefficients as the projection. The iterative method of Vrakking exploits the similarity between the original 3D angular and velocity distribution, and the projected 2D angular and radial distributions. Based on that, a trial 3D velocity distribution is assumed, from which a 2D projection is calculated. The differences between the calculated projection and the experimental image are used to apply

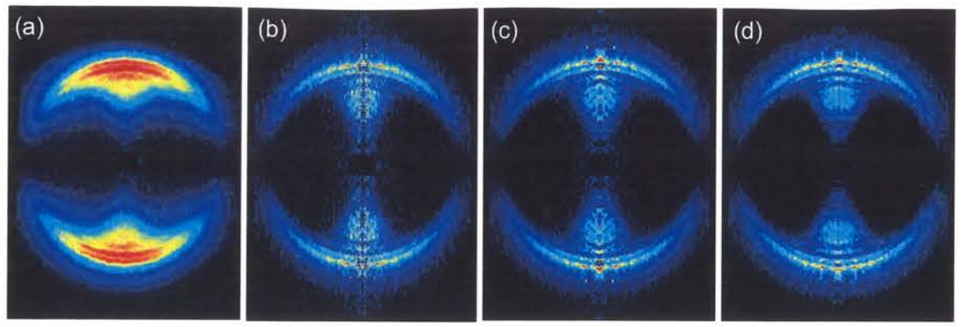


Figure 3.10: (a) Measured 2D projection of the velocity distribution of the fragments from photodissociation of D_2^+ at an intensity of 3.5×10^{13} W/cm^2. Cuts through the 3D velocity distribution reconstructed using: (b) Fourier-Hankel method (AbelWin package [96]); (c) BASEX method [97]; (d) iterative procedure of Vrakking [98].

corrections to the 3D velocity distribution. The procedure is repeated until the differences between the calculated and experimental image are acceptably small. For 15 iterations on a 500×500 matrix, reconstruction takes about one hour on a computer with a Pentium IV processor working at 1.6 GHz. For comparison, the BASEX method requires only 1–2 minutes for the same input data. The images reconstructed using the BASEX method and the iterative procedure are displayed in Figs. 3.10(c) and 3.10(d), respectively. In both images the noise level is much smaller in comparison with the result of the Fourier-Hankel method. Particularly the noise accumulated along the symmetry axis is significantly reduced, specially in the case of the iterative procedure. In addition, the iterative procedure was tested on images with narrow angular distributions [31], which are characteristic for images obtained in this work. For these reasons, the iterative procedure of Vrakking was used to invert images in this thesis.

Although in Figs. 3.10(c) and 3.10(d) the noise at the symmetry axis is significantly reduced, it is not completely eliminated. The reason is that near the symmetry axis, fewer points in the original 3D distribution contribute to the projected signal. Namely, from Fig. 3.8(b) it can be seen that in the 3D distribution, the point at a distance r_0 from the symmetry axis contributes to the points with $y \leq r_0$ in the projected image. Thus, in the projected image, the signal near the symmetry axis results from fewer points. Particulary, at the symmetry axis ($y = 0$), only one point ($r_0 = 0$) contributes to the signal, causing lower signal-to-noise ratio in this part of the projected image.

3.2.4 Velocity and energy resolution

The velocity and energy resolution of the setup can be estimated by considering the maximum divergence of the ion beam, as discussed in Section 3.1.7. For the fragments with velocity $\boldsymbol{v_0}$ at an angle β relative to the ion beam axis, the velocity spread along the z axis

is given by

$$\delta v = 2v_0 \sin\beta\,. \tag{3.14}$$

Here the velocity of the fragments was approximated by the velocity of the ion beam v_0 [Eq. (3.4)]. The fragments ejected with velocities v along the laser polarization axis (z axis) will be displaced by

$$D = vt\,, \tag{3.15}$$

where $t \sim L/v_0$ is the time between the interaction and detection. The maximum velocity that can be observed on a detector of a radius r is equal to

$$v_{max} = \frac{r}{t} = \frac{r}{L}\sqrt{\frac{2qU_a}{m_m}}\,. \tag{3.16}$$

The imaged velocity range can be increased with a faster ion beam or by decreasing the distance L between the interaction region and the MCP detector. In order to achieve a better resolution of the imaging system, the measured velocity range should be imaged on the largest possible area of the MCP detector. For small velocity spreads, one should use lower acceleration voltages [Eq. (3.14)]. Some experimental parameters describing the imaged velocity range and the velocity spread are listed in Table 3.3. In the D_2^+ measurements (Chapter 4), only fragments from the dissociation channel were recorded, and thus the maximum fragment energy that could be detected was set to about 1.0 eV. On the other hand, in the case of measurements on H_2^+ (Chapter 5), fragments with energies above 4 eV from the Coulomb explosion channel were imaged. The energy range was increased by using a higher acceleration voltage. In addition, a larger area of the detector was used by displacing the zero-velocity point from the detector center. The higher fragment signal here also allowed better collimation, which yielded a relative velocity resolution $\delta v/v_{max}$ of 8×10^{-3}.

Table 3.3: Parameters used in the measurements on D_2^+ (Chapter 4) and H_2^+ (Chapter 5) determining the velocity range and the velocity spread of the fragments.

ion	U_a [kV]	v_0 [m/s]	L [cm]	t [μs]	v_{max} [m/s]	E_{max} [eV]	β [mrad]	δv [m/s]
D_2^+	3.1	3.8×10^5	80	2.1	9.7×10^3	0.98	0.24	180
H_2^+	11.1	1.0×10^6	95	0.9	2.9×10^4	4.3	0.12	240

The relative energy resolution of the fragments is given by

$$\frac{\delta E}{E_{max}} = \frac{2v\delta v + (\delta v)^2}{{v_{max}}^2}\,. \tag{3.17}$$

In the case of D_2^+, this quantity varies between 4×10^{-4} at the center and 4×10^{-2} at the edges of the detector, which corresponds to an energy resolution δE of 0.3 meV and 36 meV, respectively. In the case of H_2^+, the energy resolution at the maximum energy of 4.3 eV was 73 meV.

In the preceding discussion, the velocity spread of the molecular ions along the ion beam axis was not taken into account. The energy spread of the ions extracted from a duoplasmatron ion source is less than 10 eV [100]. In the case of D_2^+, this corresponds to a half-width of the velocity distribution of $\Delta v_0 \sim 1.5 \times 10^4$ m/s, i.e., $\Delta v_0/v_0 \sim 0.04$. Due to a spread of the time of flight of $\Delta t \sim 90$ ns, the fragments would have a maximum energy spread (FWHM) of 190 meV. In the experiment, the energy spread in the ion source is somewhat lower and momentum selection by sector magnet SM and the collimating apertures further narrows the velocity spread. The given value thus presents the upper limit on the width of the kinetic energy distribution of fragments. In the photodissociation spectra of D_2^+, peaks separated by 60 meV were clearly resolved.

3.3 Femtosecond laser system

In this section, the femtosecond laser system and methods of characterizing laser pulses are described. The peak laser intensity is defined in terms of the measured pulse energy, pulse duration and beam diameter in the interaction region.

3.3.1 Laser setup

Ultrashort laser pulses were produced and amplified in a commercial chirped pulse amplification (CPA) laser system. Figure 3.11 shows the layout of the system. The system comprises a femtosecond oscillator, a pump laser for the oscillator, a chirped pulse amplifier and a pump laser for the amplifier.

Femtosecond oscillator

A diode-pumped Nd:YVO_4 solid-state laser[16] was used as the pump laser for the oscillator. Continuous wave radiation at a wavelength of 532 nm is produced by intra-cavity frequency doubling of the fundamental frequency in a LBO crystal. The femtosecond pulses are generated in a Ti:Sapphire oscillator[17] utilizing the Kerr lens mode-locking principle [101]. The mode locking could be achieved by enabling an intra-cavity acousto-optical modulator on startup. Two prism pairs serve to compensate for the positive group velocity dispersion introduced by the optical components in the cavity. The central wavelength is tunable in the range from 720 to 850 nm by a movable slit inserted in a part of the beam where the spectral components are spatially separated by means of a prism. The spectral width could be adjusted by varying the slit width. For the best performance of the amplifier, the central wavelength was set to 791 nm with a spectral width of 14.5 nm (FWHM). The spectrum was measured by coupling a part of the beam to a fiber via an Ulbricht sphere

[16] Spectra Physics, Millennia V
[17] Spectra Physics, Tsunami

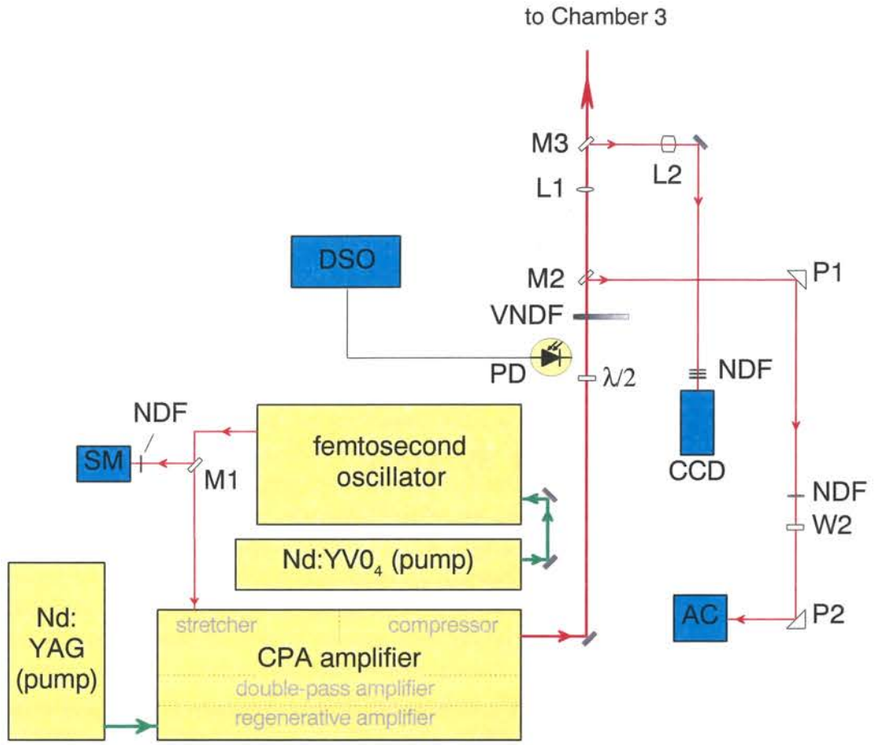


Figure 3.11: Layout of the femtosecond laser system. M, mirrors in flipper mounts; NDF, neutral density filter; SM, spectrometer; $\lambda/2$, half-wave plate; PD, photodiode; DSO, digital storage oscilloscope; VNDF, variable neutral density filter; L, lenses; P, prisms; W, window; AC, autocorrelator; CCD, CCD camera.

and sending it to a spectrometer[18]. The laser generated pulses of 70 fs in duration with a repetition frequency of 82 MHz. When pumped with 4.5 W, the average output power was approximately 600 mW, corresponding to pulse energies of 7 nJ.

As a pump laser for the CPA amplifier, a flashlamp-pumped Nd:YLF (Nd:$LiYF_4$) laser[19] was employed in the first period of this work. The fundamental frequency is frequency doubled in a LBO crystal to produce radiation at 527 nm. The laser operated at a repetition frequency of 1 kHz by Q-switching the cavity with an acousto-optical modulator. The maximum average output power was 25 W, of which about 23 W were used. Because of frequent water leakages from the chiller and fluctuations in power of up to 20%, the laser had to be replaced. A new delivered laser of the same type had insufficient internal cooling for the Q-switch, which was solved by an external cooling from the public water supply. The

[18] APE, PulseScope
[19] Spectra Physics, Merlin

cavity for the flashlamps was extremely noisy and caused large pulse-to-pulse fluctuations. Besides that, the Q-switch was often damaged and had to be replaced several times. The problems were solved after replacing the pump laser by a diode-pumped Nd:$LiYF_4$ laser[20]. This laser operates at the same wavelength and repetition frequency as its predecessor. The maximum average output power at 1 kHz is specified to 20 W, but up to 24 W were used. The advantages of diode-pumping over pumping with flashlamps is a better pulse energy and beam pointing stability, a better beam profile, a smaller electric energy consumption, easier handling and longer lifetimes of diodes compared to flashlamps.

Chirped pulse amplifier

The amplification of the pulses from the oscillator ("seed" pulses) employs the chirped pulse amplification technique [102]. To keep the peak intensity of the pulses during amplification below the damage threshold and to avoid nonlinear effects, a seed pulse is first temporally stretched by a factor of up to 10^4. The energy of such a stretched pulse is enhanced in an amplification process. Finally, the pulse is recompressed to near its original duration.

In the pulse stretching process, different spectral components in the pulse are first spatially separated by a stretcher grating. The "blue" components are passed through a longer optical path then the "red" ones. Therefore the "blue" part of the spectrum is delayed with respect to the "red" one. Such a pulse is said to be positively chirped, i.e., its frequency increases from the leading to the trailing edge of the pulse. In a similar manner, pulse compression is achieved. This time a negative velocity dispersion is introduced, i.e., the "red" components have a longer optical path than the "blue" ones, so that the positive group velocity dispersion of the stretcher and optical components is compensated.

The maximum spectral width of the pulses that could be stretched and compressed was limited to 11 nm by the length of the gratings. To amplify shorter pulses having larger spectral widths, while maintaining the maximum angular dispersion, the stretcher and compressor gratings with a larger constant should be used. After replacing the original gratings with 1200 grooves/mm by ones with 1800 grooves/mm[21], shorter pulses with a spectral width of typically 14 nm could be stretched, amplified and compressed.

After being stretched, a seed pulse enters the cavity of the regenerative amplifier. There it is amplified by traversing through a Ti:Sapphire crystal pumped by 10 W from the Nd:YLF laser. Since the pump laser delivers pulses with a repetition frequency of 1 kHz, only a small portion of the seed pulses are amplified. After 15 round trips through the cavity, the pulse energy reaches saturation. The pulse is switched out through a thin film polarizer after its polarization is changed by means of a Pockels cell. A second stage of the amplification takes place in a double-pass amplifier. Here the pulse passes twice through a Ti:Sapphire crystal pumped by 12.5 W from the Nd:YLF laser. Typically, a pulse energy of about 1.6 mJ at the output of the regenerative amplifier was increased to 2.3 mJ after the first pass and 3.2 mJ after the second pass in the double-pass amplifier. After compression, the output pulses had an energy of 2.3 mJ and a duration of about 80 fs (FWHM). For

[20] Spectra Physics, Evolution-30
[21] Spectrogon, PC 1800

comparison, in the previous setup utilizing the Nd:YAG laser as the pump laser and the original stretcher and compressor gratings, the laser delivered pulses with an energy of 1.2 mJ and a duration of 130 fs.

3.3.2 Beam and pulse characterization

After leaving the amplifier, the horizontally polarized laser beam first passed through a half-wave plate, which rotated the polarization to vertical. As discussed in Section 3.2.2, vertical polarization is needed for the purposes of fragment imaging. To adjust the polarization, a Glan polarizer is inserted into the beam and rotated in such a way that the propagation axis of the reflected beam was precisely horizontal. This is achieved by measuring the height of the beam spot on a wall. For such orientation, the Glan polarizer transmits the horizontal component of the laser polarization. By minimizing the transmitted power, the orientation of the $\lambda/2$ plate for the required vertically polarized light is achieved.

The height of the laser beam was matched to the height of the ion beam by means of two mirrors. The focusing is achieved with an achromatic doublet[22], which optimally concentrates the pulse energy in space and time by eliminating two effects occurring in singlet lenses: (i) different temporal delays of different spatial components of the beam, and (ii) focusing of different spectral components at different points on the optical axis [103]. A focal length of $f = 300$ mm provided a focused beam diameter sufficiently small for achieving peak intensities above 1×10^{15} W/cm^2. The lens was mounted on a xyz-translation stage providing a precise alignment of the overlap of the ion and laser beams.

The pulse energy could be varied with a circular variable neutral density filter[23]. For a stronger attenuation, metallic and absorptive neutral density filters of different optical densities were used. The use of a combination of a $\lambda/2$ plate and a Glan polarizer was abandoned because of both the energy losses and a relatively large group velocity dispersion in the polarizer glass. The pulse energy was measured with a powermeter[24] placed behind the variable neutral density filter. The actual pulse energy inside the chamber was 9% smaller due to the losses on the mirrors, focusing lens and window on the vacuum chamber. Pulse-to-pulse energy fluctuations were monitored with a high-speed silicon detector[25] connected to a digital storage oscilloscope[26]. For this purpose, the peak values of 1000 pulses were taken and statistically analysed. The standard deviation of such a sample was 1–2 % of the mean value.

The autocorrelation and the beam profile could be easily measured by redirecting the beam to an autocorrelator[27] or a CCD camera using mirrors in flipper mounts[28] (M2 and M3 in Fig. 3.11).

[22] Melles Griot
[23] CVI Laser
[24] Coherent, Labmaster with head LM3
[25] Thorlabs, DET210
[26] LeCroy, Wavepro 960
[27] APE, PulseCheck
[28] New Focus, model 9891

Autocorrelation

To account for pulse broadening in the optical elements, the optical path lengths from the laser to (i) the interaction region and (ii) to the autocorrelator were chosen to be approximately equal. Two BK7 windows (W) with thicknesses of 5 and 10 mm placed in front of the autocorrelator simulated the pulse broadening in focusing lens L1 and the window on the vacuum chamber. The beam was attenuated by two glass reflections on prisms P1 and P2 and a neutral density filter. The typical measured autocorrelation signal is displayed in Fig. 3.12. The autocorrelation function was fitted by a Gaussian shaped pulse. The pulse duration τ_p can be calculated as [103]

$$\tau_p = \tau_{ac}/\sqrt{2}\,, \tag{3.18}$$

where τ_{ac} is the FWHM of the Gaussian fit to the autocorrelation function. The typically measured pulses of about 90 fs in duration were broader by about 10 fs than when measured directly at the output of the laser.

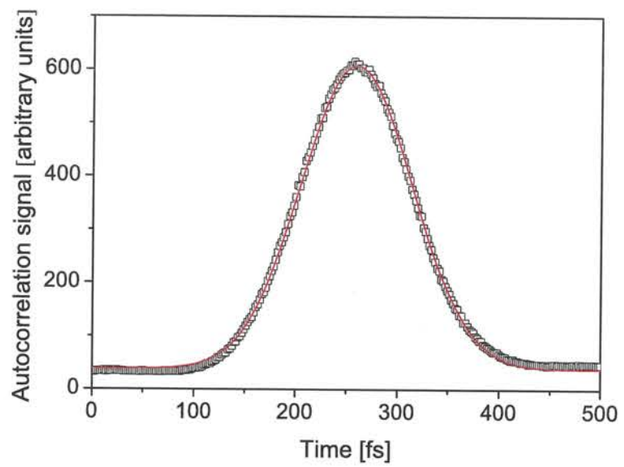


Figure 3.12: Autocorrelation function. The solid line is a fit to a Gaussian distribution corresponding to the pulse duration of $\tau_p = 91$ fs.

Laser beam profile

The laser beam profile, i.e., its energy distribution across the beam in the focal region, was measured by a CCD camera[29] and a laser beam analyser[30]. The attenuated beam was deflected by mirror M3 and focused in front of an objective lens (L2) with a focal length

[29] Cohu Solid State Camera, model 4812-7000
[30] Spiricon, LBA-100A

of $f = 200$ mm (Fig. 3.11). The lens was used to magnify the beam profile in the focal region onto the CCD chip, since the pixel size of the CCD chip of 13.5 μm was too large for direct imaging. The objective lens was mounted on a mirror holder allowing precise alignment of the lens. Its position along the beam was adjusted by a translation stage. In the first step, focusing lens L1 is adjusted so that the interaction region is exactly in the focus of lens L1. This is achieved by detecting the fragments and maximizing the signal of a high-intensity process, such as net two-photon absorption or Coulomb explosion. In the next step, the imaging lens L2 is shifted along its axis until the size of the beam profile on the CCD is smallest. At this point the objective lens images the same cross section of the beam as it is in the interaction region. Any change of the beam profile, which could be realized by shifting the focusing lens, will thus be reproduced accurately on the CCD sensor. The distance between lens L2 and the CCD camera was 170 cm, which yielded a magnification factor of 7.5, as calculated from the lens equation. A strong attenuation of the beam was achieved by a set of neutral density filters of different optical densities that were placed in front of the camera.

Figure 3.13 displays a typical beam profile measured in the focal plane of the lens. The beam was characterized by a laser beam analyser using the so-called knife-edge technique [104]. The value of the diameter where intensity falls to $1/e^2$ of its maximum intensity was $2w = 59$ μm.

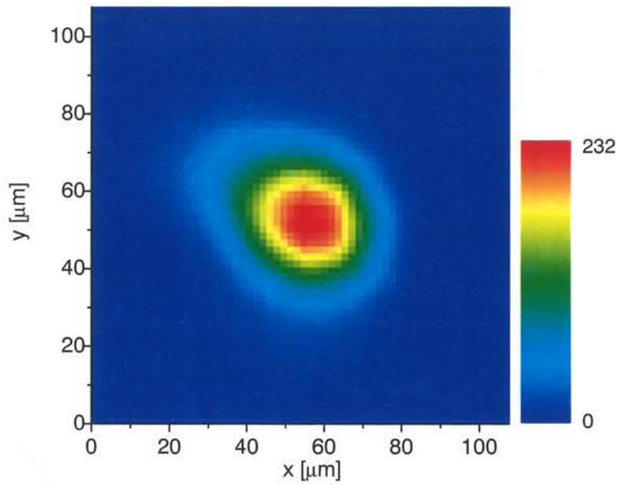


Figure 3.13: Laser beam profile in the focus of a $f = 300$ mm achromatic lens as measured by the CCD camera imaging system. The image covers 60×60 pixels of the CCD camera. The $1/e^2$ diameter of the beam is $2w = 59$ μm.

The laser peak intensity at the ion beam was varied by shifting the focusing lens along the laser propagation axis. Thereby, the size of the beam in the interaction region was

altered, while the pulse energy remained the same. The dependence of the beam diameter on the lens position is shown in Fig. 3.14. In this way laser peak intensities spanning two orders of magnitude could be covered without decreasing the pulse energy. The larger interaction volumes resulted in stronger signals at low intensities, which was particularly important for the Coulomb explosion measurements at lower intensities. Moreover, the beam diameters were much larger than the width of the ion beam, and hence the intensity variations along the laser polarization axis could be neglected. The variations along the laser propagation axis on the scale of the width of the ion beam were small as well. Thus the intensity variations were limited basically to only one dimension. The intensity distribution in the interaction region is discussed in Section 3.4.

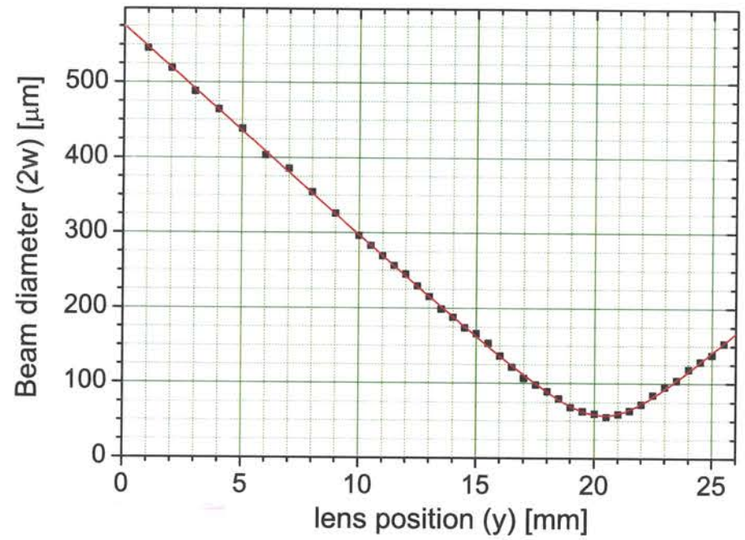


Figure 3.14: The variation of the laser beam diameter in the interaction region with the position of the focusing lens along the laser propagation axis. The solid line is a fit to Eq. (3.19), which was used to determine the peak intensities in the interaction region.

The diameter $2w$ of a non-Gaussian beam propagating along the y axis is described by the equation [105]

$$w(y) = w_0 \sqrt{1 + \left[M^2 \frac{\lambda}{\pi {w_0}^2} (y - y_0) \right]^2} , \tag{3.19}$$

where w_0 is the beam radius (waist) in the focal plane $y = y_0$. The parameter M^2 describes the deviation from a diffraction limited TEM_{00} mode, for which $M^2 = 1$. The best fit to the data in Fig. 3.14 yields the values $2w_0 = 57$ μm and $M^2 = 1.6$.

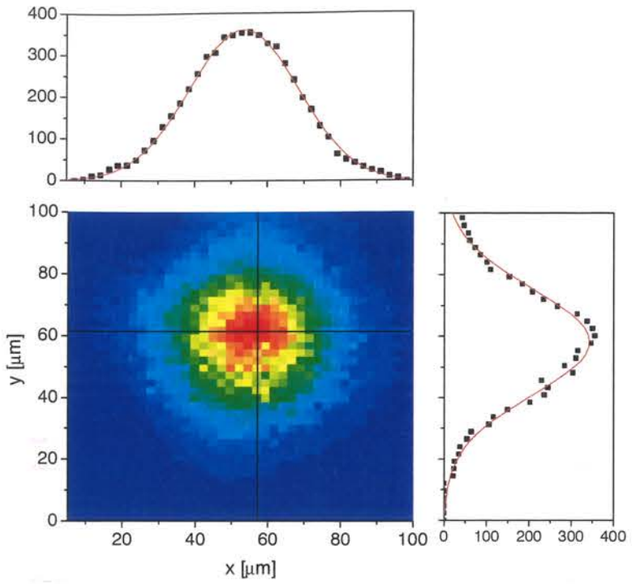


Figure 3.15: The laser beam intensity profile measured in the focus of a $f = 300$ mm achromatic lens by means of a scanning pinhole followed by a photodiode. The scanning step was 2.4 μm along both axes. The horizontal and vertical profiles were fitted by Gaussian distributions with diameters $2w_x = 60$ μm and $2w_y = 69$ μm.

The laser beam profile was also directly measured in Chamber 3 by means of a mechanical scanning method. A small pinhole drilled by a laser pulse was scanned across the focused beam and the transmitted signal was measured by a photodiode. The signal was transferred to a digital oscilloscope[31], from which its mean gated value was read out via an IEEE interface. The pinhole was scanned stepwise row by row across the beam profile by means of translation stages. The mechanical movement was realized with two step motors[32], which were controlled by a software via an IEEE interface. The minimum scanning step of 1.2 μm provided a resolution better than obtained by the CCD camera imaging system.

Figure 3.15 shows a typical beam profile in the focal plane measured by this method. The horizontal and vertical profiles were fitted by Gaussian distributions with diameters $2w_x = 60$ μm and $2w_y = 69$ μm. The beam diameter measured by this method is in a good agreement with the CCD based measurements.

[31] Tektronix, TDS 350
[32] Conrad Electronic

3.3.3 Laser intensity

The intensity distribution across a laser beam with an elliptical Gaussian spatial profle and a Gaussian time dependence is defined by the expression

$$I(x, y, t) = I_0\, e^{-2x^2/w_x^2}\, e^{-2y^2/w_y^2}\, e^{-2t^2/\tau^2}\,, \tag{3.20}$$

where I_0 is the peak intensity, and w_x and w_y are $1/e^2$ widths along the major and minor axes. The parameter τ is related to the FWHM pulse duration τ_p through $\tau_p = \sqrt{2\ln 2}\,\tau$. The integral of the laser spatial and temporal distribution is equal to the pulse energy E_p:

$$E_p = \int_{-\infty}^{\infty}\int_{-\infty}^{\infty}\int_{-\infty}^{\infty} I(x, y, t)\, dx\, dy\, dt = I_0\Big(\frac{\pi}{2}\Big)^{3/2} w_x w_y \tau\,. \tag{3.21}$$

For a radial Gaussian beam of $1/e^2$ width w ($w = w_x = w_y$) and the FWHM pulse duration τ_p, the peak laser intensity can be calculated from

$$I_0 = \frac{4\sqrt{\ln 2}E_p}{\pi^{3/2}w^2\tau_p} \tag{3.22}$$

by measuring the pulse energy, beam profile and pulse duration.

3.4 Intensity distribution in the interaction region

The molecules in the interaction region experience different intensities due to the spatial variations of the laser intensity. The following section discusses this effect and its influence on the measured signal.

3.4.1 Interaction volume

The spatial dependence of the intensity distribution of a radially symmetric Gaussian beam propagating along the y axis is given by [106]

$$I(r, y) = \frac{I_f}{1 + (y/y_R)^2}\, \exp\left(-\frac{2r^2}{w_0^2\,[1 + (y/y_R)^2]}\right). \tag{3.23}$$

Here I_f and w_0 are, respectively, the peak intensity and the width of the laser beam at the focus, and r is the radial distance in the plane perpendicular to the laser propagation axis (y axis). The distance $y_R \equiv \pi w_0^2/\lambda$, at which the beam radius has increased by a factor of $\sqrt{2}$, is called the Rayleigh range. For $w_0 = 30$ μm and $\lambda = 790$ nm, the Rayleigh range is $\sim$3.6 mm.

Inverting Eq. (3.23) for r at intensity $I = I_i$ yields the expression

$$r_i = \sqrt{\frac{w_0^2}{2}\,[1 + (y/y_R)^2]\,\ln\left(\frac{I_f/I_i}{1 + (y/y_R)^2}\right)}. \tag{3.24}$$

Equation (3.24) describes the surface of a constant intensity I_i. Such iso-intensity contours are illustrated in Fig. 3.16. It should be noted that the intensity increases much more rapidly along radial than along the axial axis. In the experiment, the width of the ion beam along the y axis was limited by the slits of widths $l = 200$–300 μm, which is much smaller than the Rayleigh range. Therefore intensity variations along the y axis can be neglected.

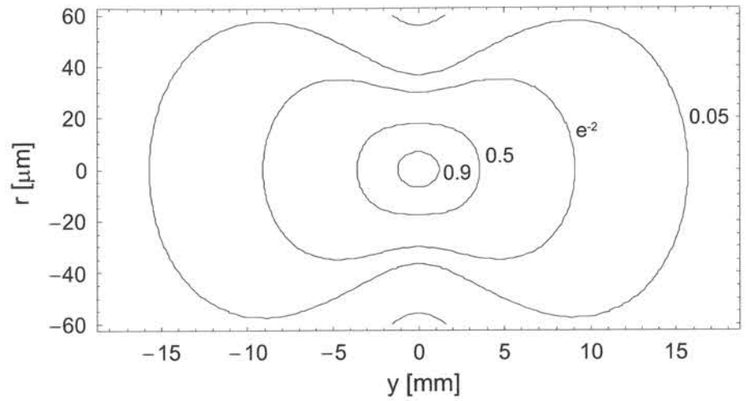


Figure 3.16: Spatial intensity distribution of a Gaussian beam at the focus, described by the axial and radial coordinates. The calculation was made for $w_0 = 30$ μm and $y_R = 3.6$ mm. The labels designate intensities at the contours in units of the maximum peak intensity I_f.

For a beam profile of width w and peak intensity I_0 (not necessarily at the focal point), the intensity distribution (3.23) becomes

$$I(r) = I_0\, e^{-2r^2/w^2}\,, \tag{3.25}$$

with iso-intensity contours described by

$$r_i = \sqrt{\frac{w^2}{2} \ln \frac{I_0}{I_i}}\,. \tag{3.26}$$

The volume of the interaction region with intensities $I > I_i$ can be calculated from the intersection of a cylinder of radius r_i and a box with dimensions h and l along the z and y axes, respectively (see Fig. 3.17). The intersection volume is given by

$$V(I > I_i) = \int_0^{r_i} r\phi(r) l \, \mathrm{d}r\,, \tag{3.27}$$

where

$$\phi(r) = \begin{cases} 2\pi & , \quad r \le h/2 \\ 4 \arcsin \frac{h}{2r} & , \quad r \ge h/2 \end{cases} \tag{3.28}$$

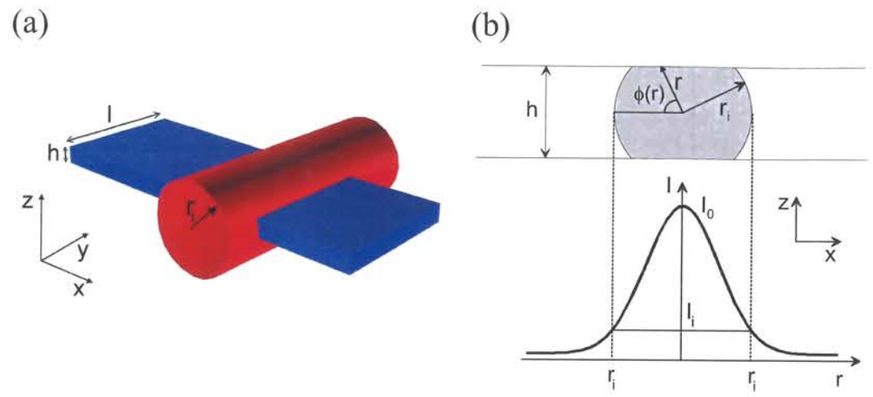


Figure 3.17: (a) Interaction volume defined by the intersection of a laser beam (shown as a cylinder) and an ion beam (box). (b) A cut in the x-z plane. The shaded area denotes the region with intensities $I > I_i$. The intensity distribution along the x axis is illustrated below.

[Fig. 3.17(b)]. Evaluating the integral yields the expression

$$V(I > I_i) = \begin{cases} r_i^2 l \pi & , \quad r_i \le h/2 \\ 2r_i^2 l \arcsin \frac{h}{2r_i} + r_i h l \sqrt{1 - \left(\frac{h}{2r_i}\right)^2} & , \quad r_i \ge h/2 \end{cases}\,. \tag{3.29}$$

Substituting the expression for r_i [Eq. (3.26)] into Eq. (3.29) one obtains

$$V(I > I_i) = \begin{cases} \frac{w^2}{2} l \pi \ln \frac{I_0}{I_i} & , \quad I \ge I_0\, e^{-\beta^2/2} \\ w^2 l \ln \frac{I_0}{I_i} \arcsin \frac{\beta}{\sqrt{2 \ln (I_0/I_i)}} + \frac{1}{2} h l w \sqrt{2 \ln \frac{I_0}{I_i} - \beta^2} & , \quad I \le I_0\, e^{-\beta^2/2} \end{cases}\,, \tag{3.30}$$

where β is defined as $\beta \equiv h/w$.

Equation (3.30) allows one to calculate the intersection volume containing intensities in the range between some intensity I_i and the laser peak intensity I_0. The dependence of $V(I > I_i)$ on the peak intensity I_0 is shown in Fig. 3.18 for $I_i = 10^{13}$ W/cm^2. The calculations were made with a laser beam width $w = 30$ μm and the ion beam dimensions $h = 25$ μm and $l = 300$ μm. Near the threshold intensity I_i, the interaction volume expands rapidly. At a peak intensity of 1.4×10^{13} W/cm^2, r_i reaches the value of $h/2$ and the volume expansion occurs along the x axis only.

In most of the related experiments, where the target is neutral H_2 or D_2 gas, the interaction region is not limited and the volume expands as $I_0^{1.5}$ [42]. For the laser-ion beam intersection calculated for the experimental parameters (Fig. 3.18), the volume expansion follows an $I_0^{0.13}$ dependence. Therefore, by choosing properly the widths of the ion and the laser beam, it is possible to a large extent to eliminate the volume expansion and large intensity variations over the interaction region.

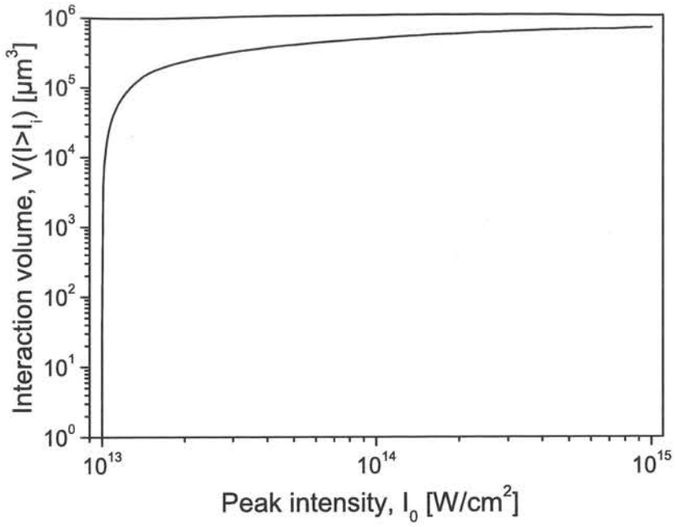


Figure 3.18: Interaction volume $V(I > I_i)$ as a function of the peak intensity I_0 for threshold intensity $I_i = 1 \times 10^{13}$ W/cm^2. The parameters used in the calculation were $w = 30$ μm, $h = 25$ μm and $l = 300$ μm.

3.4.2 Contribution of the intensity shells to the measured signal

To understand intensity dependent processes, it is important to know the sizes and contributions of different iso-intensity shells of the interaction volume to the measured signal. Differentiating Eq. (3.30) with respect to I_i leads to the expression

$$|\,\mathrm{d}V| = \begin{cases} \frac{w^2}{2}\, l\pi I^{-1}\,\mathrm{d}I & , \quad I \geq I_0\, e^{-\beta^2/2} \\ w^2 l \arcsin \frac{\beta}{\sqrt{2\ln(I_0/I)}}\, I^{-1}\,\mathrm{d}I & , \quad I \leq I_0\, e^{-\beta^2/2} \end{cases} . \tag{3.31}$$

Equation (3.31) describes the size of an infinitesimal volume $|\,\mathrm{d}V(r)|$ around intensity $I(r)$ for a peak intensity I_0. The distribution of $\mathrm{d}V/\mathrm{d}I$ over intensities I is illustrated in Fig. 3.19 for a peak intensity $I_0 = 1 \times 10^{15}$ W/cm^2. The area under the curves between intensities I_1 and I_2 is proportional to the volume $V(I_1 < I < I_2)$ of the corresponding shell. The calculations were done for different widths w of the laser beam. Without considering the relative amplitudes, they can also be interpreted as curves corresponding to different parameters $\beta = h/w$. For relatively large laser beam widths (small β), almost all intensities, except a narrow range around the peak intensity I_0, lie in shells $r > h/2$. Thus the shape of these curves basically stems from a one-dimensional Gaussian intensity distribution: At lowest intensities as well as at the peak intensity, the gradients $\mathrm{d}I(r)/\mathrm{d}r$ approach zero, which is reflected in the divergent behaviour of $\mathrm{d}V/\mathrm{d}I$ at low and high intensities. At intermediate intensities, the slope of the Gaussian distribution is nearly

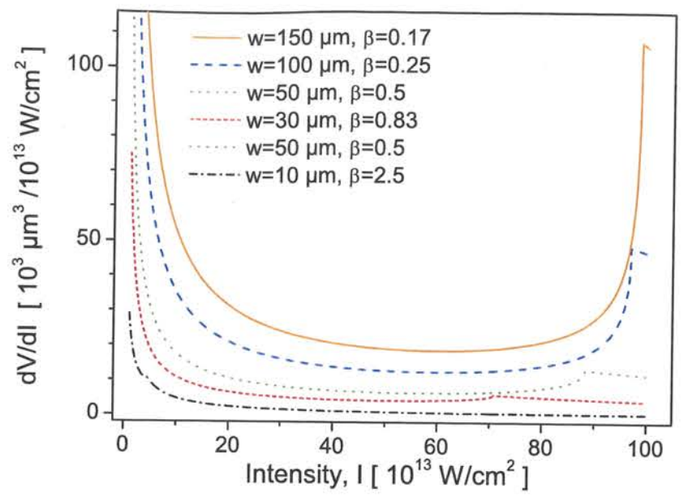


Figure 3.19: The gradient change of the volume of intensity shells, $\mathrm{d}V/\mathrm{d}I$, as a function of the intensity of the shells [Eq. (3.31)]. The calculations were made for the peak laser intensity $I_0 = 1 \times 10^{15}$ W/cm^2, and the ion beam dimensions of $h = 25$ μm and $l = 300$ μm. The curves are results of calculations for different laser beam widths, i.e., different parameters $\beta = h/w$.

constant, causing small changes in $\mathrm{d}V/\mathrm{d}I$. For intensities $I > I(r = h/2)$, the intensity shells are inside the radius $r < h/2$, where the function has a $1/I$ dependence. In Fig. 3.19 this change in the behaviour of the function occurs at $I = 9.9 \times 10^{14}$ W/cm^2 for $w = 150$ μm, while, for higher focused laser beams (higher values of β), the change takes place at lower intensities.

In the following example, two processes occurring at different intensities and resulting in fragments at similar kinetic energies will be considered. In order to distinguish the contributions of these processes, the relative volumes of intensity shells need to be calculated. If intensity shells with the same $\Delta I/I$ are considered, their volumes are according to Eq. (3.31), for $\Delta I/I = 0.1$, to a good approximation equal to

$$|\Delta V(\Delta I/I = 0.1)| = \begin{cases} \frac{1}{20}\, w^2 l\pi & , \quad I \geq I_0\, e^{-\beta^2/2} \\ \frac{1}{10}\, w^2 l \arcsin \frac{\beta}{\sqrt{2\ln(I_0/I)}} & , \quad I \leq I_0\, e^{-\beta^2/2} \end{cases} . \tag{3.32}$$

The dependence of the volumes $|\Delta V(\Delta I/I = 0.1)|$ on intensity is plotted in Fig. 3.20 for different widths h of the ion beam or, alternatively, for different parameters β. With $h \gg w$ all intensity shells are equally large, hindering the observation of the process of interest. By reducing the ion beam width or by using less focused laser beams, providing the pulse energy is sufficient, the contribution of low-intensity shells can be greatly reduced. This demonstrates that it is possible to effectively isolate a process occurring in a narrow

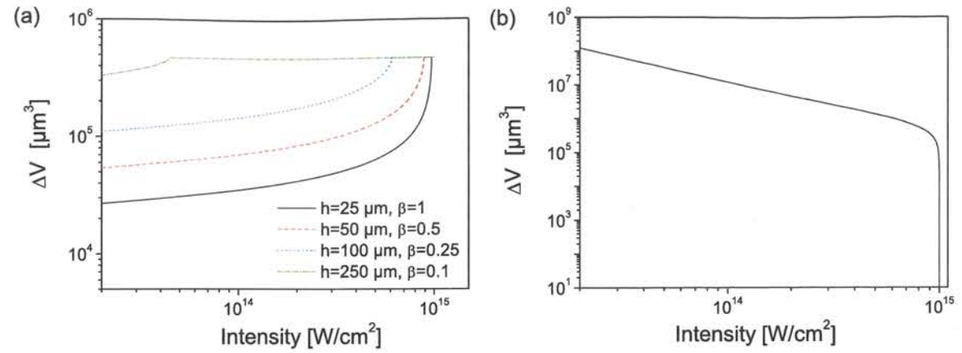


Figure 3.20: Volume of iso-intensity shells with $\Delta I/I = 0.1$ as a function of intensities in the interaction region. (a) ion beam of width $l = 300$ μm and different widths h [Eq. (3.32)]; (b) no constraints on the interaction volume [Eq. (3.33)]. The laser peak intensity and beam width are $I_0 = 1 \times 10^{15}$ W/cm^2 and $w = 30$ μm, respectively.

range of intensities near the peak intensity. This result is important for studies of processes near the threshold, such as Coulomb explosion, which will be discussed in Section 6.1.2

For comparison, without constraints on the interaction region, the volumes of iso-intensity shells are now given by [42]

$$|\Delta V(\Delta I/I = 0.1)| = \frac{\pi}{30} w_0^2 y_R (2I + I_0)(I_0 - I)^{\frac{1}{2}} I^{-\frac{3}{2}}. \tag{3.33}$$

The size of the volume of the intensity shells in this case is shown in Fig. 3.20(b). The volume of low-intensity shells is here several orders of magnitude larger than the volume of interest.

Chapter 4

Photodissociation of the deuterium molecular ion

This chapter presents measurements on photodissociation of D_2^+ in femtosecond laser fields of intensities up to 1.5×10^{14} W/cm^2. Section 4.1 discusses the energies of the vibrational levels of the electronic ground state of D_2^+ and presents experimental images resolving the fragments from single vibrational levels. In Section 4.2, the kinetic energy distributions of the fragments for different peak intensities are presented and discussed. Particularly, the bond softening effects: the shifting of the peaks to lower kinetic energies (level shifting) and broadening of the peaks with increasing laser intensity are analysed and discussed. The alignment of the fragments is investigated in Section 4.3. Besides the one-photon bond softening process, the angular distributions suggest the mechanisms of vibrational trapping and two-photon bond softening (above-threshold dissociation) to occur at highest intensities. In Section 4.4, the kinetic energy distributions of D_2^+ fragments are compared to those of H_2^+ measured by Sändig *et al* under similar experimental conditions [28].

4.1 Vibrationally resolved velocity distributions

In comparison with H_2^+, the vibrational levels of the heavier isotopic variant D_2^+ are characterized by smaller spacings between adjacent levels. The diagram in Fig. 4.1 illustrates the positions of the vibrational levels of the electronic ground state $1s\sigma_g$ of H_2^+ and D_2^+.

The potential of the binding ground state of H_2^+ and D_2^+ can be described by an anharmonic oscillator, with the energies of the vibrational levels given by [93]

$$E(v) = \omega_e \left(v + \frac{1}{2}\right) - \omega_e x_e \left(v + \frac{1}{2}\right)^2 + \ldots \quad v = 0, 1, 2, \ldots \tag{4.1}$$

Here ω_e is the fundamental frequency in the harmonic approximation and $\omega_e x_e$ is the anharmonicity constant. Both constants are expressed in units of cm^{-1} and their values for H_2^+ and D_2^+ are listed in Appendix B. Due to the anharmonicity, the spacing between successive vibrational levels decreases for higher vibrational levels. The average spacing

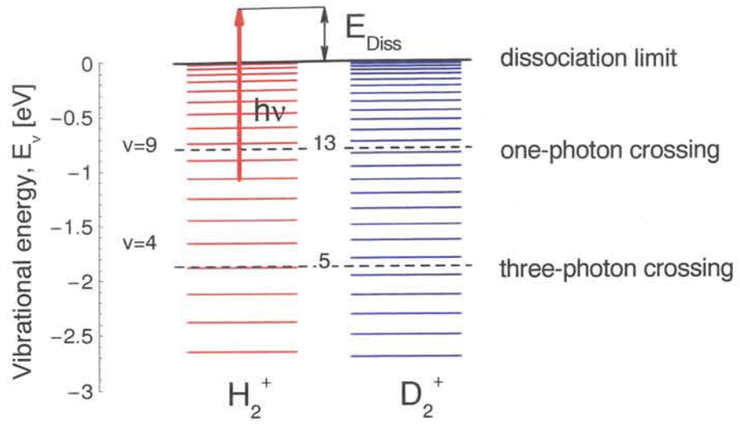


Figure 4.1: Schematic diagram showing in comparison the energies of the vibrational levels of H_2^+ and D_2^+ of the electronic ground state (the vibrational eigenvalues are listed in Appendix B). The dashed horizontal lines mark the energies of one- and three-photon avoided crossings (Figs. 2.2 and 4.8). Vibrational levels with largest Franck-Condon factors for one- and effective two-photon absorption are designated by numbers. The arrow illustrates a one-photon transition at $\lambda = 785$ nm ($h\nu = 1.6$ eV). The difference between the photon energy and the binding energy of a particular vibrational state is transferred into the kinetic energies of the photofragments.

can be characterized by constants ω_e, which are 2322 cm^{-1} (288 meV) and 1577 cm^{-1} (196 meV) for H_2^+ and D_2^+, respectively. Their ratio is equal to 1.47, which is close to $\sqrt{2}$, as expected for the ratio of oscillation frequencies of masses m and $2m$ in the harmonic approximation.

For the case of a weak laser field, the total kinetic energy of the photodissociation fragments is given by energy conservation (see Fig. 4.1)

$$E_{Diss}(v) = (nh\nu - |E_v|)/2\,, \tag{4.2}$$

where n is the effective number of photons absorbed. The factor 1/2 reflects the fact that in the case of homonuclear molecules, the dissociation energy is shared equally between the fragments. The energies of the vibrational levels E_v have negative values, where zero energy denotes the energy of the dissociation limit. The eigenvalues of the vibrational states of H_2^+ and D_2^+ are listed in Appendix B. For the photon energy $h\nu$ of 1.6 eV ($\lambda = 785$ nm), $v = 5$ is the lowest vibrational level for which photodissociation by absorption of one photon is energetically allowed. Photodissociation of all vibrational levels is possible if net two photons are absorbed.

In order to resolve fragments from single vibrational levels according to their velocities, the area of the MCP detector was here optimally used. The velocity of the ion beam was selected such that the fragments with the highest expected energy are displaced by

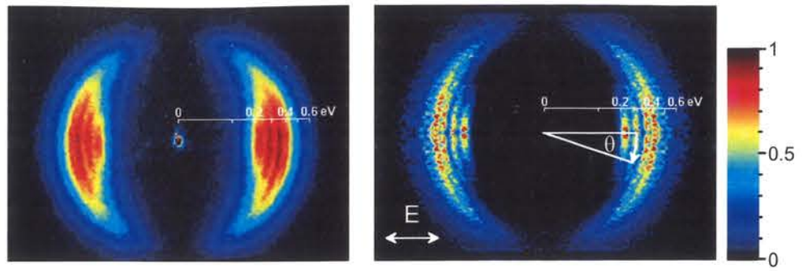
an amount close to the radius of the detection area [Eq. (3.16)]. For this reason, the acceleration voltage was reduced to $U_a = 3.1$ kV (instead of 11.1 kV in the measurements on H_2^+ in [28], [86]), which, however, decreased the ion current by a factor of ~4. Since the detection area was also by nearly the same factor larger, a reduction of the signal-to-noise was unavoidable. This could partly be compensated by longer measurements in which the data from $1 \times 10^7 - 2 \times 10^7$ laser shots were collected. For a sufficient number of photofragments, the measurements were done with a maximum pulse energy of about 1 mJ available with the previous pump laser. The peak laser intensity was varied by introducing chirp to the pulses. The pulses were focused on the ion beam by means of a $f = 375$ mm mirror. The laser beam diameter in the interaction region was estimated to be 110 ± 40 μm.

The measured vibrationally resolved velocity distributions of the neutral fragments at different laser intensities are shown in Fig. 4.2. The 2D projected distributions are displayed on the left side, while the right side shows the corresponding cuts through the 3D velocity distributions obtained by inverting the experimental images (Section 3.2.3). As described in Section 3.2, the radial distance from the center of the image is proportional to the fragment speed gained by the laser field. The corresponding kinetic energies are marked by the scale for the fragments ejected along the laser polarization axis. In Fig. 4.2(a), the fragments originating from molecules in different vibrational levels can be seen as circular features at different radii.

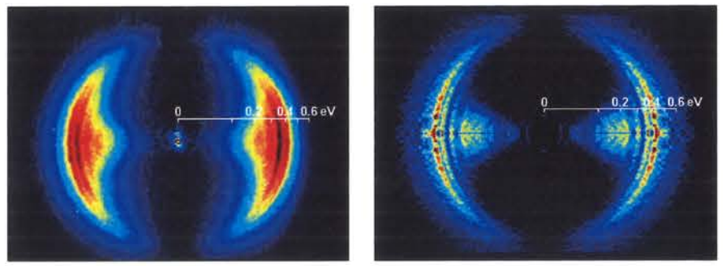
4.2 Kinetic energy distributions of the fragments

The kinetic energy distributions shown in Fig. 4.3 were obtained by summing the signal of pixels at the same radii, as indicated in Fig. 4.2(a). Each plot in Fig. 4.3 shows the kinetic energy spectra integrated over (i) a relatively small interval of angles (from -10° to 10°) and (ii) all angles (from -90° to 90°) with respect to the laser polarization axis. Whereas the former show the spectra for molecules experiencing nearly the same effective intensity (Section 4.3.1), the latter show the total number of fragments. The vertical lines (vibrational "comb") indicate the fragment energies expected for a low-intensity photodissociation of molecules in different vibrational states [Eq. (4.2)].

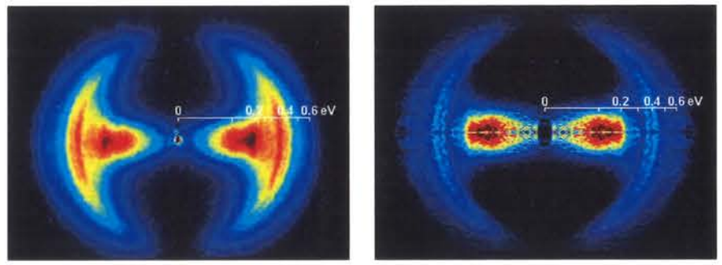
At the lowest intensity, the strongest peak corresponds to the level $v = 13$ [Fig. 4.3(a)], for which the Franck-Condon factors between the bound and the dissociative electronic state have maximum. Since the level $v = 12$ lies slightly below the crossing, its dissociation is also likely to occur at relatively low intensities. As a consequence of this "classical", weak-field dissociation, the angular distributions of the fragments from the levels $v = 12$ and $v = 13$ are broad [Figs. 4.2(a) and 4.5]. On the other hand, the levels $v = 11$ and $v = 10$ lie well below the dissociation limit, and hence dissociation of these levels is not possible in weak fields. However, due to the lowering of the potential barrier with increasing intensity, these levels can dissociate via the one-photon bond softening mechanism (Section 2.1.3). Since this mechanism is strongest along the laser polarization axis, the dissociation will mostly occur for those molecules that are better aligned with respect to the polarization



(a) 2×10^{13} W/cm^2, 920 fs



(b) 3.5×10^{13} W/cm^2, 510 fs



(c) 1.5×10^{14} W/cm^2, 140 fs

Figure 4.2: Velocity distributions of the neutral fragments resulting from photodissociation of D_2^+. Left: experimental 2D projected velocity distributions; right: slices through the 3D velocity distributions obtained after inverting the corresponding experimental images (Section 3.2.3). The laser polarization is along the horizontal axis in the plane of the image. The peak laser intensities and pulse durations are given for each measurement. The pulse energy was around 1 mJ in all measurements. The size of the imaged area on the phosphor screen along the polarization axis is 41 mm. In Fig. 4.2(a), θ indicates the angle between the laser polarization (symmetry) axis and the fragment velocity vector. The circular arc illustrates the integration of data with a certain kinetic energy, as employed for the kinetic energy distributions in Fig. 4.3.

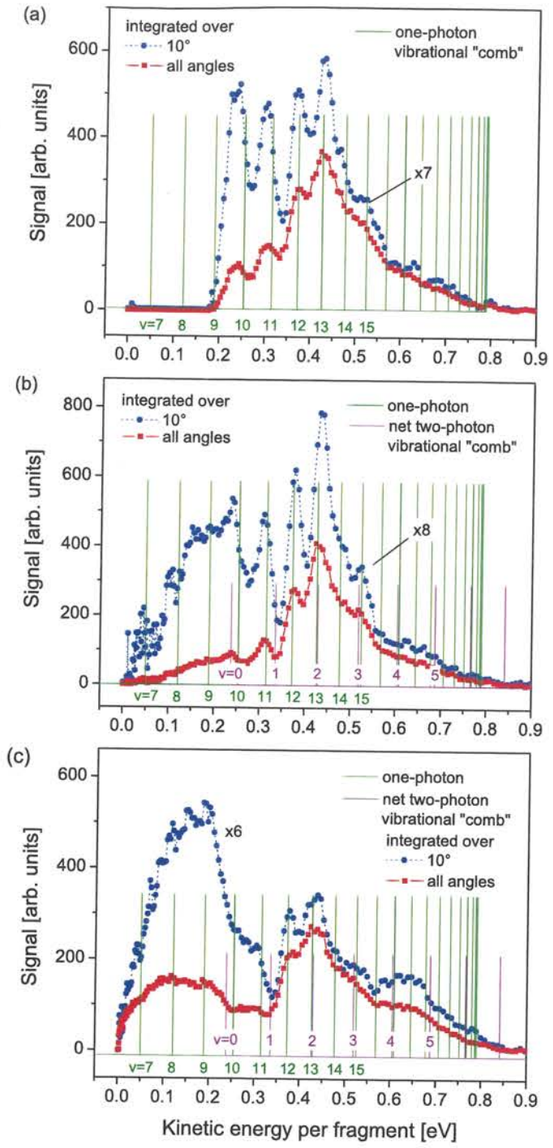


Figure 4.3: Kinetic energy distributions of the fragments for the measurements in Fig. 4.2. The distributions were obtained by integrating the inverted velocity distributions over (i) 10° (from -10° to 10°) and (ii) all angles (from -90° to 90°) around the laser polarization axis. The peak laser intensities and pulse durations are (a) 2×10^{13} W/cm^2, 920 fs; (b) 3.5×10^{13} W/cm^2, 500 fs; (c) 1.5×10^{14} W/cm^2, 140 fs.

axis. It should be noted that the number of the fragments from a particular vibrational level is not only determined by the photodissociation probability, but also by the initial vibrational population distribution (Section 3.1.1) and the intensity distribution in the interaction region (Section 3.4). This has been discussed in detail in calculations by Serov *et al* [45].

In comparison with the vibrational "comb", the peaks from the lower-lying vibrational levels appear to be shifted towards lower kinetic energies. To determine the magnitude of these shifts and the widths of the peaks, the kinetic energy distributions in Fig. 4.3(a) were fitted by a sum of Gaussian distributions. The results of the best fit are displayed in Fig. 4.4 and the parameters are summarized in Table 4.1. At an intensity of 2×10^{13} W/cm^2 the shift is largest for the lowest vibrational level $v = 10$ (approximately 20 meV). The level shifting effect was observed in the photodissociation spectra of H_2^+ by Sändig *et al* [28, 86]. In the work presented here, the magnitudes of the shifts of these measurements were determined and are given in Section 4.4. Several calculations simulating the experimental kinetic energy distributions confirmed this effect [45, 44, 57]. The measured spectra were best reproduced by Serov *et al* [45, 107], where the complete 3D molecular dynamics of H_2^+ was studied employing a wave packet propagation method.

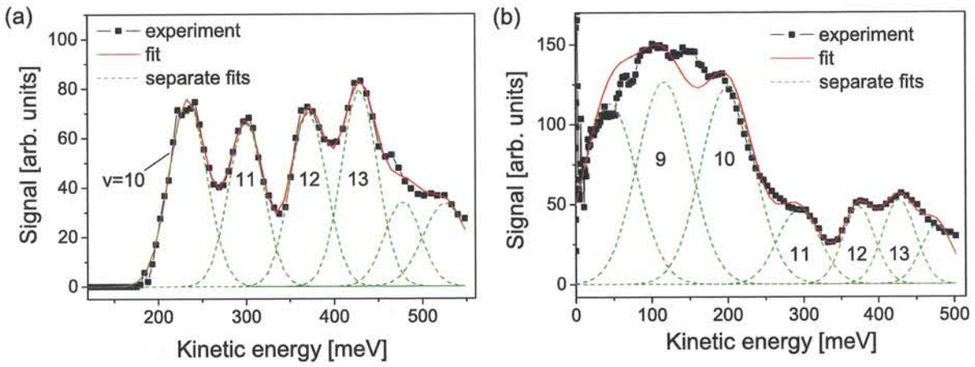


Figure 4.4: Fragment kinetic energy distributions at an intensity of (a) 2×10^{13} W/cm^2 and (b) 1.5×10^{14} W/cm^2 fitted by a sum of Gaussian distributions. The data in (a) were fitted with a constraint that the distributions $v = 12-14$ have the same widths. In (b), the fragments below 250 meV are not resolved. The distributions plotted in this energy range served to estimate the lower limit of the widths and to obtain more accurate results for the levels $v \geq 11$. The best fit parameters are given in Table 4.1.

Intuitively, the shifting of vibrational levels with respect to their field-free position can be explained by the deformed shape of the lower potential well in strong laser fields. For a fixed laser intensity, the potential well broadens at larger internuclear separations [see Fig. 2.2(b)]. Consequently, the new vibrational eigenstates acquire lower energies, leading to lower fragment kinetic energies.

Table 4.1: Parameters from the fit of the kinetic energy distributions of D_2^+ fragments in Fig. 4.4. The shift of the peaks is calculated with respect to the vibrational "comb" shown in Fig. 4.3. The errors in the central energy are estimated assuming an uncertainty of one pixel.

vibrational level	9	10	11	12	13
central energy [meV]					
2×10^{13}		234±5	300±6	371±6	429±7
1.5×10^{14}		200[a]	293±6	373±6	427[a]
energy shift [meV]					
2×10^{13}		-20±5	-15±6	-2±6	2±7
1.5×10^{14}		-54[a]	-22±6	0±6	0[a]
peak width [meV]					
2×10^{13}		50	47	48	48
1.5×10^{14}	>80	>80	66	50	51

[a] parameter fixed in the fitting procedure

A strong enhancement of the photodissociation of the low-energy fragments along the laser polarization axis was observed at higher intensities [Figs. 4.2(b) and 4.2(c)]. At these intensities the one-photon gap along the polarization axis is completely open, allowing dissociation of all the vibrational levels down to $v = 7$ (see Fig. 4.8). At highest intensities the contribution of the single vibrational levels is not more distinguishable. Here the intensity variations during the pulse cause large dynamic shifts of the vibrational levels, resulting in a broadening of the contributions of the single vibrational levels.

Figure 4.4(b) shows the results of the best fit of the kinetic energy spectra at an intensity of 1.5×10^{14} W/cm^2. The parameters given in Table 4.1 show that, in addition to the large broadening of the hump corresponding to the levels $v \leq 10$, the peak $v = 11$ is significantly broader as well. The broadening of the kinetic energy distributions of the low-energy fragments was confirmed in the one-dimensional calculations by Rebentrost [57]. There, the kinetic energy distributions for each of the levels $v = 7-9$ extends from 0 to 0.2 eV. Such overlapping of the fragments from several vibrational levels at low kinetic energies can partially explain the enhancement of the number of the fragments in this part of the spectrum. Besides the bond softening effect, Kondorskiy *et al* [44] attributed this enhancement also to Raman-type transitions. Namely, multiple bound-free-bound transitions between the $1s\sigma_g$ and $2p\sigma_u$ states induce a population transfer from the strongly coupled levels (here $v = 12$ and $v = 13$) to lower vibrational levels. In the next section, it will be explained that also the vibrational level $v = 6$ can contribute to the measured spectra.

The level shifting effect, which causes large broadening at higher peak intensities, can

be neglected at lower intensities[1]. In addition to the experimental width, the peak width is here determined by the following factors:

- *The finite lifetime of the vibrational states.* Nuclear wave packets spend a finite time in the binding ground state before the molecule dissociates. The uncertainty in energy is related to the lifetime τ through the Heisenberg relation

$$\Delta E \cdot \tau \sim \hbar . \tag{4.3}$$

  At the intensities used, the Rabi frequency [Eq. (2.1)] is much higher than the vibrational frequency, and thus the lifetime τ is on the order of magnitude of the oscillation period $T = 1/\nu$. Here ν is the oscillation frequency of a vibrational state v given by [93]

$$\nu(v) = (E_{v+1/2} - E_{v-1/2})/h . \tag{4.4}$$

  After extrapolating the energies of the vibrational levels, one obtains $T = 33$ fs for the oscillation period of the vibrational state $v = 10$ of D_2^+. From Eq. (4.3), this corresponds to an uncertainty in energy per fragment of ~10 meV. For the bond softening fragments at higher peak intensities, the lifetime and level shifting contributions to the resulting broadening cannot be disentangled.

- *The rotational population distribution.* The energies of rotational levels in the rigid-rotor approximation are given by [93]

$$E(J) = BJ(J+1), \tag{4.5}$$

  where J is the rotational quantum number and B is the rotational constant. For the ground electronic state and D_2^+, $B = 15.016$ cm^{-1} (~1.9 meV) [108]. With an assumption that the rotational states $J = 0-2$ of each vibrational level are occupied (Section 3.1.1), its contribution to the widths of the vibrational peaks in the kinetic energy spectra is ~6 meV.

- *The laser spectral width.* For the one-photon absorption process, the laser bandwidth $\Delta\lambda$ results in a spread of fragment kinetic energies [Eq. (4.2)]

$$\Delta E_{Diss} = \frac{1}{2} h\Delta\nu = \frac{1}{2} hc \frac{\Delta\lambda}{\lambda^2} . \tag{4.6}$$

  For $\lambda = 785$ nm and $\Delta\lambda = 12.5$ nm, ΔE_{Diss} is about 13 meV.

4.3 Angular distributions of the fragments

4.3.1 One-photon bond softening

Figure 4.5 shows the angular distributions of the fragments from different vibrational levels, as extracted from the inverted image in Fig. 4.2(a). The broadest angular distribution

[1]This also includes the dissociation of the levels lying at or above the one-photon crossing, which dissociate already on the rising edge of the pulse

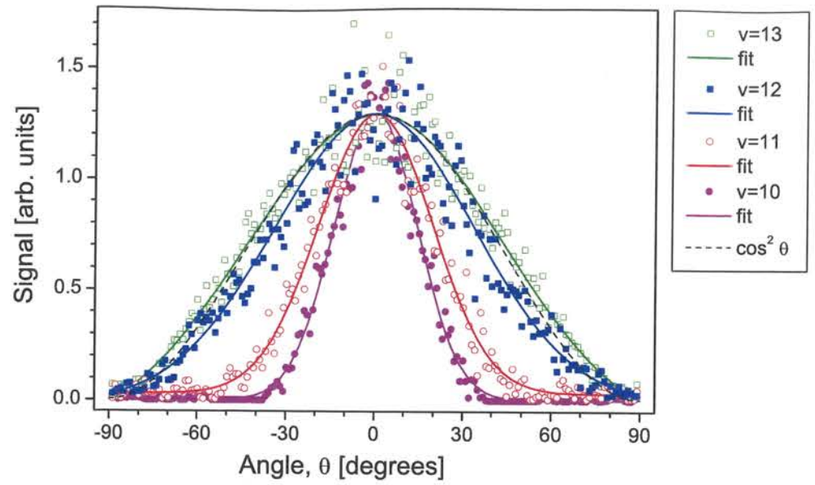


Figure 4.5: Angular distributions of the fragments from the vibrational levels $v = 10$ to $v = 13$, as extracted from the inverted image in Fig. 4.2(a). Each angular distribution is averaged over five adjacent radii to minimize the noise. The solid curves show fits to Gaussian distributions of FWHMs given in Table 4.2, together with the corresponding alignment parameters $\langle\cos^2\theta\rangle$. Here θ is the angle between the molecular and the laser polarization axis.

corresponds to the vibrational level $v = 13$. The reason for this is that it lies in the middle of the gap and thus is not affected by the light-induced potentials. Molecules at an angle θ relative to the laser polarization axis experience an effective or parallel intensity [65] determined by the projection of the laser electric field on the internuclear axis, i.e.,

$$I_{\text{eff}}(\theta) = I\cos^2\theta , \tag{4.7}$$

where I is the laser intensity. The angular distribution of the fragments $v = 13$ can be described well by a $\cos^2\theta$ distribution (Fig. 4.5), suggesting that the photodissociation probability for this level is linear in the effective intensity.

On the other hand, for the lower vibrational levels, which dissociate via bond softening, the photodissociation rate is nonlinear with the effective intensity. The height of the potential barrier is smallest for molecules aligned with the field ($\theta = 0°$, see Fig. 2.4), resulting in highest dissociation probabilities along the laser polarization axis. For larger angles, the increased height of the barrier leads to a rapid decrease in the dissociation probability, which is manifested in the narrowing of the angular distributions. The narrowing is most pronounced for the lowest vibrational levels, since only high parallel intensities, i.e., small angles, can lead to their photodissociation.

Table 4.2: FWHMs of Gaussian distributions and the alignment parameters $\langle\cos^2\theta\rangle$ of the angular distributions shown in Fig. 4.5. The peak laser intensity is 2×10^{13} W/cm^2 and the pulse duration is 920 fs.

Vibrational level	10	11	12	13
FWHM	$33.1 \pm 0.4°$	$45.3 \pm 0.7°$	$80 \pm 2°$	$102 \pm 4°$
$\langle\cos^2\theta\rangle$	0.93 ± 0.01	0.87 ± 0.01	0.76 ± 0.02	0.73 ± 0.03

The degree of alignment is often characterized by the average value of $\cos^2\theta$

$$\langle\cos^2\theta\rangle = \frac{\sum_{\theta_i=-90°}^{\theta_i=90°} P(\theta_i)\cos^2\theta_i}{\sum_{\theta_i=-90°}^{\theta_i=90°} P(\theta_i)}, \tag{4.8}$$

where $P(\theta)$ is angular distribution of fragments. The maximum alignment corresponds to $\langle\cos^2\theta\rangle = 1$. For a $\cos^2\theta$ distribution, $\langle\cos^2\theta\rangle = 0.75$. The alignment parameters of the angular distributions plotted in Fig. 4.5 are given in Table 4.2.

In Table 4.3, the dependence of the alignment on the peak laser intensity is illustrated for two measurements with the same pulse duration. Again, the fragments $v = 13$ have the broadest angular distribution. A larger deviation from the expected $\cos^2\theta$ distribution here can be attributed to saturation effects. Namely, at higher peak intensities, the photodissociation probability approaches unity not only for $\theta = 0°$, but also for larger angles. This weaker dependence on the effective intensity (i.e., angle θ) is reflected in a broadening of the angular distribution.

In addition to the narrowing of the angular distributions for the lower vibrational levels, Table 4.3 also shows a narrowing with increasing laser intensity. Whereas the first effect can be explained in terms of the angular dependence on the photodissociation probability

Table 4.3: The alignment parameter $\langle\cos^2\theta\rangle$ for different vibrational levels at two different intensities and the same pulse duration of 140 fs. For the bond softening fragments $v = 9-10$, the alignment parameter was calculated at kinetic energies of 0.15 eV (1.0×10^{14} W/cm^2) and 0.19 eV (1.5×10^{14} W/cm^2).

Intensity	Vibrational level			
	9–10	11	12	13
1.0×10^{14} W/cm^2	0.875 ± 0.02	0.75 ± 0.03	0.71 ± 0.03	0.71 ± 0.03
1.5×10^{14} W/cm^2	0.95 ± 0.01	0.88 ± 0.02	0.76 ± 0.02	0.71 ± 0.02

(i.e., geometric alignment), the latter is an indication of dynamic alignment (Section 2.1.4). Classically, higher intensities correspond to higher torques exerted on molecules. In the picture of light-induced potential curves, this corresponds to a deeper potential valley along $\theta = 0°$ in the lower adiabatic potential surface (Fig. 2.4). In both pictures, the result is an alignment of molecules with the laser field.

4.3.2 Vibrational trapping and two-photon bond softening

In order to analyse processes at the highest intensity ($I = 1.5 \times 10^{14}$ W/cm^2), the inverted velocity distribution in Fig. 4.2(c) was transformed to display the angle θ as a function of the fragment kinetic energy. Thereby, the data along each radius were normalized to unity. The obtained image shown in Fig. 4.6 exhibits two striking features: (i) broadening of the angular distribution at kinetic energies below 0.15 eV (see also Fig. 4.7), and (ii) its narrowing at kinetic energies above 0.6 eV. Both the features can be explained by an opening of the three-photon gap.

In the previous sections, the appearance of the fragments with low kinetic energies and narrow angular distributions was explained in terms of bond softening. This mechanism, however, cannot account for the broadening of the angular distributions of the low-energy fragments, as shown in Fig. 4.7. Although the widening of the one-photon gap for angles $|\theta| > 0°$ could explain this broadening, it would necessarily lead to a broadening of the angular distributions of the upper vibrational levels as well, which is in contrast to the observations in Figs. 4.6 and 4.7.

The observed broadening can be explained by the effect of vibrational trapping in light-induced potential wells. As explained in Section 2.1.4, in the vicinity of the three-photon avoided crossing X_2, the molecules will most probably follow the lower adiabatic curve $|u, n-3\rangle$ (Fig. 4.8). However, for the vibrational levels above the crossing (particularly $v = 6$), there is a probability of trapping in the potential well created above the three-photon gap [26]. This effect was experimentally observed in H_2^+ by Frasinski *et al* using 792 nm laser pulses of variable pulse lengths [27]. According to their explanation, the molecule first crosses the three-photon gap diabatically on the leading edge of the pulse. From the Landau-Zener formula [65], the probability for a diabatic transition is highest at low intensities because the width of the gap is rather small. After entering the potential well above the gap, the nuclear wave packet loses kinetic energy, turns back and arrives again at the gap. At this time the gap is much wider, and hence the probability of the diabatic crossing is small. The wave packet is now trapped in the potential well. As the intensity on the trailing edge of the laser pulse decreases, the shape of the upper adiabatic curve changes from concave to convex (see Fig. 4.8). Consequently, a portion of the nuclear wave packet is lifted up and finally ends up in the $|u, n-1\rangle$ state by effectively absorbing one photon.

The angular distribution of molecules dissociating via this scenario would be broadened for two reasons. (i) The distance between the adiabatic potential curves is smallest at lowest (effective) intensities, i.e., for θ close to 90°. Consequently, the probability for a diabatic transition is highest for these angles (there is no coupling for $\theta = 90°$). (ii) The potential

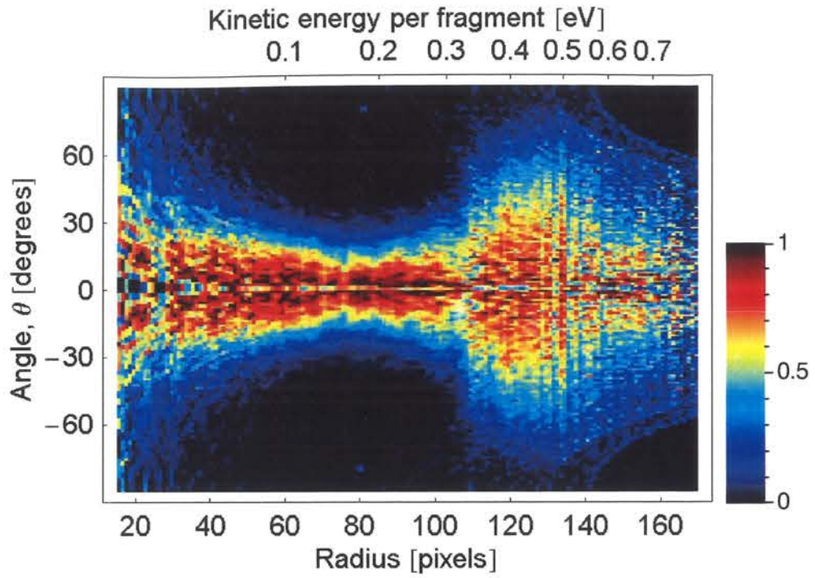


Figure 4.6: Number of fragments as a function of the angle θ and fragment speed (i.e., radius), as extracted from the inverted data in Fig. 4.2(c) (peak intensity of 1.5×10^{14} W/cm^2). The data on the same radius were normalized to unity. The noise in the data results from the inversion procedure and the normalization of these data.

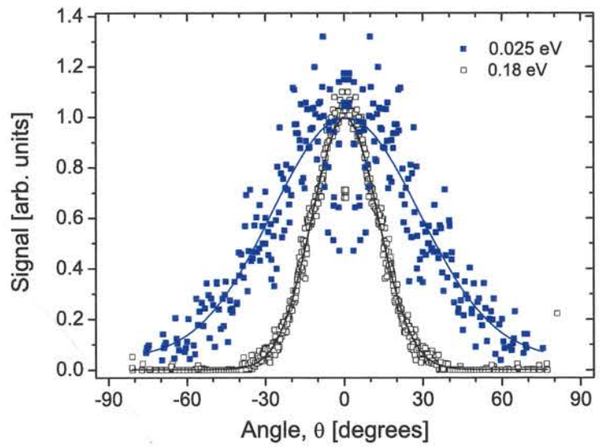


Figure 4.7: Angular distributions from Fig. 4.6 at kinetic energies of 0.025 eV and 0.18 eV (radii of 30 and 80 in Fig. 4.6). Each angular distribution comprises data at five adjacent radii. The solid lines show fits to Gaussian distributions with FWHMs of $56 \pm 3°$ and $29.5 \pm 0.2°$. The corresponding $\langle \cos^2 \theta \rangle$ parameters are 0.84 ± 0.04 and 0.954 ± 0.006, respectively.

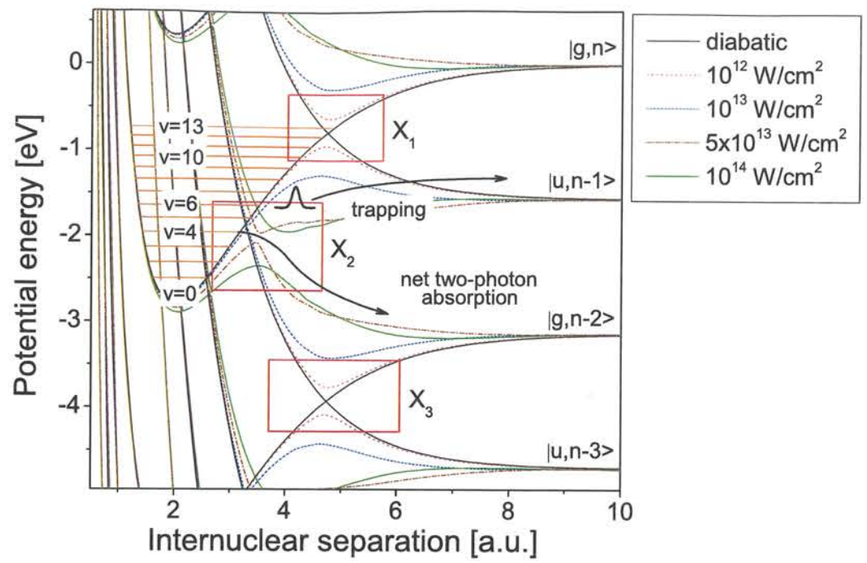


Figure 4.8: Diabatic and adiabatic dressed potentials curves for a wavelength of 790 nm. The horizontal lines indicate the positions of the D_2^+ vibrational levels in the absence of the laser field. The arrows illustrate the processes of vibrational trapping and two-photon bond softening. Curve-crossing regions are outlined by rectangles X_1, X_2 and X_3.

surface of the trapping state has a minimum along $\theta = 90°$, which results in a further misalignment. The measured low-energy angular distributions in Fig. 4.6 would be in this case a sum of a narrow angular distribution of the bond softening fragments and a broad distribution from the trapped molecules [30].

The seemingly unexpected one-photon dissociation of the level $v = 6$ lying below the dissociation limit is supported by the wave packet calculations by Rebentrost [57]. The energy gain surpassing the energy of one photon can be explained by absorption of photons that, compared to the emitted photons, are on average more in the higher-energy part of the laser spectrum. The final result of absorption of n and emission of $n - 1$ photons is effective absorption of one photon with an energy larger than the average photon energy [42].

The second feature observed in Fig. 4.6 is the appearance of the well-aligned fragments in the kinetic energy range of 0.6 to 0.7 eV. The fact that both the features appear simultaneously at the highest intensity supports the idea of vibrational trapping, because they both require opening of the three-photon gap. The comparison of the kinetic energies of the fragments with the vibrational "combs" in Fig. 4.3 suggests that the fragments originate from the levels $v = 4$ and $v = 5$ (possibly $v = 3$ as well) by a net absorption of two photons. From Fig. 4.8 it is clear that exactly these levels are expected to dissociate since they lie in the vicinity of the three-photon gap. After absorbing three photons, the

molecules follow the $|u, n-3\rangle$ state and emit one photon at the crossing X_2. Consequently, they end up in the $|g, n-2\rangle$ state, reflecting the effective absorption of two photons. The narrow angular distribution in Fig. 4.6 is a consequence of the bond softening mechanism, i.e., the angle-dependent width of the three-photon gap.

4.4 Comparison with measurements on H_2^+ at lower intensities

H_2^+ was studied under similar experimental conditions earlier in this group [86]. In order to compare the 3D velocity distributions and kinetic energy spectra of the two isotopic variants, the experimental images of Ref. [28] were inverted here. Figure 4.9 shows projected and inverted velocity distributions of the neutral fragments resulting from photodissociation of H_2^+ at a wavelength of 785 nm. The pulse energy is 1.0 mJ in both measurements and the pulse durations are 575 and 135 fs, corresponding to the peak intensities of 3.5×10^{13} and 1.5×10^{14} W/cm^2, respectively [28]. The calculated intensities may differ from that given in the D_2^+ measurements because of the uncertainty related to the different focused beam diameters in these measurements.

Figure 4.10 shows the kinetic energy distributions of the fragments extracted from the inverted images as discussed in Section 4.2. In distinction from D_2^+, in H_2^+ the peaks corresponding to single vibrational levels are more widely spaced, allowing to extend the vibrationally resolved study of bond softening to the lowest dissociating vibrational levels. The central energy and the widths of the peaks were determined by fits to Gaussian distributions as shown in Fig. 4.11. The results of the best fits are given in Table 4.4.

In comparison with D_2^+ (Table 4.1), the level shifting of the corresponding vibrational levels of H_2^+ is of a similar magnitude. This is to be expected, since level shifting is determined by the shape of the light-induced potential curves, which are the same in both cases.

In distinction from D_2^+, the widths of the peaks of H_2^+ are significantly broader. This suggests that the widths are primarily determined by the lifetimes of the vibrational states. In strong fields, the nearly resonant vibrational levels ($v = 9$ in H_2^+ and $v = 13$ in D_2^+) dissociate with a high probability every time the molecule approaches the outer turning point, i.e., the lifetime is comparable to the vibrational period. Since the oscillation period is shorter for H_2^+ [see Eq. (4.4)], according to the uncertainty principle [Eq. (4.3)], the spread of its fragment energies would be larger. At lower intensities, at which the peaks are best resolved, the widths of the $v = 9$ peak in H_2^+ and $v = 13$ peak in D_2^+ are 68 meV and 48 meV, respectively. Their ratio of 1.4 is surprisingly close to the inverse ratio of their oscillation periods.

It is interesting to note that at an intensity of 3.5×10^{13} W/cm^2 the width of the bond softening level $v = 6$ is smaller than that of the level $v = 7$ in Fig. 4.10(a). The smaller number of the fragments from the level $v = 6$ is a consequence of a lower photodissociation probability. The corresponding longer lifetime of this level would result in a smaller energy

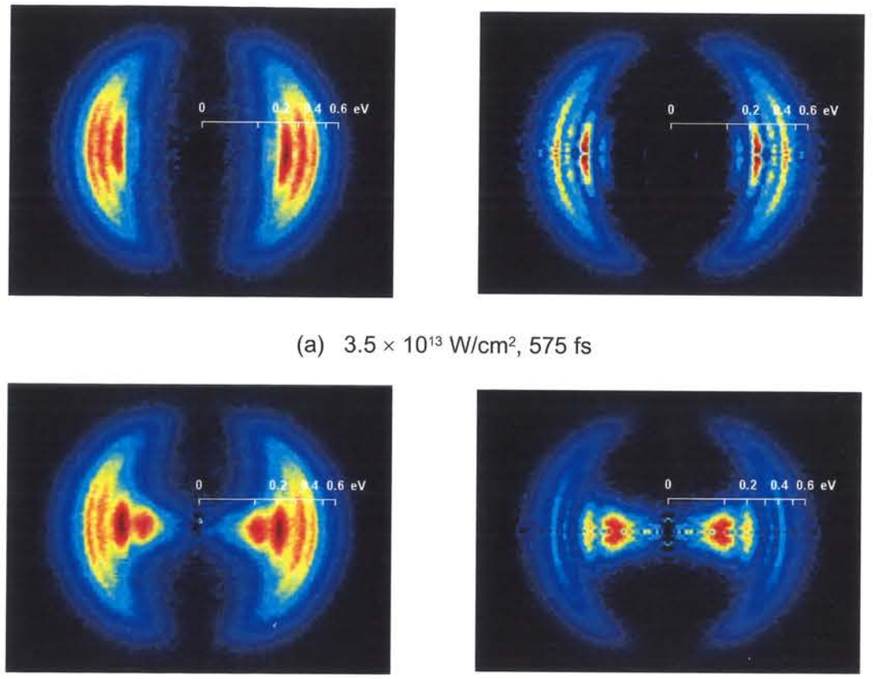


Figure 4.9: Velocity distributions of the neutral fragments resulting from photodissociation of H_2^+. Left: experimental 2D projected velocity distribution; right: slices through the 3D velocity distributions obtained after inverting the corresponding experimental images. The laser polarization is along the horizontal axis in the plane of the image. The size of the imaged area along the polarization axis is 23 mm. The pulse energy is 1.0 mJ. The peak laser intensities and pulse durations are given for each measurement.

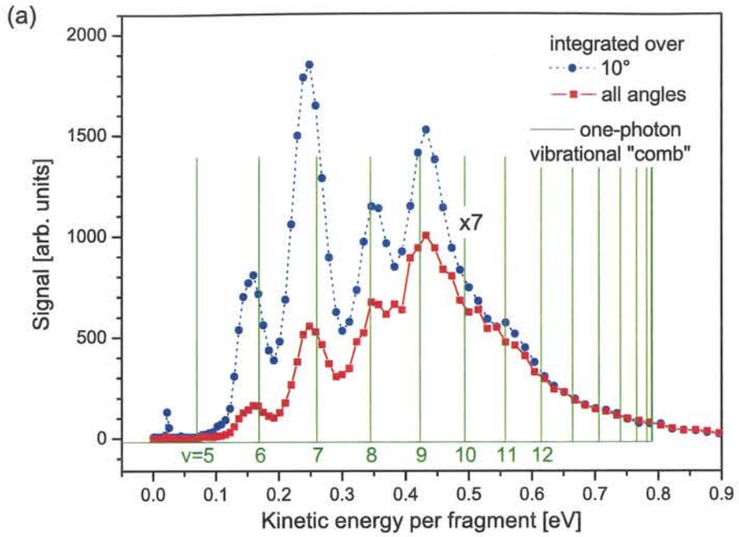


Figure 4.10: Fragment kinetic energy distributions from the inverted images in Fig. 4.9. The data were integrated over 10° and over all angles. The peak laser intensities and pulse durations are (a) 3.5×10^{13} W/cm^2, 575 fs; (b) 1.5×10^{14} W/cm^2, 135 fs.

spread, what is in qualitative agreement with the widths in Table 4.4.

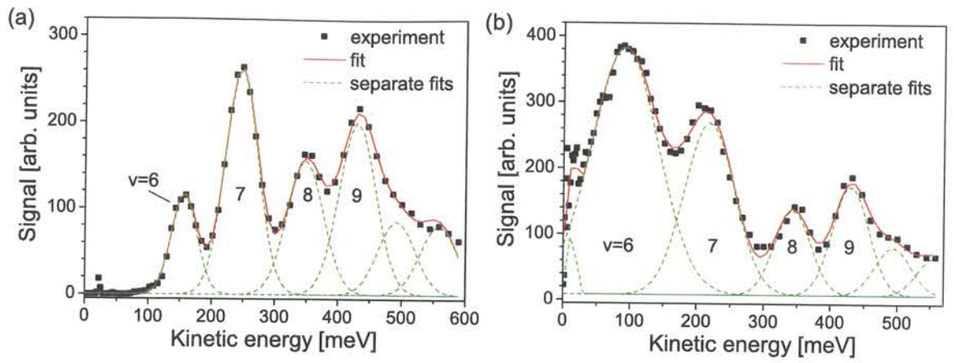


Figure 4.11: Fragment kinetic energy distributions at an intensity of (a) 3.5×10^{13} W/cm^2 and (b) 1.5×10^{14} W/cm^2 fitted by a sum of Gaussian distributions. The central energy and the widths of the peaks are given in Table 4.4.

Table 4.4: Parameters from the fit of the kinetic energy distributions of H_2^+ in Fig. 4.11. The shift of the peaks is calculated with respect to the vibrational "comb". The errors in the central energy are estimated assuming the uncertainty of one pixel.

vibrational level	6	7	8	9
central energy [meV]				
3.5×10^{13}	156±8	246±10	348±11	430±13
1.5×10^{14}	91±6	218±10	345±11	432±13
energy shift [meV]				
3.5×10^{13}	-12±8	-14±10	3±11	7±13
1.5×10^{14}	-77±6	-42±10	0±11	9±13
peak width [meV]				
3.5×10^{13}	47	61	68	68
1.5×10^{14}	119	88	63	63

Chapter 5

Photodissociation of the hydrogen molecular ion

The investigation of the strong-field photodissociation presented in the previous chapter is in this chapter extended to higher laser intensities. By using shorter pulses, larger pulse energies and stronger focusing, the peak laser intensities above 1×10^{15} W/cm^2 were achieved, allowing to investigate the two-photon bond softening process and Coulomb explosion. The photodissociation and Coulomb explosion channels were studied simultaneously by detecting both the charged and neutral fragments. In this chapter, results of the photodissociation of H_2^+ are discussed.

In Section 5.1, the velocity distributions of the fragments are shown in a series of images recorded at different peak intensities. The distributions are analysed by discussing the fragment kinetic energy and angular distributions. Attention is also given to the intensity distribution in the interaction region. In Section 5.2, the dependence of the alignment on the peak intensity is discussed for fragments at different kinetic energies. Furthermore, the widths of the angular distributions of the fragments from the different vibrational levels are compared. In Section 5.3, the dependence of the fragment yield of the one- (1ω) and net two- (2ω) photon process on the peak intensity is investigated.

5.1 Velocity and kinetic energy distributions of the fragments

Figure 5.1 shows an example of the velocity distribution measured at a peak intensity of about 1×10^{15} W/cm^2. The circular feature at energies below 0.9 eV corresponds to the neutral (H) and charged (H^+) fragments from the photodissociation channel. In addition, the protons from the Coulomb explosion channel can be seen at energies in the range from about 1 to 4 eV. These fragments were identified as Coulomb explosion protons in a separate measurement in which no fragments were observed when only neutral fragments were detected.

Since the experimental images are symmetric with respect to the vertical axis at zero

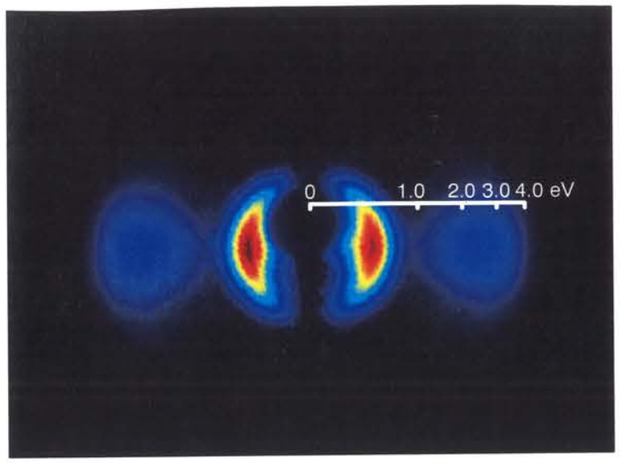


Figure 5.1: Projected 2D velocity distribution of the neutral and charged fragments resulting from the photodissociation and Coulomb explosion of H_2^+. Laser pulses of 130 fs in duration, a pulse energy of 1.75 mJ and a central wavelength of 785 nm were focused to a peak intensity of about 1×10^{15} W/cm^2. The scale marks kinetic energies of the fragments ejected along the laser polarization axis (horizontal axis). The circular feature below 0.9 eV corresponds to H and H^+ fragments from the photodissociation channel, while the one at higher kinetic energies are protons from the Coulomb explosion channel. Here the fragments with lowest energies were not recorded because of the Faraday cup used to block the ion beam and to measure the ion current (Section 3.1.4).

velocity, in order to increase the experimental resolution, it suffices to image only one side of the image. Practically, the fragment image on the MCP detector was enlarged by extending the distance between the interaction region and the detector [see Eq. (3.16)]. The whole imaged distribution was shifted from the center to the edge of the detector by slightly tilting the axis of the ion beam. Besides increased resolution, this method allowed to reduce the impact of the Faraday cup on the experimentally measured side by shifting the Faraday cup closer to the non-imaged fragments.

The velocity distributions of the fragments obtained in this way are shown in Fig. 5.2 in a series of images recorded at different peak intensities. The density plots in the left column display the measured velocity distributions (left), together with the corresponding inverted distributions (right), shown mirrored here. The 3D plots in the right column present the photodissociation part of the experimental images. Here, the data were mirrored and smoothed for the purpose of visualization. The corresponding kinetic energy spectra are displayed in Fig. 5.3.

In all measurements pulses with a duration of 96 fs, a central wavelength of 790 nm and the maximum available pulse energy of 2.1 mJ were employed. As explained in Section 3.3.2, the peak intensity was varied by shifting a $f = 300$ mm focusing lens along the

laser propagation axis and thereby altering the focused beam diameter in the interaction region. The advantage of this method over varying pulse energy by means of a $\lambda/2$ plate and a polarizer is that the larger interaction volumes resulted in more fragments at the same intensity. This allowed measurements spanning two orders of magnitude in intensity. Particularly at relatively low intensities, fast measurements with high signal-to-noise ratio could be carried out.

The focusing arrangement allowed the peak laser intensities to be varied from 2×10^{14} W/cm^2 to 1.5×10^{15} W/cm^2. In addition, three distinct measurements at lowest intensities are also included in Fig. 5.2 for completeness: in measurement a, the laser beam was not focused, while in measurements b and c the shifts of the lens from the focal position was much larger and could not be directly measured. For this reason, the peak intensities given for these measurements have larger uncertainties.

One-photon bond softening

The velocity distribution shown in Fig. 5.2(a) is typical of a weak-field photodissociation. In the absence of bond softening, photodissociation proceeds from the vibrational levels $v \geq 9$ with the maximum probability for the level $v = 9$, for which the Franck-Condon factor is largest. With increasing intensity, the molecules in the lower-lying vibrational levels $v = 8$ and $v = 7$ dissociate as a consequence of the barrier lowering (measurement b). A clear manifestation of the bond softening mechanism is the appearance of the strong and narrow peak $v = 7$ at an intensity of 2×10^{13} W/cm^2 (measurement c). A small hump at about 0.13 eV indicates photodissociation of the vibrational level $v = 6$. The level shifting of the peak $v = 7$ is here approximately 30 meV. With increasing intensity, the velocity distribution of the fragments broadens and extends to zero velocities. At a much higher intensity of 2×10^{14} W/cm^2 (measurement d), the potential barrier exists no more, allowing dissociation of the fragments from the vibrational levels $v \geq 5$. In the broad bond softening feature, no sign of the vibrational structure is observed (see Section 4.2 for discussion).

It is interesting to note that the relative number of the fragments from the levels $v = 7$ and $v = 6$ is considerably higher here than in the measurement at the similar intensity presented in Section 4.4. Here the laser beam diameter of $2w \sim 500$ μm was much larger than that in the measurement in Section 4.4 of about 100 μm [86] and also larger than the ion beam width of 50 μm. In Section 3.4 it was shown that if the laser beam diameter is large in comparison with the ion beam width, the processes occurring in the intensity shells close to the peak laser intensity are enhanced (Fig. 3.19). Compared to the levels $v \geq 8$, the dissociation of the levels $v = 7$ and $v = 6$ occurs at higher intensities, which are much closer to the peak intensity. For this reason the yield of these levels is enhanced, demonstrating this principle.

At intensities higher than 3×10^{14} W/cm^2, the bond softening signal starts to fall off, as indicated by the scaling factors in Fig. 5.3(a). The observed decrease is primarily caused by the smaller total interaction volumes due to stronger focusing at higher intensities. Furthermore, as discussed above, the relative volumes of the intensity shells that

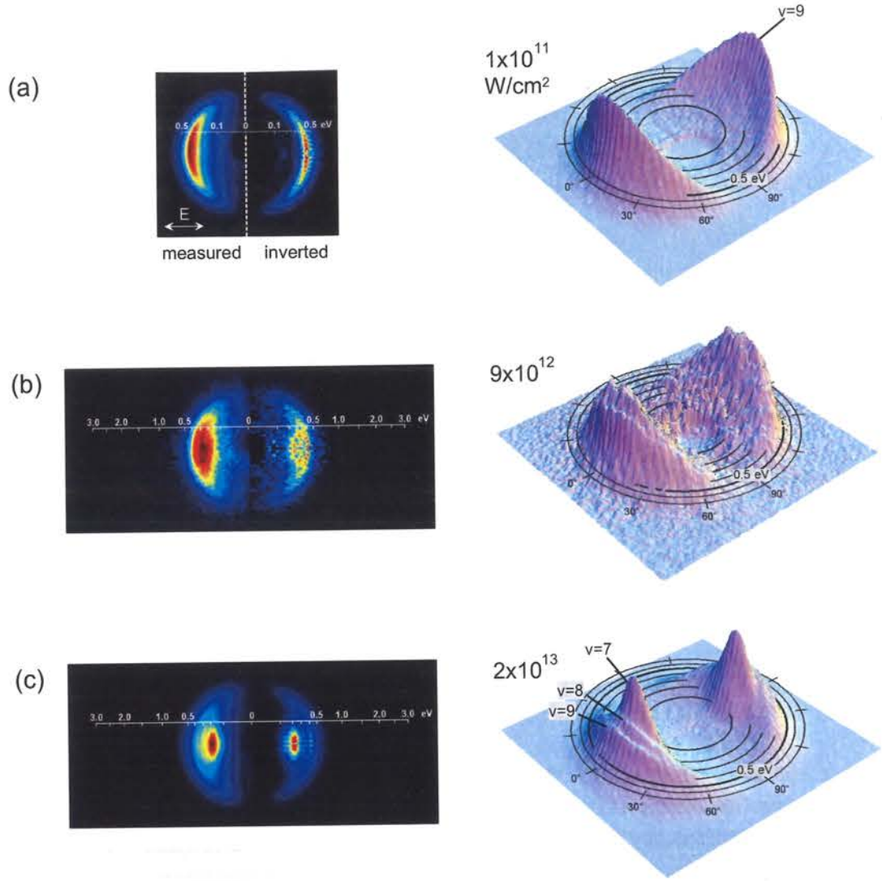


Figure 5.2: Velocity distributions of the fragments resulting from photodissociation and Coulomb explosion of H_2^+ at different peak intensities. Left column: the experimentally measured velocity distributions (left), together with the corresponding inverted distributions (right), shown as "mirror pairs" for the purpose of comparison. The inserted scale marks kinetic energies of the fragments ejected along the laser polarization axis (horizontal axis). The horizontal size of the imaged area is 27 mm. Right column: 3D plots presenting the photodissociation part of the measured data. For the purpose of visualization, the measured side was mirrored and the data were smoothed using a Gaussian filter. Each image is normalized to its maximum signal. The concentric circles mark kinetic energies with a step width of 0.1 eV. The ticks on the outer circle mark angles with respect to the laser polarization axis. The pulse energy is 2.1 mJ and the pulse duration is 96 fs in all measurements.

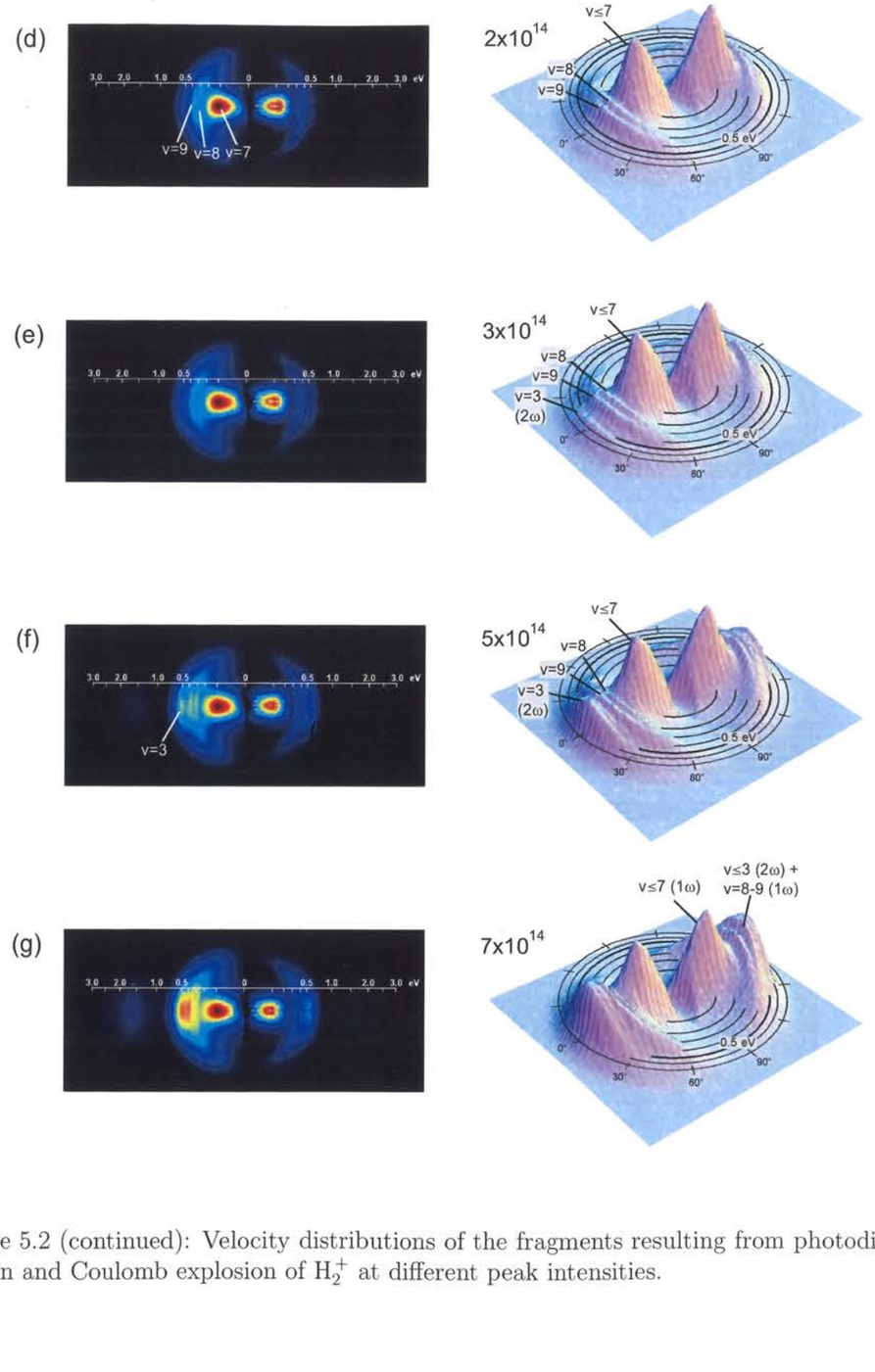


Figure 5.2 (continued): Velocity distributions of the fragments resulting from photodissociation and Coulomb explosion of H_2^+ at different peak intensities.

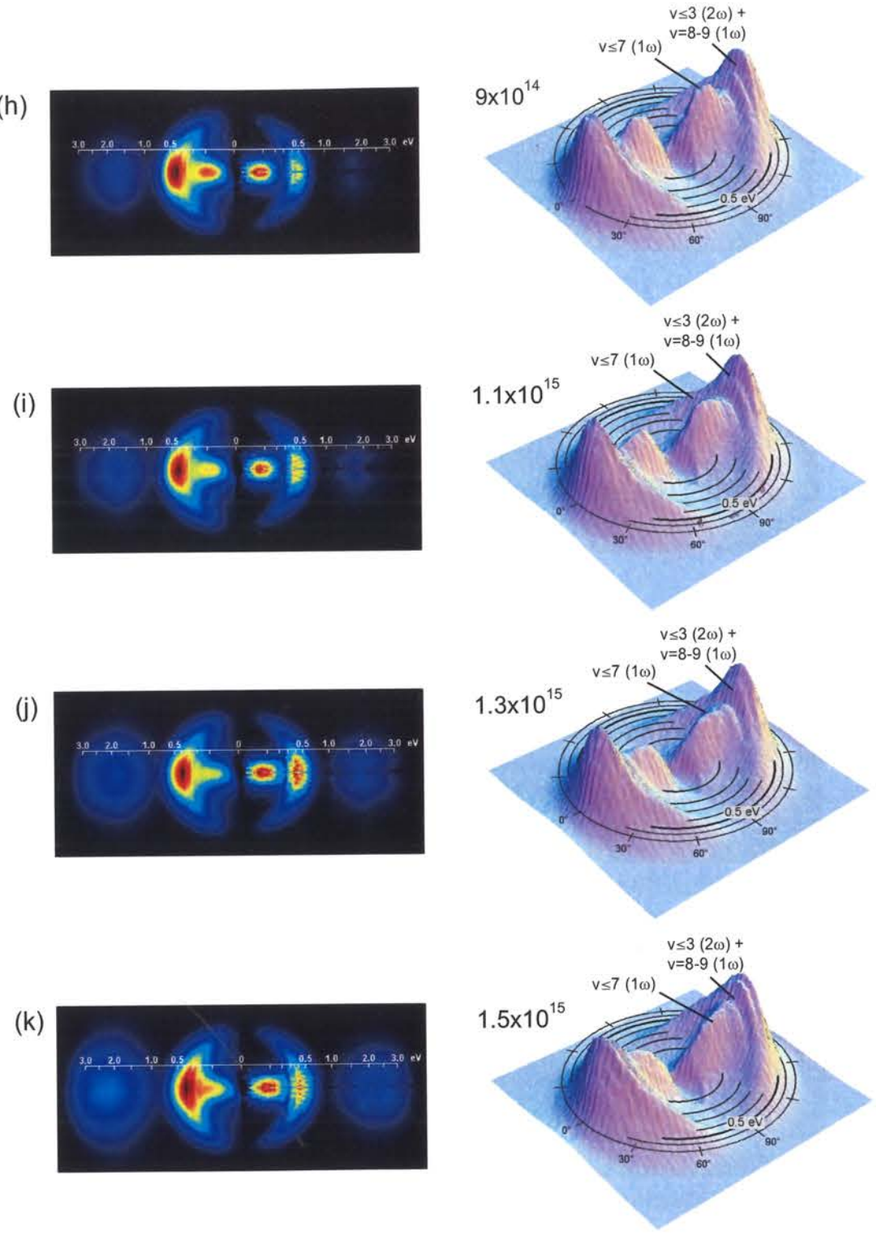


Figure 5.2 (continued): Velocity distributions of the fragments resulting from photodissociation and Coulomb explosion of H_2^+ at different peak intensities.

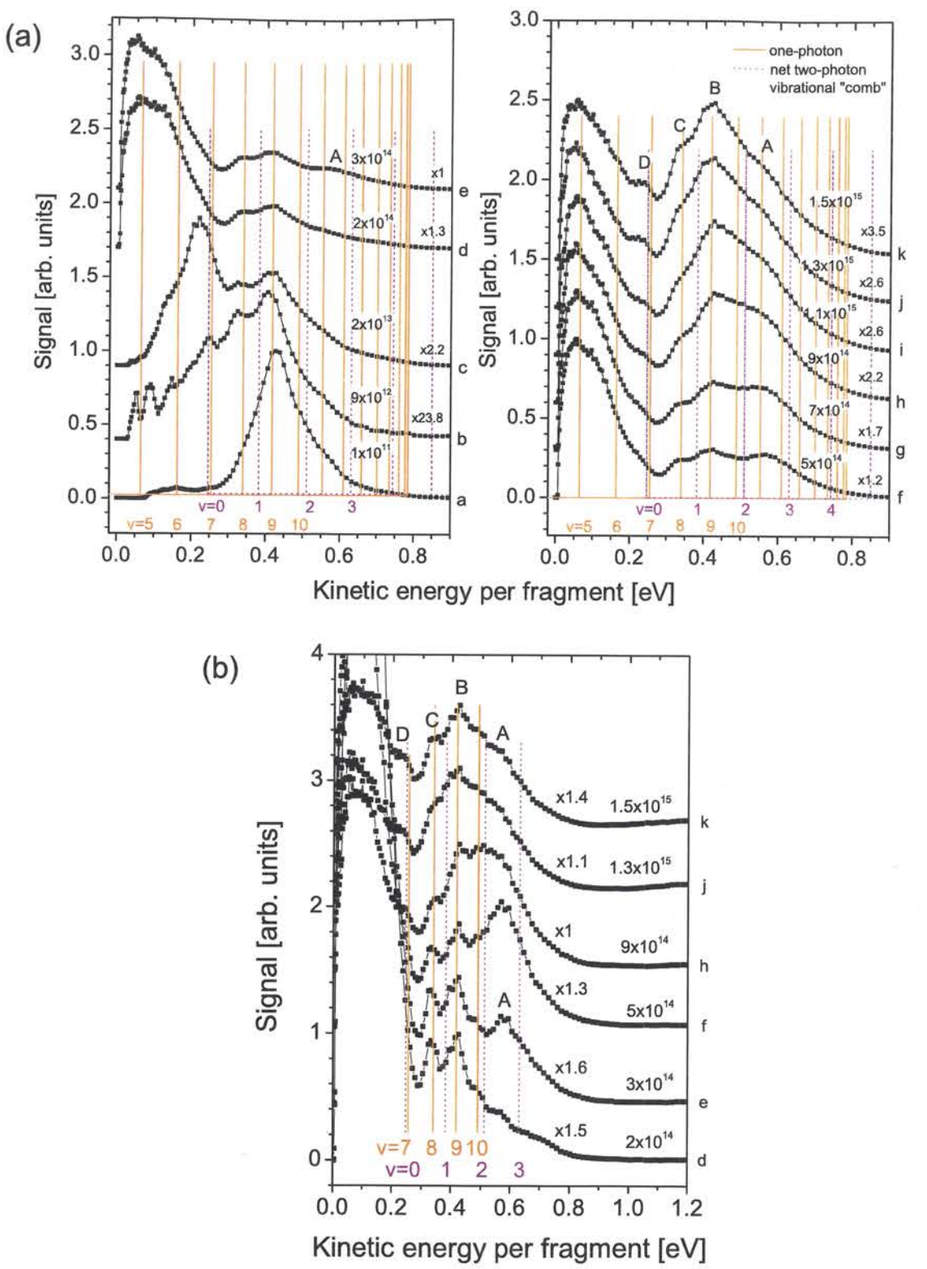


Figure 5.3: Kinetic energy distributions of the fragments obtained by integrating inverted velocity distributions over (a) all angles and (b) 10° around the laser polarization axis. In (b), only the part of the spectra with the net two-photon contribution is shown. The peak laser intensities and the scaling factors are given for each measurement. The measurements are labelled with letters as in Fig. 5.2.

are responsible for this process also decrease, since with increasing intensity, the intensity at which this process occurs gets further away from the peak intensity. The dependence of the total signal of the 1ω bond softening process on the peak intensity is discussed in Section 5.3.

Two-photon bond softening

At an intensity of 3×10^{14} W/cm^2 a new peak emerges at a kinetic energy of about 0.6 eV (measurement e). With increasing intensity it outgrows the peaks from the levels $v = 9$ and $v = 8$ (measurement f). The high intensity and kinetic energies at which this feature appears indicate the 2ω mechanism. A comparison with the 2ω vibrational "comb" suggests that the observed fragments correspond to the vibrational level $v = 3$ [Fig. 5.3(b)]. The apparent level shifting of approximately 50 meV at such a high intensity is reasonable for this level. The narrow angular distributions of the 2ω process, similarly as in the 1ω bond softening process, can be attributed to the shape of the lower potential surface in the region of the avoided crossing.

In the 2ω process, no fragments from the vibrational level $v = 4$ were observed, in contrast to the expectations based on Fig. 2.2. The possible explanation for the absence of the fragments $v = 4$ is that at the intensities at which the 2ω process starts, the process is overshadowed by the 1ω fragments appearing at the same kinetic energies. The 2ω fragments could be observed only at higher intensities at which the 2ω signal exceeds the 1ω signal. At these intensities, however, the lower-lying peak $v = 3$ would be much more pronounced. Apart from that, as observed by Frasinski *et al* [27], it is also possible that the molecules in the level $v = 4$ dissociate by absorbing one photon after being trapped in the light-induced potential well above the three-photon gap (Section 4.3.2).

With further increasing intensity, the 2ω signal becomes comparable to the decreasing 1ω signal. The 2ω fragment kinetic energy distribution broadens to lower kinetic energies, while the contribution of the level $v = 3$ decreases. The humps in Figs. 5.2 and 5.3, indicated by B, C and D, most likely stem from the 1ω contributions of the levels $v = 9$, $v = 8$ and $v = 7$, respectively. At first sight it seems counterintuitive that the modulations are most pronounced at the highest intensity (measurement k). However, as the interaction volume decreases at higher intensities, the volumes of the shells corresponding to the 2ω and 1ω bond softening processes decrease more quickly than the 1ω process occurring in the low-intensity shells. This can be illustrated by the following example based on Eq. (3.32) and the parameters from the experiments. At a peak intensity of 3×10^{14} W/cm^2 (measurement e), the volume around an intensity of 2.7×10^{14} W/cm^2, responsible for the 1ω bond softening fragments, is approximately 5 times larger than the volume around an intensity of 1×10^{13} W/cm^2, which is responsible for the $v = 7$ fragments. At a peak intensity of 1.3×10^{15} W/cm^2 (measurement k) this ratio decreases by about factor of two. The relatively higher 1ω signal at highest intensities provides a possible explanation for a clearer structure at this intensity.

Despite that, the possibility that the humps B, C and D show fragments from the single vibrational levels $v = 2$, $v = 1$ and $v = 0$ cannot be completely excluded. According to the 2ω vibrational "comb", the fragments from these levels can be expected at similar kinetic energies, providing that they are level shifted to lower kinetic energies, as observed in the 1ω bond softening process. According to the spectra, the magnitude of level shifting would be smaller for the lower vibrational levels, as it is expected from the static picture of vibrational levels in the light-induced electronic state. Although the contribution of the single vibration levels in the 2ω signal is not clear, the angular distributions indicate that the lower-energy 2ω fragments can be attributed to the lower vibrational levels (discussed in the following section).

5.2 Angular distributions of the fragments: alignment

5.2.1 Dependence on the peak laser intensity

From the velocity distributions presented in Fig. 5.2, it is clear that the angular distributions of the fragments depend on their kinetic energy as well as on the peak laser intensity. In Fig. 5.4, these dependencies are quantified with the alignment parameter $\langle \cos^2 \theta \rangle$ [Eq. (4.8)] for the angular distributions of the inverted images in Fig. 5.2.

At intensities up to 2×10^{13} W/cm^2, as expected, the lower-lying vibrational levels $v = 8$ and particularly $v = 7$ show higher degrees of alignment. With increasing intensity, the fragments become increasingly more aligned, which indicates dynamic alignment. These results are in agreement with the observations in the D_2^+ measurements, which are discussed in Section 4.3.1.

At a much higher intensity of 1.6×10^{14} W/cm^2, significantly lower alignment parameters were measured at the same kinetic energies. The degradation of the alignment with increasing intensity suggests saturation effects as a cause (Section 4.3.1). For the lower-lying vibrational levels, corresponding to the data at 0.13 eV and 0.23 eV, the degradation extends to peak intensities of 6×10^{14} W/cm^2 or higher. For these levels, namely, higher parallel intensities are needed for dissociation, and thus saturation occurs later in Fig. 5.4. On the other hand, the angular distributions of the levels $v = 8$ and $v = 9$ are not influenced by the intensity variations. For the level $v = 9$, the alignment parameter is 0.74, which is close to that of a $\cos^2 \theta$ distribution.

A rapid increase in alignment with intensity was observed for the fragments at 0.58 eV starting from an intensity of 3×10^{14} W/cm^2. From Figs. 5.2(e) and 5.3(e) it can be seen that the narrowing is due to the appearance of the 2ω peak $v = 3$. The measured angular distribution is a sum of a broad distribution of the fragments $v = 11 - 12$ and a narrower distribution of the fragments $v = 3$. Since the contribution of the 2ω process increases much more rapidly with intensity, the total angular distribution narrows. The rise in alignment is also observed at lower kinetic energies. However, there it occurs at increasingly higher peak intensities, suggesting that these fragments originate from the lower vibrational levels due to the barrier lowering. At sufficiently high intensities, a degradation of alignment is observed for the data at 0.41 and 0.31 eV. This can be attributed to the apparent larger contribution of the 1ω fragments from the levels $v = 9$ and $v = 8$.

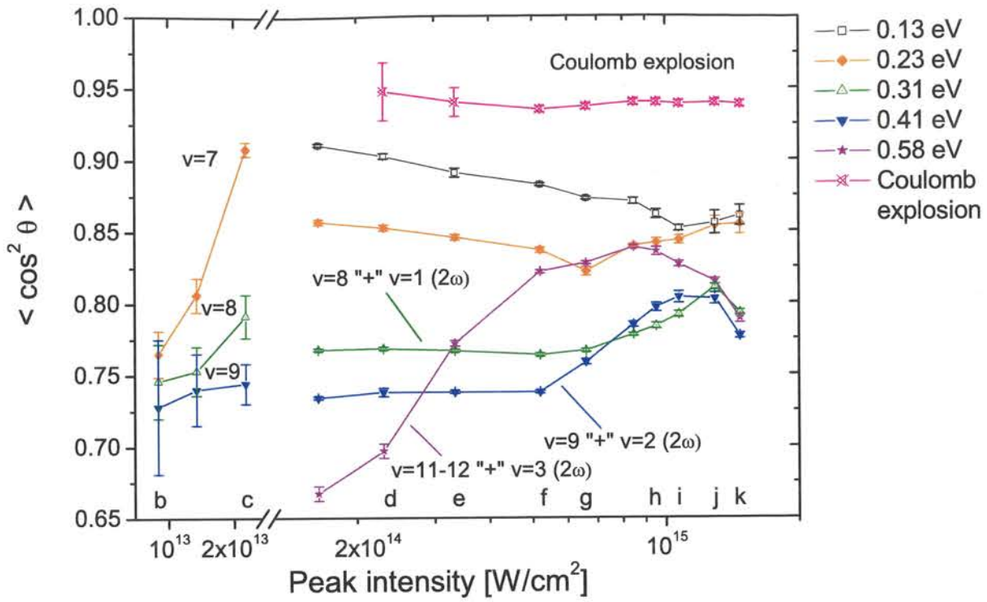


Figure 5.4: The alignment parameter $\langle \cos^2\theta \rangle$ of the angular distributions at different fragment kinetic energies as a function of the peak laser intensity. The data extracted at kinetic energies corresponding to humps A, B and C are labelled with the 1ω and 2ω vibrational levels. The angular distributions were extracted from the inverted images and averaged over five adjacent radii. The error bars indicate the maximum deviation of the $\langle \cos^2\theta \rangle$ parameter for these radii. The measurements at different intensities are labelled with letters as in the previous figures.

For comparison, the alignment parameters of the Coulomb explosion angular distributions are also shown in Fig. 5.4. The Coulomb explosion fragments show the highest degree of alignment at all intensities.

5.2.2 Angular distributions of the one- and net two-photon processes

Figure 5.5 shows angular distributions at different kinetic energies, i.e., corresponding to different vibrational levels. The distributions were extracted from the inverted images in Fig. 5.2 at intensities at which, according to Fig. 5.4, highest degree of alignment for a particular vibrational level was found. For the level $v = 11$, the angular distribution is extracted from the measurement at an intensity of 1.6×10^{14} W/cm^2 in which no contribution of the 2ω process was observed. In distinction to the distributions at lower peak intensities

[Figs. 5.5(a)-(d)], the angular distributions in Figs. 5.5(e)-(g) clearly show contributions of two angular distributions of different widths. These widths can be extracted by fitting the distributions by a sum of two Gaussian distributions. In order to compare these widths with other distributions in Fig. 5.5, the angular distributions corresponding to the 1ω and Coulomb explosion process were also characterized by Gaussian distributions.

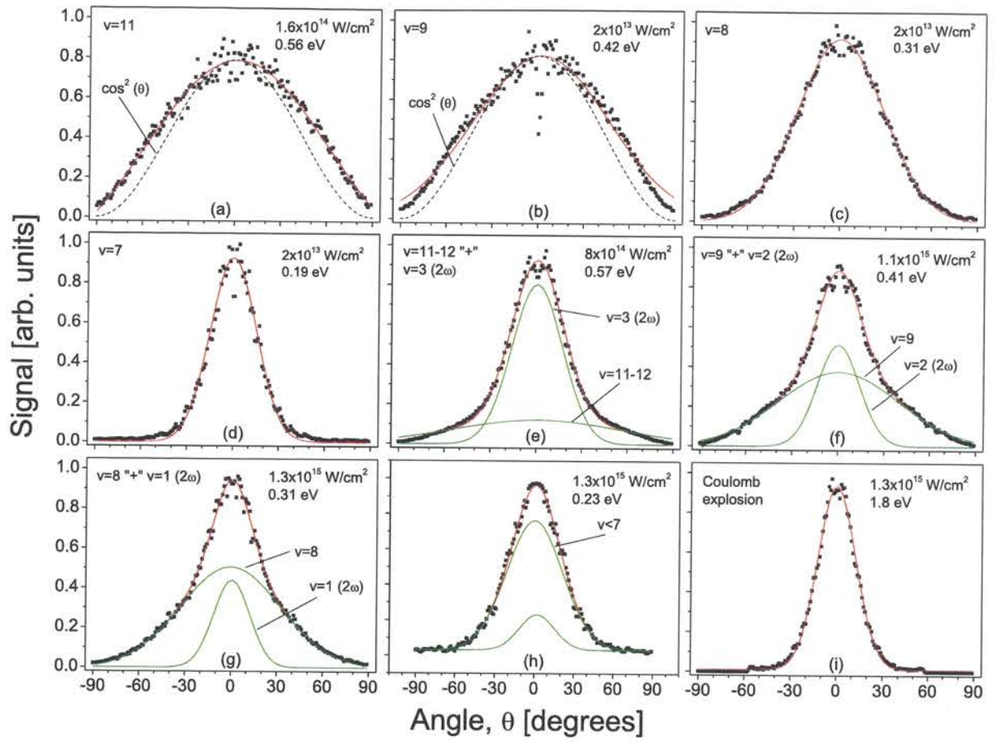


Figure 5.5: Angular distributions of the fragments extracted from the inverted images in Fig. 5.2 at different kinetic energies. For all levels, except for the level $v = 11$, the plots show angular distributions at intensities at which the highest degree of alignment was found (see Fig. 5.4). The plots are labelled with the vibrational levels contributing to the angular distributions. The distributions were fitted to a single Gaussian distribution or to a sum of two Gaussian distributions (see the text). The obtained FWHMs are given in Tables 5.1 and 5.2.

The results of the best fits of the data in Figs. 5.5(a)-(d) are given in Table 5.1. The angular distributions of the fragments $v = 11$ and $v = 9$ are considerably broader than a $\cos^2\theta$ distribution expected for dissociation at low intensities. The broadening can be attributed to saturation, as explained in Section 4.3.1. The vibrational level $v = 8$

Table 5.1: FWHMs of Gaussian distributions fitted to the angular distributions of single vibrational levels as shown in Figs. 5.5(a)-(d).

v	7	8	9	11
	$35.4 \pm 0.3°$	$66.1 \pm 0.3°$	$104 \pm 2°$	$141 \pm 6°$

Table 5.2: FWHMs of Gaussian distributions obtained from the fits shown in Figs. 5.5(e)-(h). The values in the second row (in brackets) are FWHMs treated as fixed parameters corresponding to the angular distributions of the 1ω process at lower intensities.

Kin. energy	0.23 eV	0.31 eV ($v = 1$)	0.41 eV ($v = 2$)	0.57 ($v = 3$)
	$\leq 38°$	$28 \pm 2°$	$33 \pm 2°$	$39 \pm 2°$
	$(50 \pm 2°)$	$(77 \pm 4°)$	$(92 \pm 5°)$	$(130 \pm 30°)$

dissociates via the one-photon bond softening mechanism, which favours photodissociation of better aligned molecules. This is particularly true for the lower-lying vibrational level $v = 7$, which experiences a potential barrier that is hardly penetrable for the larger angles θ (Fig. 2.4). The FWHM found here is close to the width of the corresponding D_2^+ vibrational level $v = 10$ at the same peak intensity (Table 4.2).

For the angular distributions containing 2ω contributions, the widths were determined by fitting the distributions to a sum of two Gaussian distributions, corresponding to the 1ω and 2ω processes. To obtain reliable results, the widths of the one-photon angular distributions were treated as a fixed parameter. Since for the vibrational levels $v = 8 - 11$ no significant variation of the angular distributions were observed at higher intensities (Fig. 5.4), their contribution in Figs. 5.5(e)-(g) can be estimated from the measurements at lower intensities at which no contribution of the 2ω process was observed. The widths of the 1ω distributions estimated in this way are given in Table 5.2, together with the results of the best fits. For the levels $v = 11 - 12$, contributing to the angular distribution in Fig. 5.5(e), the width is determined with a relatively large error (Table 5.2). However, its small contribution to the total angular distribution results in a similar accuracy of the width of the 2ω angular distribution as in other measurements.

For the angular distribution in Fig. 5.5(h), however, the contribution of the hump D at a kinetic energy of 0.23 eV (Fig. 5.3) cannot be easily distinguished from the bond softening fragments $v < 7$. The appearance of this hump at intensities beyond 9×10^{14} W/cm^2 (Fig. 5.3), accompanied with alignment of the total angular distribution at 0.23 eV at the same intensities (Fig. 5.4), suggests that the angular distribution of the emerging hump is narrower than that of the bond softening fragments $v < 7$. From the measurements

at intensities in the range from 3×10^{14} to 7×10^{14} W/cm^2, the FWHM of the angular distribution of the fragments $v < 7$ was estimated to be $50 \pm 2°$. Using this width as a fixed parameter in the fit in Fig. 5.5(h), only the upper limit on the FWHM of 38° of the angular distribution of this hump could be determined (Table 5.2).

The clear narrowing of the angular distributions of the 2ω fragments at lower kinetic energies indicates that they can be attributed to dissociation of the lower-lying levels $v = 2$ and $v = 1$. The barrier lowering mechanism involved here is analogous to the one occurring at the one-photon avoided crossing. However, the angular distributions attributed to the levels $v = 3$ and $v = 9$ are very different, although they both lie in the diabatic curve-crossing region. This is because the level $v = 9$ photodissociates at relatively low intensities, resulting in a broad angular distribution, whereas the dissociation of the level $v = 3$ requires the opening of the three-photon gap, which occurs dominantly along the laser polarization axis. A further difference is that the molecules in the 2ω process undergo an additional adiabatic transfer (X_3 in Fig. 2.2). The potential surfaces at this avoided crossing have a minimum for $\theta = 90°$, which should lead to a broadening of the angular distributions [30]. However, the narrow angular distributions measured in the 2ω process indicate that this effect is much smaller than the narrowing due to the bond softening effect.

5.3 Fragment yields of the one- and the net two-photon process

The dependence of the fragment yield on the peak laser intensity can provide information about the nature of the fragmentation mechanism. The measured total number of the fragments in the 1ω bond softening and the 2ω process as a function of the peak laser intensity is shown in Fig. 5.6. For the bond softening fragments in Fig. 5.6(a), the data were obtained by integrating the inverted velocity distributions over all angles for kinetic energies below 0.3 eV (see Fig. 5.3). The data displayed are normalized to the product of the average ion current and the number of laser shots, which is proportional to the number of fragments for a given interaction volume.

In Fig. 5.6(a), the fragment yield grows rapidly at the lowest intensities. It reaches the maximum at a peak intensity of 3×10^{14} W/cm^2, after which it falls off. For a better understanding of the dependence of the photodissociation probability on the peak intensity, the intensity distribution in the interaction volume needs to be taken into account. Each iso-intensity shell of intensity I and volume $\mathrm{d}V$ contributes to the measured signal with

$$\mathrm{d}S(I) = \alpha P(I)\,\mathrm{d}V\,. \tag{5.1}$$

Here α is a proportionality constant and $P(I)$ is the photodissociation probability, which is assumed to be zero for intensities below the threshold intensity I_{thr}. The total signal is obtained by integrating expression (5.1) over all intensities:

$$S(I_0) = \alpha \int_{I_{thr}}^{I_0} P(I) \frac{\mathrm{d}V}{\mathrm{d}I}\,\mathrm{d}I\,. \tag{5.2}$$

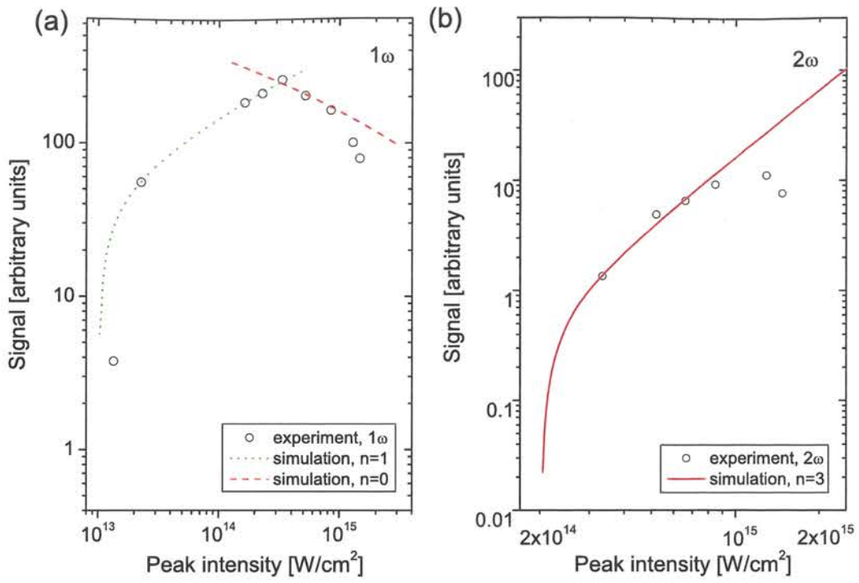


Figure 5.6: The total fragment signal in the (a) one-photon bond softening and (b) net two-photon process as a function of the peak laser intensity. The curves show the results of simulations of a I^n dependence (see the text).

The function $\mathrm{d}V/\mathrm{d}I$ was calculated in Section 3.4 for the intersection of an ion beam of a rectangular cross section with a laser beam of a Gaussian intensity distribution. The probability $P(I)$ is often characterized by a I^n dependence, where n can be related to the number of photons participating in the process. In the calculation of the distribution $\mathrm{d}V/\mathrm{d}I$, the experimental ion beam dimensions of $l = 250$ μm and $h = 50$ μm were used. The diameter of the laser beam was calculated for the range of peak intensities presented in Fig. 5.6 using Eq. (3.22) together with the experimentally measured pulse energy of 1.92 mJ and pulse duration of 96 fs (the same in all measurements). From Fig. 5.3, the threshold intensity I_{thr} for the bond softening process was determined to be 1×10^{13} W/cm^2.

The fit to the data at lower intensities in Fig. 5.6(a) yielded the best agreement with $n = 1$, as expected for a one-photon process. The decrease of the signal at higher intensities is consistent with the observed broadening of the angular distributions (Fig. 5.4). Namely, both the effects suggest that the 1ω process enters the saturation regime, in which the photodissociation probability is equal to unity and the measured signal is determined by the size of the interaction volume only. Using the same model, the data in this regime were simulated by the dissociation probability independent of intensity, i.e., $n = 0$. Here a good agreement was achieved for the measurements below 8.5×10^{14} W/cm^2. However, at higher intensities, the number of fragments decreases more rapidly than the focal volume

($n = 0$ curve), indicating that the 1ω process is additionally depleted through ionization into the Coulomb explosion channel.

The major advantage of the velocity imaging method is that it allows to disentangle the contributions of fragments through their angular distributions. Utilizing this property, the signal of the 2ω process was extracted from the inverted velocity images. Here the 2ω process was treated as a whole since the kinetic energy distributions do not allow to determine the contributions of single vibrational levels. Therefore, the angular distributions in the kinetic energy range from 0.3 to 0.8 eV were summed and the total angular distribution was fitted by a sum of two Gaussian distributions, as described in Sec 5.2. The area under the Gaussian distribution corresponding to the 2ω process served as a measure of the signal of this process. The data obtained in this way are plotted in Fig. 5.6(b) as a function of the peak laser intensity.

The best comparison of the results with the model was achieved with a I^3 dependence. The obtained result reflects the initial three-photon absorption process. The effect of the subsequent one-photon re-emission seems to be much smaller, which can be attributed to saturation of the one-photon process at these intensities. A larger discrepancy between the data and the I^3 dependence is found at highest intensities. The smaller slope indicates that the 2ω process enters the saturation regime. Besides that, at such high intensities a significant fraction of the dissociating molecular ions ends up in the Coulomb explosion channel.

In a recent experiment starting from neutral H_2, Gibson *et al* [109] also found an I^3 power law dependence of the 2ω process. On the contrary, in the only related ion beam experiment, Williams *et al* [43] have observed a linear $n = 1$ dependence, which they attributed to the specific nature of H_2^+. The results presented here cast doubt on the validity of these speculations.

Chapter 6

Coulomb explosion

This chapter presents a study of the Coulomb explosion (CE) process aimed at finding evidence of the existence of critical distances in the ionization of H_2^+. The predicted maxima in the ionization rate at particular internuclear separations should be reflected in the kinetic energies of the CE fragments (Section 2.2.2). To meet the requirements for higher energy resolution, stronger signal and smaller intensity variations in the interaction region, the following changes in the setup were made:

- Ion beam collimation was improved by using apertures A4 and A7 with widths along the laser polarization axis of 200 μm and 25 μm, respectively. The narrower second slit also decreased the spatial variations of the laser intensity in the interaction region, as discussed in Section 3.4. At the same time the current of the molecular ions was increased (Section 3.1.4).

- As explained in Section 5.1, the size of the fragment velocity distribution on the MCP detector was enlarged by extending the distance between the interaction region and the detector. In order to detect energetically higher CE fragments, the center of the velocity distribution was shifted to the edge of the detector by slightly inclining the axis of the ion beam.

- The magnification of the CCD camera was increased so that one pixel corresponded to a size of 55 μm on the detector (instead of 107 μm as in the previous chapters). The higher magnification allowed the CE channel and only part of the dissociation channel to be imaged (see Fig. 6.1).

Section 6.1 deals with measurements using pulses with a duration below 100 fs. First, projected velocity distributions of the CE fragments at different intensities are shown and discussed. Results at near-threshold intensities in H_2^+ and D_2^+ are then presented. The peaks observed in the kinetic energy spectra are interpreted in a subsequent model. Next, an experiment with elliptically polarized light is described, which was conducted to eliminate a possible alternative explanation for the measured spectra. In Section 6.2, the CE process was investigated using pulses of longer durations, revealing separate groups in

the fragment velocity distributions. The results of the measurement of the fragment yield of the CE channel as a function of the peak laser intensity are discussed in Section 6.3.

6.1 Measurements with sub-100-fs pulses

Figure 6.1 shows the projected velocity distributions of the H_2^+ fragments at intensities in the range of $9.3 \times 10^{13} - 3.4 \times 10^{14}$ W/cm^2 and pulse lengths of 95–100 fs. The measured images were normalized to the product of the average ion current and the number of laser shots. The colours were selected to present the CE signal, while the stronger dissociation signal extends beyond the displayed range. The CE protons become observable at an intensity of about 9×10^{13} W/cm^2 as a narrow group around 1.5 eV. At lowest intensities the signal rises rapidly with increasing intensity. As discussed in Section 3.4, this is characteristic of processes occurring near the threshold intensity I_{thr} for a particular process. The images at intensities in the range from 1.1×10^{14} to 1.6×10^{14} W/cm^2 reveal two groups centered around 1.1 eV and 1.7 eV. With increasing intensity the groups merge together into a broad group, which shifts to higher kinetic energies.

6.1.1 Mechanism of Coulomb explosion

The fragment kinetic energies observed in this and previous experiments suggest that CE occurs at relatively large internuclear separations. A molecular ion can reach these distances via 1ω or 2ω process, as illustrated in Fig. 6.2. As explained in Section 2.2.3, in the range of internuclear distances of 5–12 a.u., the ionization probability is strongly enhanced. The positively charged nuclei created after ionization repel each other. The fragments gain a kinetic energy of e^2/R, where R is the internuclear separation at the moment of ionization. The measured kinetic energy per fragment is the sum of the initial kinetic energy due to the dissociation process [Eq. (4.2)] and the gained CE energy

$$E_{kin} = E_{diss}(v) + \frac{e^2}{2R}. \tag{6.1}$$

For a relatively large distance R, the kinetic energy of a dissociating molecule can be approximated by the final dissociation energy E_{diss}. For example, for the measured total kinetic energy of $E_{kin} = 2$ eV and a dissociation energy of $E_{diss} = 0.2$ eV (found from the dissociation channel), the CE energy is 1.8 eV. This energy corresponds to an ionization at $R \sim 7.5$ a.u., at which the $1s\sigma_g$ and $2p\sigma_u$ curves reach approximately the value they have in the dissociation limit.

The dependence of the average energy of the CE protons on the peak laser intensity is shown in Figure 6.3. The data were derived from the measurements displayed in Fig. 5.2 in the previous chapter, since there the fragments with higher kinetic energies than here could be imaged. The average measured kinetic energy increases from 1.5 eV to above 2.2 eV in the range of intensities used. At the same time, the average dissociation energy is increased only by 0.1 eV (i.e., from 0.14 eV to 0.24 eV). Therefore, it is the

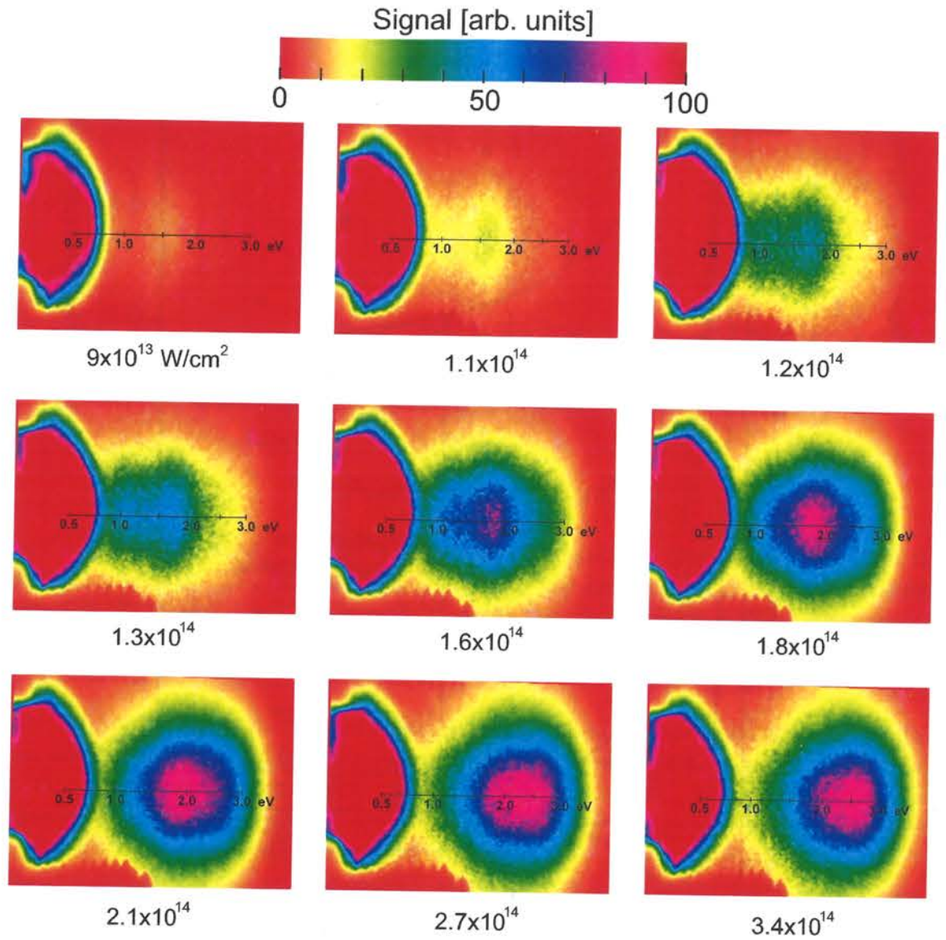


Figure 6.1: Projected 2D velocity distributions of the Coulomb explosion fragments of H_2^+ at different intensities and pulse durations between 95–100 fs. The colours were selected to show the signal in the CE channel. The fragments with kinetic energies below 0.8 eV (showed in saturation) stem from the photodissociation channel. Two CE groups centered around 1.1 and 1.7 eV were observed at intensities in the range of $1.1 \times 10^{14} - 1.6 \times 10^{14}$ W/cm^2.

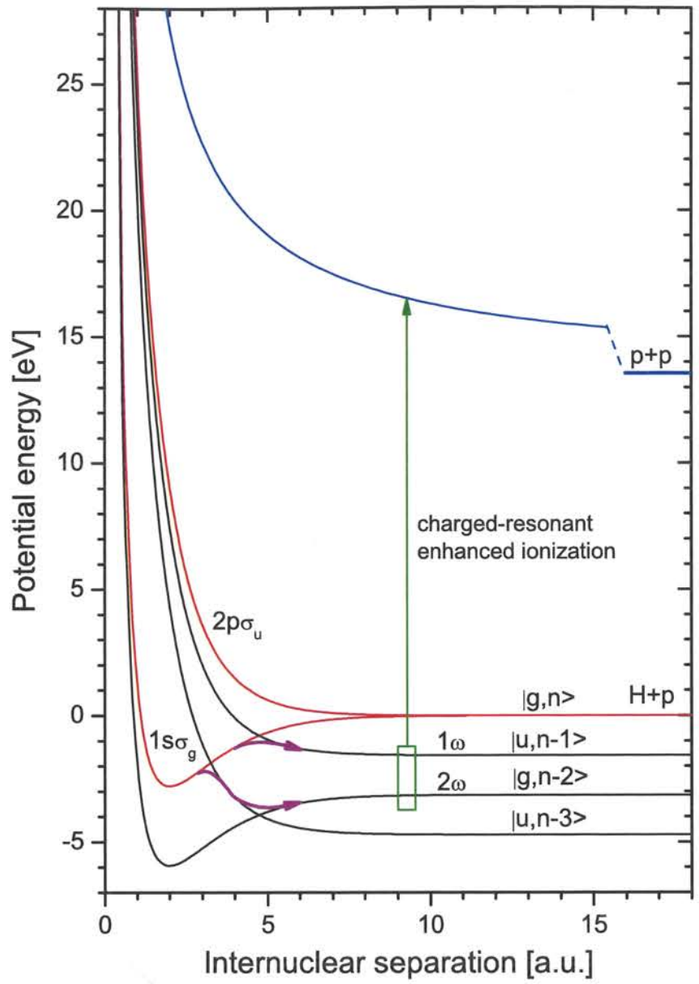


Figure 6.2: Potential energy diagram illustrating the mechanism of Coulomb explosion. The molecules dissociate by following the one- (1ω) or net two-photon (2ω) process. At relatively large internuclear separations, a dissociating molecular ion undergoes ionization and subsequent Coulomb explosion of nuclei. The measured kinetic energy per fragment is thus the sum of the initial dissociation energy and the CE energy.

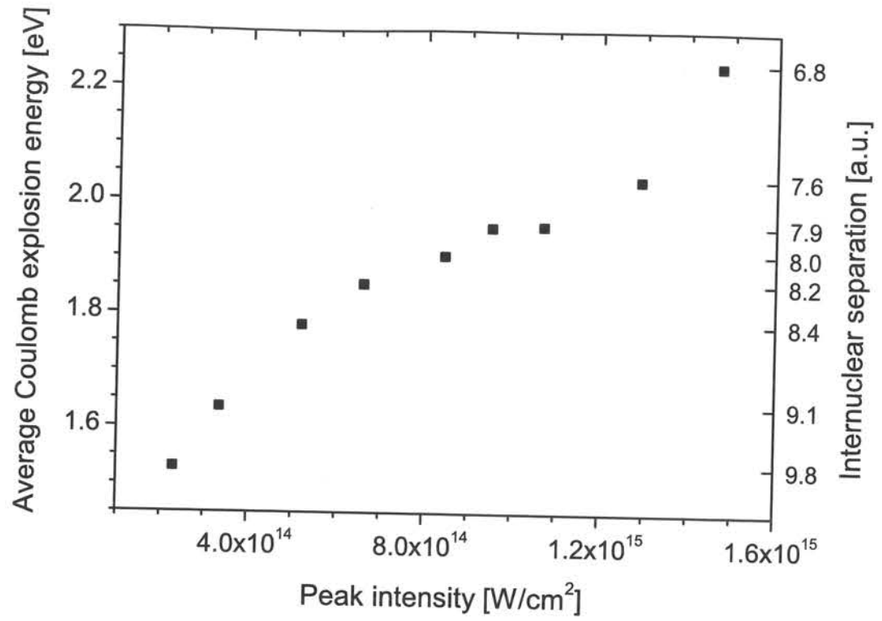


Figure 6.3: Average kinetic energy of the Coulomb explosion protons as a function of the peak laser intensity. The data were derived from the kinetic energy spectra obtained by integrating the inverted velocity distributions in Fig. 5.2 over all angles. The axis on the right side marks the corresponding internuclear separations at which the ionization occurs.

ionization occurring at shorter internuclear separations, rather than the change in the initial kinetic energy, that is responsible for the higher fragment energies. The reason is that with increasing peak intensity, the threshold intensity I_{thr} is reached earlier, i.e., at smaller internuclear separations. However, this effect is somewhat diminished since I_{thr} also increases with decreasing R.

In the interpretation of the images, the spatial intensity distribution must also be considered. At intensities near the threshold, the measured signal comes from a narrow intensity range between the threshold intensity and the peak intensity, as illustrated in Fig. 6.4. At higher peak intensities, the spectra also include contributions measured at lower peak intensities, thus broadening the kinetic energy distributions. At highest intensities in Fig. 6.3, a more rapid increase of the average kinetic energy was observed. Roughly speaking, the new intensity shells created in the center of the intensity distribution are responsible for the higher kinetic energies. This can be visualized if the spectra measured at successive intensities are subtracted from each other, as shown in Fig. 6.5. Obviously, the intensity range from 1.3×10^{15} to 1.5×10^{15} W/cm^2 is responsible for a narrower distribution centered around 2.6 eV, corresponding to an ionization at $R \sim 6$ a.u.

The two groups observed in Fig. 6.1 suggest that ionization occurs at two different

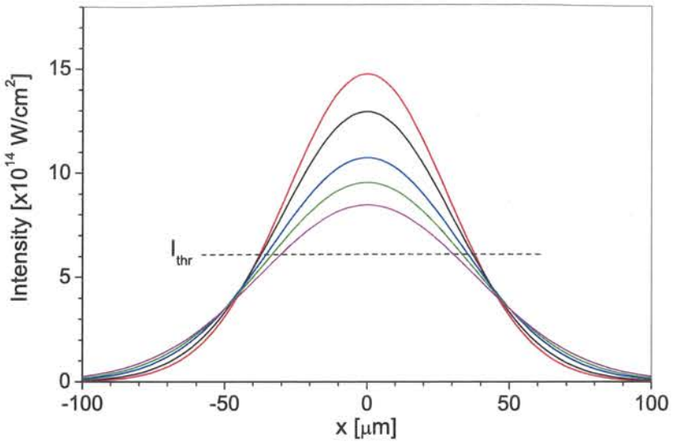


Figure 6.4: Gaussian distributions illustrating one-dimensional spatial intensity distribution for the measurements at highest intensities in Fig. 6.3. The areas under the distributions are the same, corresponding to the same pulse energy, whereas their widths are smaller for higher peak intensities. Only intensities above the threshold intensity I_{thr} for a particular process contribute to the measured signal.

internuclear separations. An alternative explanation could be that the groups originate from different initial kinetic energies of molecules following the 1ω and 2ω dissociation paths. However, the difference between the average kinetic energies of the fragments in these processes of less than 0.5 eV is smaller than the one in the two CE groups (see Fig. 5.3). Furthermore, since in the dissociation channel the 1ω process is much stronger than the 2ω process at intensities below 2×10^{14} W/cm^2, basically only one group, rather than observed two groups, would be seen in the CE channel.

Angular distributions of the fragments

The alignment of the CE fragments as a function of the laser peak intensity was already presented in Chapter 5 together with the data from the dissociation channel (see Fig. 5.4). With the alignment parameter $\langle \cos^2 \theta \rangle \sim 0.94$, the CE fragments are at all intensities significantly more aligned than the fragments in the dissociation channel. A typical angular distribution of the CE fragments was shown in Fig. 5.5(i). The data were fitted by a Gaussian distribution with a FWHM of 29°. Angular distributions of similar widths were found in the experiments starting with H_2 [29].

Since the CE fragments result from ionization of dissociating molecules, both the alignment due to the dissociation process and the angular dependence of the ionization probability will contribute to their angular distributions. A major reason for a higher degree of alignment of the CE fragments is a strong angular dependence of the ionization probability (geometric alignment). Posthumus *et al* have shown that the threshold intensity

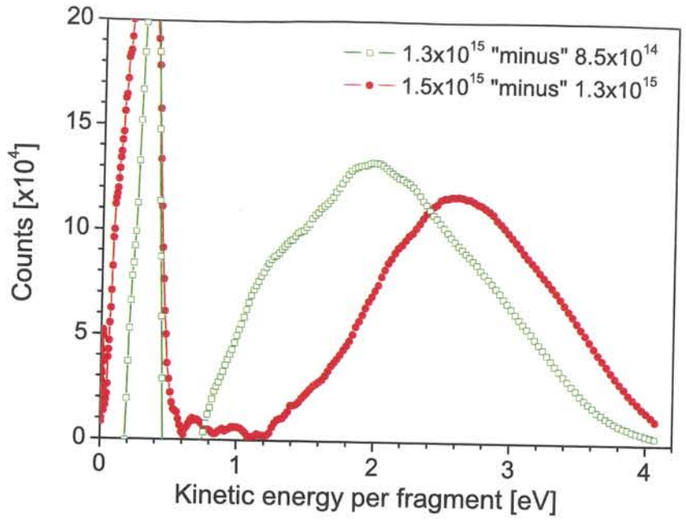


Figure 6.5: Kinetic energy distributions obtained by subtracting the spectra at successive intensities, as indicated in the legend. The spectra used here were obtained by integrating experimental data in Fig. 4.9 over all angles.

I_{thr} for ionization of diatomic molecules is smallest for $\theta = 0°$ and sharply increases with θ [29] (here θ is the angle between the laser polarization and the molecular axis). This angular dependence is strongest at the classical critical internuclear distance of about 10 a.u. In a recent experiment, Litvinyuk *et al* have found that the ionization probability of N_2 molecules aligned parallel to the electric field is about 4 times greater than for those aligned perpendicular to the field [110].

In the two CE groups different degrees of alignment were observed. The FWHM of the group at 1.1 eV is 33° (fit by a Gaussian), whereas the group centered at 1.7 eV has the FWHM of 29°. This behaviour can be explained in the following way. Only molecules sufficiently aligned with the laser field can be ionized, i.e., those for which $I_{thr}(\theta) < I_0$, where I_0 is the peak intensity. At shorter internuclear separations $I_{thr}(\theta)$ is generally higher, and thus ionization will be possible only for molecules at smaller angles around $\theta = 0°$. Since the higher energy group at 1.1 eV stems from an ionization at shorter internuclear separations, its angular distribution will be narrower, as observed in the experiment.

6.1.2 Coulomb explosion at near-threshold intensities

As discussed earlier, at laser peak intensities close to the threshold intensity, only a very narrow interval of intensities contributes to the measured signal. The most interesting results could be therefore expected at the lowest intensities at which the counting rates are still sufficiently high to allow measurements. Despite that fact, the CE of H_2^+ and D_2^+

has not been investigated in this intensity range. The related experiments on neutral H_2 or D_2 molecules were limited to relatively high intensities required for their ionization.

Kinetic energy spectra

Figure 6.6 shows the kinetic energy distributions along the laser polarization axis for intensities in the range of 7.7×10^{13} to 2.5×10^{14} W/cm^2. Sharp peaks were observed at lowest intensities of $\sim 8 \times 10^{13}$ W/cm^2 [Fig. 6.6(a)]. The main peaks appeared at the same or slightly larger kinetic energies also in measurements at higher intensities. Above an intensity of 1×10^{14} W/cm^2 the structure begins to vanish and only modulations in the spectra were observed. The second group, observed in Fig. 6.1 at 1.1 eV, becomes visible at intensities above 1.2×10^{14} W/cm^2 [Fig. 6.6(b)]. Above an intensity of 2×10^{14} W/cm^2, the two groups are seen as one broader group, which shifts to higher kinetic energies with increasing intensity.

In order to ensure a sufficient number of the fragments at lowest intensities, the data were collected for about 6 hours, corresponding to approximately 1×10^7 laser shots. The spectra at these intensities contain 10^3–10^4 fragments. The images were usually recorded in intervals of about 30 minutes, between which the energy and duration of the pulses were checked, and optimization of the ion current was made. The single images were discarded in case of a larger deviation of one of these parameters. A very good check of the stability of the intensity and the overlap of the laser and ion beams during single measurements was found to be the ratio of the number of the fragments in the CE and the dissociation channel. Particularly at lowest intensities this number is highly sensitive on the peak laser intensity and thus could be used as a relative measure of the peak intensity. For the spectra in Fig. 6.6(a) in the intensity range of $7.7 \times 10^{13} - 9.4 \times 10^{13}$ W/cm^2, the ratio of the maximum signals in the dissociation and CE channel ranges from 120 down to 30.

Figure 6.7 shows an example of a low-intensity experimental image (peak intensity of 8.8×10^{13} W/cm^2), whose spectra is displayed in Fig. 6.6(a). No clear structure could be perceived here. Due to the low signal, the peaks become recognizable only after integration over a sufficient number of pixels. For the integration over 2°, as used in the kinetic energy spectra, this number is between 17 and 23 in the kinetic energy interval 1–2 eV. A similar structure as in Fig. 6.6(a) was found also for the fragments ejected along an angle with respect to the symmetry axis, as shown in Fig. 6.8. However, the signal-to-noise ratio is here lower because of the lower number of fragments and the uncertainty related to the exact position of the symmetry axis in the images.

The peaks were confirmed in numerous measurements under different experimental conditions. In the early experiments, in which the whole area of the phosphor screen was imaged ("pixel size" of 107 μm), the peaks were not completely resolved. After increasing the imaging magnification ("pixel size" of 48 μm), a uniform rectangular pattern stemming from the mesh mounted on the MCP detector became visible. It should be noted that the separation between the mesh wires of 224 μm (4–5 pixels) was much smaller than the peak separation and thus it was not related to the observed features. With the higher magnification factor and without the mesh, the spectra could be better resolved. Since

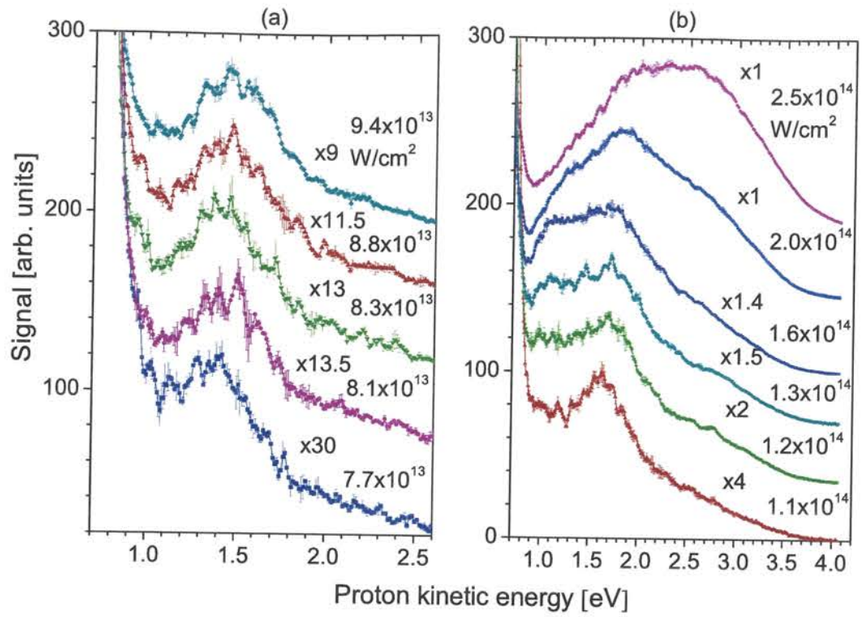


Figure 6.6: Kinetic energy spectra of the Coulomb explosion channel of H_2^+ at different intensities and a pulse duration of 95–100 fs. Sharp peaks were observed at intensities close to the threshold. The two groups at 1.1 and 1.7 eV observed in Fig. 6.1 can be resolved here at intensities in the range of 1.2×10^{14} to 2×10^{14} W/cm^2. The spectra were obtained by integrating the projected 2D velocity distributions over 2° around the laser polarization axis. The error bars were calculated from the difference in the spectra of the velocity distributions above and below the symmetry axis. The peak laser intensities and scaling factors are given for each measurement.

no influence of the electric field from the MCP on the fast fragments was observed, the measurements afterwards were done without the mesh. The peak structure was also observed when different areas of the MCP detector and different orientations of the CCD camera were used, eliminating any possibility that the structure is related to a property of the imaging system. The possibility that the structure is caused by the ion beam itself was ruled out by an additional check in which the signal was recorded with the laser beam being blocked.

Interpretation of the peaks in the kinetic energy spectra

According to the CREI model, the critical distances depend only on the electromagnetic interactions and thus should be the same in H_2^+ and D_2^+ [36, 111]. To check whether the observed peaks can be attributed to different critical distances, CE was studied in D_2^+

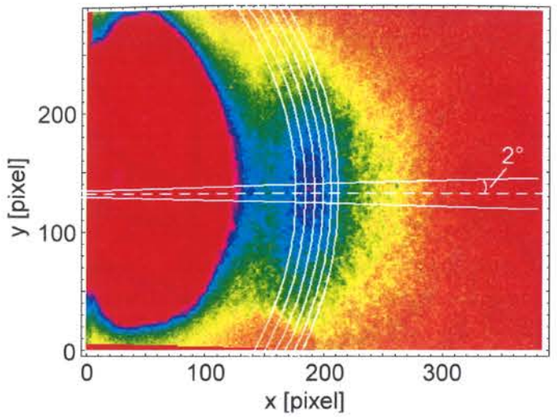


Figure 6.7: Projected 2D velocity distribution of the protons in the Coulomb explosion channel of H_2^+ at an intensity of 8.8×10^{13} W/cm^2. The integration range for the spectra in Fig. 6.6 is indicated by the lines at an angle of 2° with the symmetry axis. The circular arcs mark the position of the main peaks between the kinetic energies of 1.3 and 1.6 eV in Fig. 6.6(a).

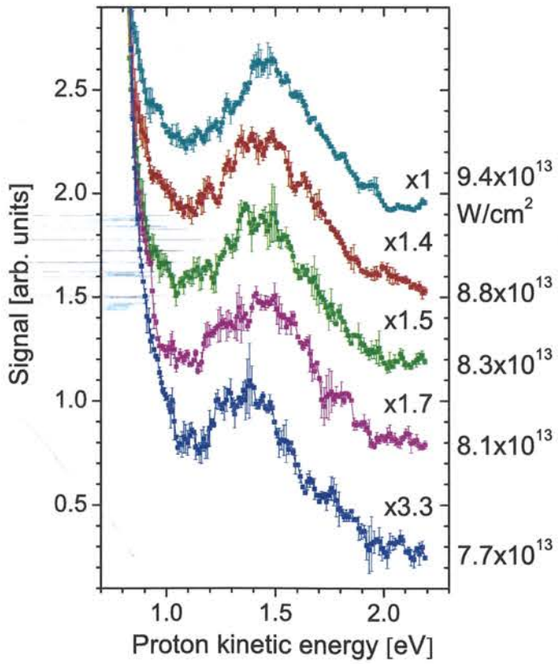


Figure 6.8: Kinetic energy spectra as in Fig. 6.6(a), but with the integration performed over angles in the range of 2–4° both above and below the symmetry axis.

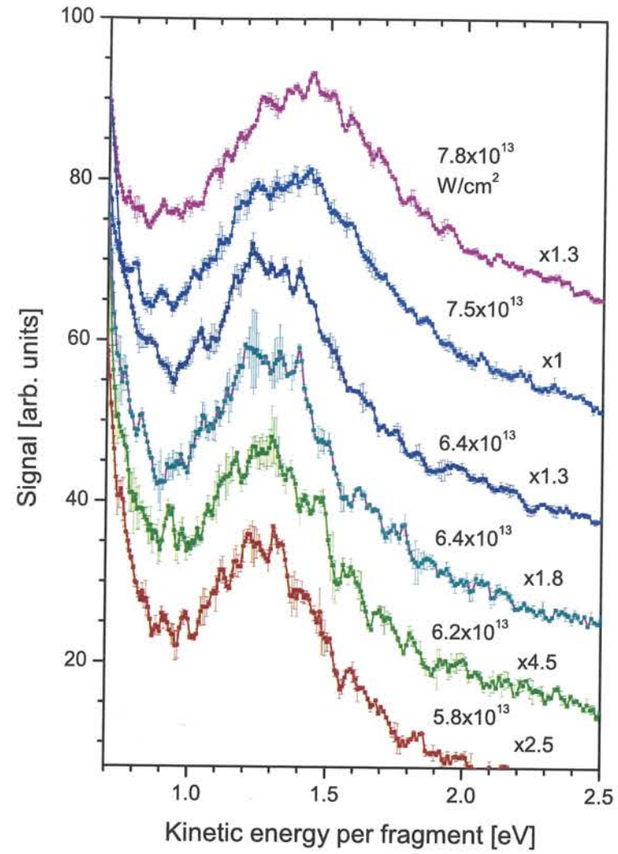


Figure 6.9: Kinetic energy spectra of deuterons in the Coulomb explosion channel of D_2^+. The spectra were obtained by integrating the projected 2D velocity distributions over 2° around the laser polarization axis. The pulse length was approximately 100 fs. The peak laser intensities and the scaling factors are given for each measurement.

under similar conditions. At intensities close to the threshold, a peak structure was also observed here, however with a smaller peak separation than in H_2^+, as shown in Fig. 6.9. The small separation between adjacent peaks observed in D_2^+ was close to the limit of the experimental resolution, resulting in a less clear structure. Nevertheless, the obvious differences in the spectra of H_2^+ and D_2^+ strongly suggest that the individual peaks are not due to ionization at different critical distances.

The magnitude of the spacing between the peaks of H_2^+ and D_2^+ indicates that the peaks could be related to the vibrational levels, similarly as observed in the dissociation channel (Chapters 4 and 5,[28],[86]). In Fig. 6.10, the energies of the peaks were compared with the one-photon vibrational "comb". The "comb" was shifted here by an energy amount as a free parameter. The results of such a fit show that the energies of the main peaks in the different spectra of Fig. 6.6(a) could be matched well.

According to Eq. (6.1), the energy shift of the "comb" is equal to the CE energy $E_{CE} = e^2/(2R_c)$ gained after ionization at a critical distance R_c. Since in the fit this energy was the same for all peaks, the model suggests that the molecules in different vibrational states all undergo ionization at a same critical distance. The "combs" in Figs. 6.10(a) and 6.10(b) were shifted by a CE energy of 1.06 eV, which corresponds to $R_c \sim 12.8$ a.u. A slightly larger shift in Fig. 6.10(c) of 1.09 eV corresponds to $R_c \sim 12.5$ a.u. The ionization at somewhat shorter critical distance can be explained by the higher peak intensity in this measurement. In Fig. 6.11, the spectra of D_2^+ were compared with its vibrational "comb" in the same way. The best agreement was achieved in Fig. 6.11(a), where all main peaks are matched by the "comb". The energy shift of the "comb" in the case of D_2^+ was 0.98–1.01 eV, corresponding to $R_c \sim 13.5$–13.9 a.u.

The fact that the vibrational structure remains preserved after ionization suggests that the observed critical distance is well defined. The maximum spread ΔR_c can be estimated by allowing the maximum CE energy spread, ΔE_{CE}, to be equal to the distance between the adjacent peaks. Taking $\Delta E_{CE} = 0.1$ eV and $E_{CE} = 1$ eV, the relative spread $\Delta R_c/R_c = \Delta E_{CE}/E_{CE} \sim 0.1$.

Due to similar spacings between the adjacent vibrational levels, the position of the "comb" and the vibrational levels assigned to the peaks above are not unambiguously determined. The vibrational levels assigned in Figs. 6.10 and 6.11 may differ by ± 1 in H_2^+ and ± 2 in D_2^+, respectively. This also implies an uncertainty related to the value of the critical distances given above.

The presented CE spectra do not simply reflect the spectra of the photodissociation fragments. Particularly, the effect of level shifting observed in the photodissociation channel for the levels $v \leq 7$ in H_2^+ seems not to be present in the CE spectra. For a complete understanding of the results, quantum mechanical calculations including both the dissociation and ionization dynamics are required.

A structure in the CE kinetic energy spectra of H_2^+ was observed only in an early experiment of Zavriyev *et al* [64] starting from neutral H_2. In contrast to the work presented in this thesis, the modulations in [64] were reported in a broader kinetic energy range of about 1–3 eV and at much higher intensities of $\sim 10^{15}$ W/cm^2. The results were associated to vibrational population trapping in a light-induced potential well. In contrast to the

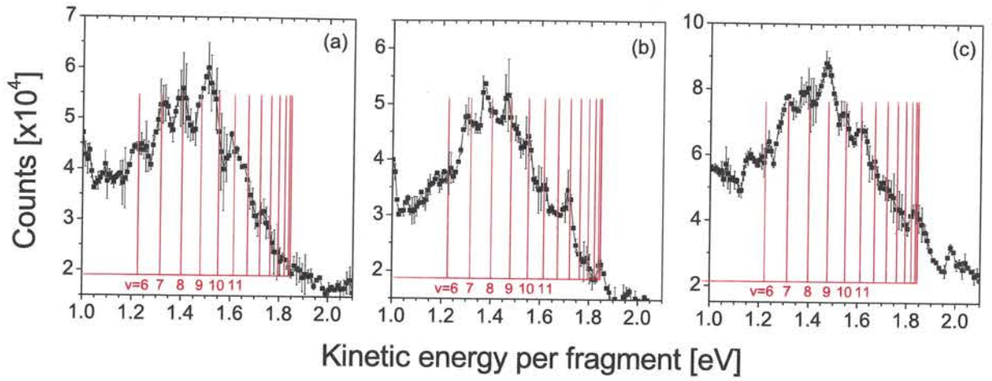


Figure 6.10: Comparison of the spectra of H_2^+ from Fig. 6.6(a) with the one-photon vibrational "comb". The peak intensities are (a) 8.1×10^{13}, (b) 8.3×10^{13} and (c) 8.8×10^{13} W/cm^2. The "combs" in (a) and (b) were shifted by 1.06 eV and in (c) by 1.09 eV from its dissociation position. These Coulomb explosion energies correspond to ionization at a well-defined critical distance of $R_c \sim 12.8$ a.u. and $R_c \sim 12.5$ a.u., respectively.

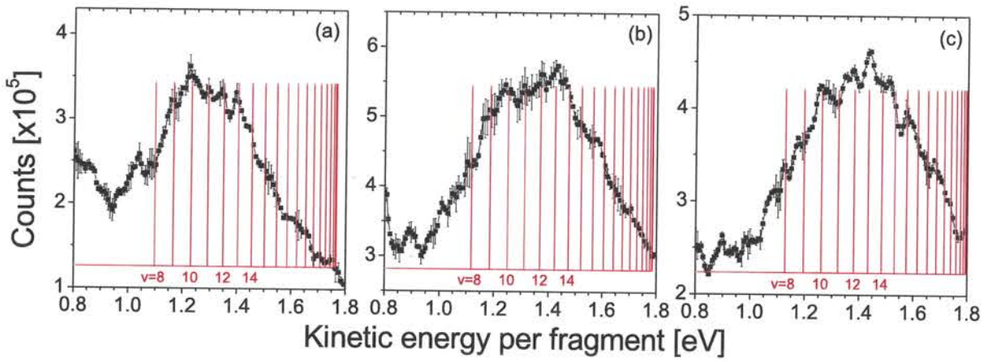


Figure 6.11: Comparison of the spectra of D_2^+ from Fig. 6.9 with the one-photon vibrational "comb". The peak intensities are (a) 6.4×10^{13}, (b) 7.5×10^{13} and (c) 7.8×10^{13} W/cm^2. The "combs" were shifted by (a) 0.98 eV, (b) 1.0 eV and (c) 1.01 eV from its dissociation position, corresponding to ionization at critical distances of $R_c \sim 13.5$–13.9 a.u.

mechanism of enhanced ionization, later confirmed to be responsible for CE [112], the authors proposed that the trapped molecules undergo multiphoton ionization at the different turning points, giving rise to fragments of different kinetic energies. This interpretation suffered from several difficulties, one of which is that the population trapping is very unlikely to occur at such high intensities. In the succeeding experiments, no structure in the CE spectra could be observed.

Measurements with elliptically polarized light

An alternative interpretation of the structure observed in the CE spectra could be provided by the role of the ionized electron. From the processes of above-threshold ionization and high harmonic generation, it is known that the ionized electron can return to the ionic core, following the change of the direction of the laser electric field [37]. One can imagine that the electron could screen the positive charge of a nucleus during the time spent in its vicinity, thereby weakening the Coulomb repulsion of the fragments. The kinetic energies of such fragments would be shifted to lower values, resulting in maxima at lower and minima at higher energies than expected. The process could be repeated in the next optical cycles, producing modulations in the spectra.

The return of the electron to a nucleus can be hindered if a small ellipticity is introduced to the laser field. The elliptically polarized field can generally be written as

$$E(t) = E_0 \left[\boldsymbol{e}_x \, \varepsilon \cos(\omega t) + \boldsymbol{e}_z \sin(\omega t) \right] , \tag{6.2}$$

where ε is a parameter characterizing the ellipticity of the electric field. The ellipticity was introduced to the laser beam by a combination of a zero-order half-wave and a zero-order quarter-wave plate[1]. First, the optical axis of the $\lambda/2$ plate was set to produce vertically polarized light. This was done by passing the beam through a properly adjusted Glan polarizer and measuring the power of the reflected beam. After that, the $\lambda/4$ plate was placed behind the $\lambda/2$ plate and, by maximizing the vertically polarized component, the optical axis of the quarter-wave plate was set parallel to the optical axis of the $\lambda/2$ plate. An ellipticity was then introduced by rotating the optical axis of the $\lambda/2$ plate by a small angle. The parameter ε was calculated by measuring the power of the vertically and horizontally polarized components, P_z and P_x, respectively:

$$\varepsilon = \sqrt{\frac{P_x}{P_z}} . \tag{6.3}$$

Figure 6.12 shows kinetic energy spectrum of the CE protons measured at $\varepsilon = 0.29$. A structure similar to those observed with linearly polarized light can be perceived. For the relatively high elipticity used, the return of the electron is not possible, and hence its impact on the CE spectra can be excluded. It should be noted that the spectrum measured here is distorted, since the laser polarization was not strictly vertical, as required by the imaging method employed.

[1] Halle

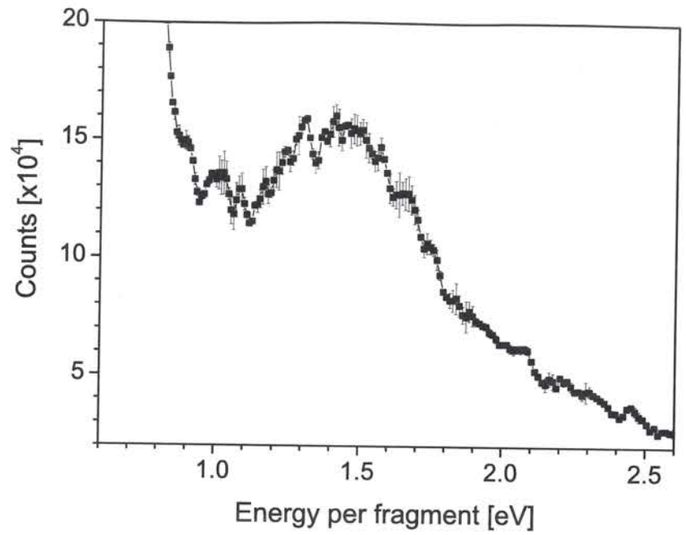


Figure 6.12: Coulomb explosion spectra of H_2^+ with an elliptically polarized light of the ellipticity parameter $\varepsilon = 0.29$. The peak intensity was 9.4×10^{13} W/cm^2 and the pulse duration was 101 fs.

6.2 Measurements with pulses of longer durations

The Coulomb explosion of H_2^+ and D_2^+ was also investigated by using longer pulses with durations of 90–630 fs, varied by introducing a chirp to the pulse. Figure 6.13 shows in comparison the measured velocity distributions of H_2^+ and D_2^+. The pulse energy and the beam diameter were the same in all measurements. The corresponding peak intensities range from 4×10^{14} down to 5×10^{13} W/cm^2.

The fragments with highest kinetic energies, both in H_2^+ and D_2^+, were observed with shortest pulses (pulse duration of 90 fs). In this case, high intensities are reached shortly after the start of the dissociation process, and hence CE occurs at smaller internuclear separations, resulting in higher repulsion energies. With longer pulses, fragments of lower kinetic energies were observed, corresponding to ionization at larger internuclear separations. With increasing pulse duration, fewer molecules will be ionized at an early stage of the pulse (i.e., at short internuclear separations) and more will undergo ionization at later times (i.e., at larger internuclear separations) when intensity is higher. Thus, the average kinetic energy of the fragments shifts to lower values. Simultaneously, the number of CE fragments falls off as a consequence of the decrease in the peak laser intensity.

It is interesting to note that the kinetic energies of the deuterons are larger in all pairs of measurements. Since D_2^+ is heavier, its fragments in the dissociation process acquire a lower velocity $\sqrt{2E_{diss}/m}$, where m is the fragment mass. Thus, for the same evolution of the pulse, the ionization of D_2^+ will take place at smaller internuclear separations, resulting

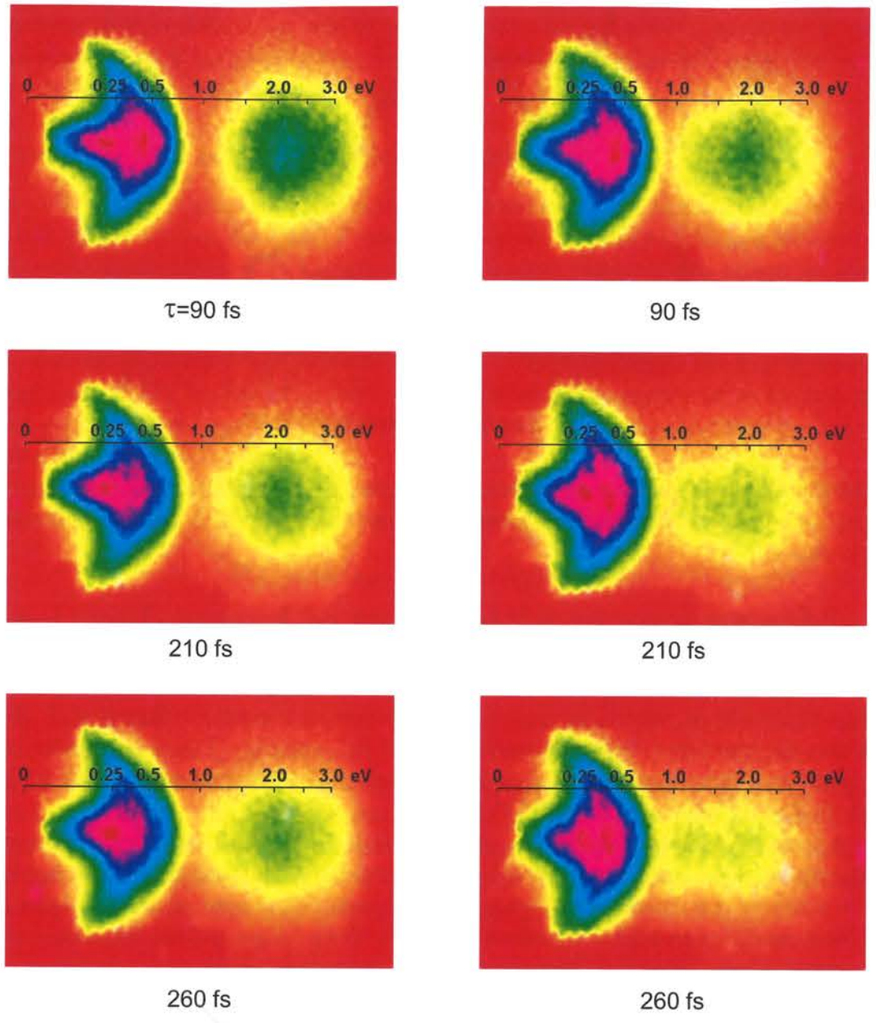


Figure 6.13: Projected 2D velocity distributions from photodissociation and Coulomb explosion of D_2^+ (left) and H_2^+ (right) for different pulse durations (τ). The pulse energy of 1.7 mJ was the same in all measurements. The peak intensities range from 4×10^{14} down to 5×10^{13} W/cm^2.

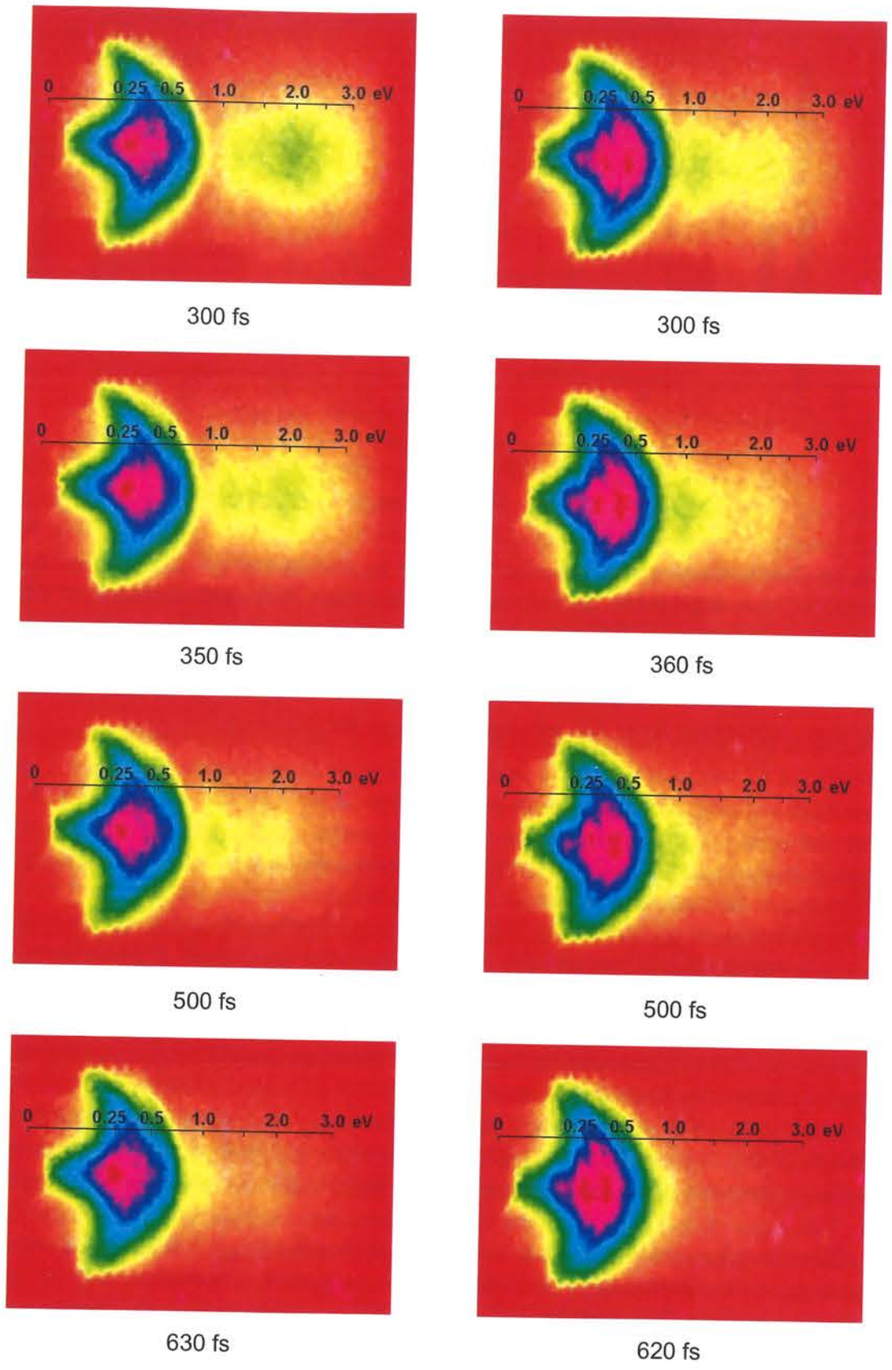


Figure 6.13 (continued): Projected 2D velocity distributions from photodissociation and Coulomb explosion of D_2^+ (left) and H_2^+ (right) for the different pulse durations.

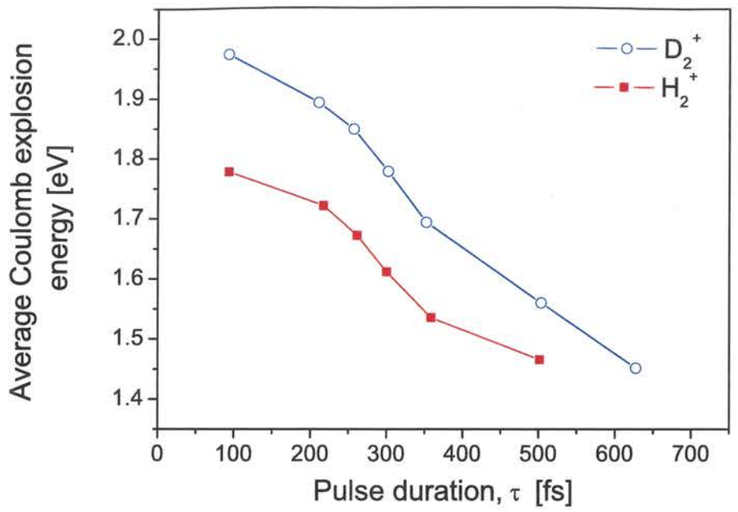


Figure 6.14: Dependence of the average Coulomb explosion energy on the pulse duration for H_2^+ and D_2^+ (see Fig. 6.13). In the intermediate range of the pulse durations, the ratio of the durations for D_2^+ and H_2^+ at the same average kinetic energies is approximately 1.4. This is in agreement with the value expected from the ratio of the masses of the molecular ions. In the derivation of the average Coulomb explosion energies, the average dissociation energies were subtracted from the measured average kinetic energies.

in higher kinetic energies. By comparing the images of D_2^+ and H_2^+ in Fig. 6.13 it can be seen that the molecular ions display the same features, which, however, in D_2^+ appear at larger pulse durations. This suggests that the observed features have their origin in the critical distances, as these are the same for H_2^+ and D_2^+.

Figure 6.14 shows the dependence of the average CE energies calculated from Fig. 6.13 on the pulse duration. Indeed, the ratio of the pulse durations at which the average CE energy is the same in both molecular ions is approximately 1.4 for intermediate pulse durations, which is in agreement with the inverse ratio of their velocities. For shorter pulses the discrepancy is larger, whereas for large pulse durations the CE fragments overlap with the fragments from the dissociation channel.

The most interesting observation was made for pulse durations of 350–500 fs in D_2^+ and ~300 fs in H_2^+. In these measurements, three main CE groups are clearly seen. The kinetic energy spectrum of the CE deuterons at a pulse duration of 350 fs is shown in Fig. 6.15(a). The same signal as a function of the internuclear separation is displayed in Fig. 6.15(b). The transformation was made using Eq. (6.1) and $\langle E_{diss} \rangle = 0.31$ eV, as calculated from the data in the dissociation channel. The main groups centered at 1.2, 1.5 and 2.1 eV correspond to critical distances of 15, 11 and 8 a.u., respectively. The two smallest of them are close to the critical distances of 7 and 10 a.u. predicted by the CREI model [36].

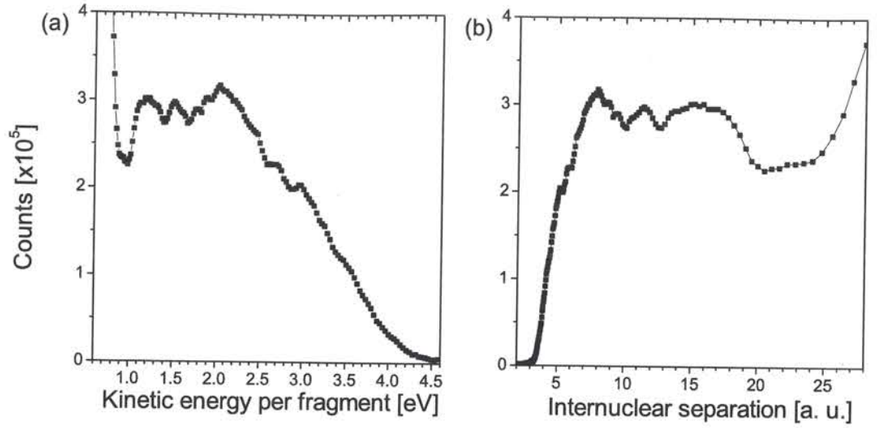


Figure 6.15: (a) Kinetic energy distribution of the Coulomb explosion fragments of D_2^+ at a pulse duration of 350 fs and a peak intensity of 9.8×10^{13} W/cm^2. The spectrum was obtained by integrating the projected velocity distribution over 2° around the laser polarization axis. (b) The same data as a function of the internuclear separations at which Coulomb explosion occurs. The main peaks in Fig. 6.15(a) correspond to critical distances of 8, 11 and 15 a.u. The transformation was made using Eq. (6.1) and $\langle E_{diss} \rangle = 0.31$ eV, as calculated from the data in the dissociation channel.

The groups observed in Fig. 6.13 have significantly different widths of angular distributions. Figure 6.16 shows the angular distributions at kinetic energies of 1.2 and 3.0 eV, as extracted from the measurement with a pulse duration of 350 fs. The higher-energy fragments, corresponding to ionization at smaller internuclear separations, also have here narrower angular distributions. As explained in Section 6.1.1, the different angular distributions support the idea of critical distances. In this case, however, the range of FWHM of angular distributions from 28–37° is much larger and seems to be correlated with the clearer separation of the groups corresponding to different critical distances.

In a recent pump-probe experiment, Trump *et al* investigated the dissociation dynamics in D_2^+ [113]. The dissociation was initiated by a pump pulse and the dissociating molecules were ionized by a time-delayed second pulse. The authors observed a shift of the CE group to lower kinetic energies with the increased delay, confirming that ionization occurs at larger internuclear separations. This experiment thus showed that ionization can take place at different internuclear separations. However, it did not provide an evidence for the existence of critical internuclear distances, as suggested by the measurements presented here.

The enhancement of ionization at larger internuclear separations with increasing pulse duration was also observed in measurements in which the peak intensity was approximately the same. Figure 6.17 shows the results of the measurements with pulse durations in the range of 225–730 fs and a peak intensity around 1×10^{14} W/cm^2. The effect of the

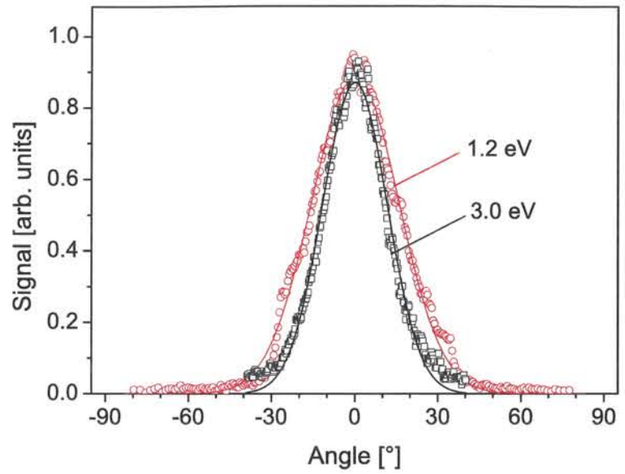


Figure 6.16: Angular distributions of the Coulomb explosion groups of D_2^+ at kinetic energies of 1.2 and 3.0 eV. The data were extracted from the measurement with a pulse duration of 350 fs and a peak intensity of 9.8×10^{13} W/cm^2 (see Fig. 6.13). The solid lines are fits by Gaussian distributions with FWHMs of 37° at 1.2 eV and 28° at 3.0 eV.

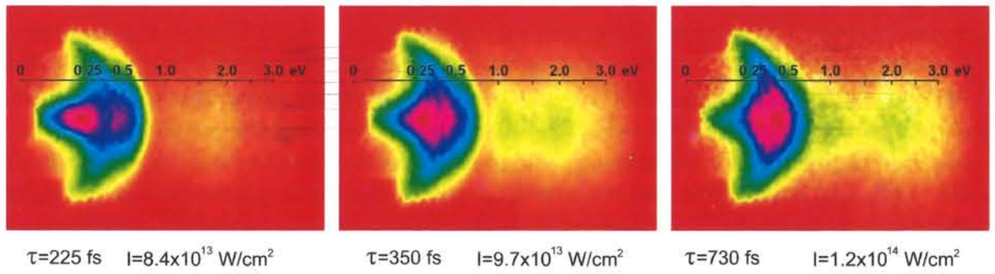


Figure 6.17: Projected 2D velocity distributions of the Coulomb explosion fragments of D_2^+ at different pulse durations (τ) and similar peak intensities (I).

longer pulse lengths on the peak intensities was compensated with smaller laser beam diameters in the interaction region. The action of longer pulses on molecules is clearly seen on fragments in the dissociation channel. At the shortest pulse duration, the most of the molecules dissociate via the high-intensity 1ω and 2ω bond softening mechanisms. With increasing pulse duration more molecules dissociate already at lower intensities on the rising edge of the pulse. By the time the peak of the pulse is reached, only a small portion of the molecules will remain undissociated, and consequently the bond softening peaks disappear. On the other hand, CE is favoured by the long "time-window" in which intensity is high. In this case, the large number of molecules arriving at different times can undergo ionization in a broader range of internuclear separations. The increased duration of the laser field will enable ionization at larger internuclear separations, resulting in the CE fragments with lower kinetic energies.

6.3 Fragment yield of the Coulomb explosion channel

The dependence of the total number of counts in the CE channel on the peak laser intensity is displayed in Fig. 6.18. At intensities below 2×10^{14} W/cm^2, the CE signal exhibits a steep rise with peak intensity. By taking into account the volume expansion and the intensity dependence of the process (Section 5.3), it was found that the data can be described well by a I^3 power dependence. Since the ionization potential is much larger than the photon energy, the magnitude of n found here is not related to the number of photons absorbed. For example, at $R = 8$ a.u., ionization potential is $I_p \sim 17$ eV [Eq. (2.19)], which corresponds to an energy of about 11 photons of $\lambda = 790$ nm. This is also expected from the predictions based on the value of the Keldysh parameter, which states that ionization should take place in the tunnelling regime (Section 2.2.1).

The fact that the same parameter n is found in the CE and the dissociation process [see Fig. 5.6(b)] suggests that the ionization process follows the dissociation and is possibly limited by it. At higher peak intensities, the yield of the CE process, similarly as the yield in the 2ω dissociation process, shows a larger deviation from an I^3 power law. However, the comparison with the model for $n = 0$ suggests that the process has not saturated. Like the results of the dissociation channel (Section 5.3), the dependence found here is also in agreement with the recent findings in H_2 by Gibson *et al* [109] and contrary to the results of the ion beam experiment by Williams *et al* [43].

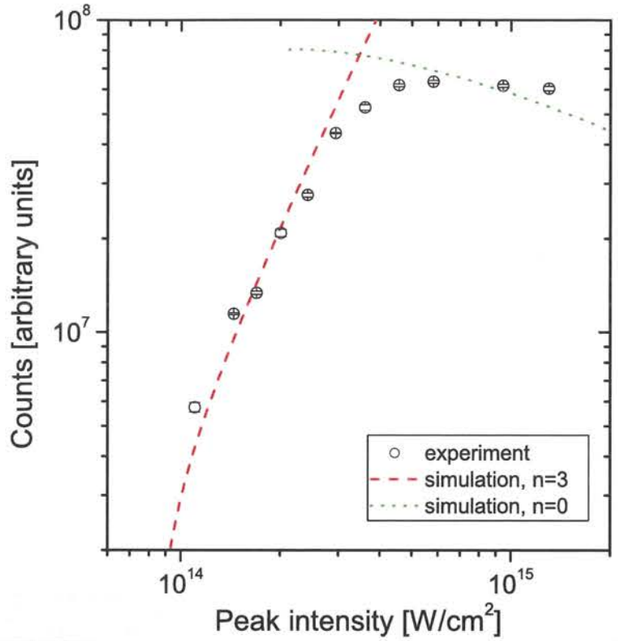


Figure 6.18: Yield of the Coulomb explosion fragments of H_2^+ as a function of the peak laser intensity. The error bars were calculated from the standard deviation of data recorded in 2–3 measurements, each with $\sim 4 \times 10^5$ laser shots. The pulse duration was 95 fs. The curves are results of the simulation of a I^n dependency, as described in Section 5.3.

Chapter 7

Conclusion and perspectives

Photodissociation of D_2^+ and photodissociation and Coulomb explosion of H_2^+ at intensities $\geq 10^{14}$ W/cm^2 have been investigated for the first time with high resolution. To date, experiments on H_2^+ and D_2^+ in intense laser fields have been conducted almost exclusively on neutral molecules as targets. The additional ionization process involved not only complicated interpretation of the results, but also hindered investigation of intense-field phenomena at lower intensities. Here, fast and collimated beams of H_2^+ and D_2^+ molecular ions have been used in combination with a photofragment imaging method. The setup provided comparatively small intensity variations in the interaction region and high-resolution imaging of the three-dimensional velocity distribution of the photofragments.

To elucidate the role of isotope effects in the photodissociation process, D_2^+ has been studied under experimental conditions similar to those in the H_2^+ study of Sändig *et al* [28] (Chapter 4). Fragments from the single vibrational levels have been resolved in the velocity distributions. Their kinetic energy and angular distributions can be interpreted with the model of light-induced potentials. In comparison with the kinetic energy spectra of H_2^+ in [28], here smaller widths of the peaks have been found, suggesting that the measured widths reflect the lifetimes of the vibrational states in the perturbed ground electronic state. Moreover, fragments with near-zero kinetic energies and broad angular distributions have been observed. They indicate the mechanism of trapping, for which there has hitherto been little experimental evidence.

In net two-photon photodissociation of H_2^+ (Chapter 5), the single vibrational level $v = 3$ has been identified. With increasing peak intensity, fragments with lower kinetic energies and narrower angular distributions have been observed, which suggests the potential barrier-lowering mechanism for the initial three-photon absorption.

The measured velocity distributions of the fragments in the one- and net two-photon photodissociation processes of D_2^+ and H_2^+, as well as those of HD^+ presented in [46, 114], provide the basis for theoretical calculations. Simulations based on the three-dimensional time-dependent Schrödinger equation, including full nuclear motion and intensity distribution in the interaction region, as done by Serov *et al* [45], will lead to a better understanding of the photodissociation dynamics of molecules in intense fields.

The main objective of this thesis was to explore the Coulomb explosion channel of

H_2^+. The most interesting aspect of this phenomenon is the prediction that ionization is enhanced at particular critical internuclear distances [34–36]. Up to now, however, such distances have not been experimentally observed.

The major contribution of this work consists in presenting the evidence of the existence of critical internuclear distances of enhanced ionization (Chapter 6). For the first time, a clear structure has been found in kinetic energy distributions of Coulomb explosion protons. The peaks observed at intensities close to the threshold have been attributed to H_2^+ molecules in different vibrational states, ionized at a well-defined critical distance of about 13 a.u. Furthermore, additional Coulomb explosion velocity-groups have been observed at higher intensities and particularly with pulses of longer durations. Their different kinetic energies and angular distributions strongly suggest ionization at three critical distances.

The Coulomb explosion data provide a benchmark for theoretical calculations, which are necessary for a complete understanding of the results. As suggested by the observed structure, present calculation methods should be extended to incorporate both the dissociation and ionization dynamics. In future experiments, it would be interesting to use molecules prepared in certain vibrational states to unambiguously assign the Coulomb explosion peaks to vibrational quanta. A significant technical improvement leading to clearer spectra would be to use lasers with higher repetition rates, as well as to simultaneously detect the fragments from single molecular ions [115].

This work demonstrates that using H_2^+ in ion beams offers exciting possibilities for fundamental explorations. As a one-electron system, H_2^+ is an ideal system for Coulomb explosion imaging [116, 117]. By ionizing the molecular ion with few-cycle pulses, the vibrational wave function is instantaneously projected onto the Coulomb potential curve. The initial wave function can be reconstructed from the proton kinetic energy distribution. In this way, not only can the molecular structure be directly imaged, but also the temporal evolution of this structure can be followed by employing the pump-probe technique.

Another interesting topic for future research is investigation of the photoelectron ATI spectra of H_2^+. These spectra are produced at critical internuclear distances and recently they were theoretically calculated [118]. Moreover, the electron momenta can be imaged in coincidence with the momenta of nuclear fragments [119]. Such a kinematically complete experiment, like the one recently carried out on H_2 [120], would provide a better understanding of the interplay between nuclear and electronic dynamics for different fragmentation channels of H_2^+. Furthermore, it would be interesting to investigate diffraction of the electrons from the two nuclei. According to simulations [121], the electron velocity distribution should exhibit an interference pattern, from which information about the critical internuclear distances could be inferred. Like Coulomb explosion imaging, this method could open up the possibility of dynamic imaging of the H_2^+ nuclear wave function.

Appendix A

Unit conversion

quantity	value	
1 eV	1.6022×10^{-19} J	8065.73 cm^{-1}
1 atomic mass unit (amu)	1.6605×10^{-27} kg	
1 a.u. of length	0.5292×10^{-10} m	
1 a.u. of energy	27.2114 eV	
1 a.u. of charge	1.6022×10^{-19} C	
1 a.u. of electric field	5.1422×10^{11} V/m	
1 a.u. of electric dipole moment	8.4783×10^{-30} Cm	

Appendix B

Molecular data on H_2^+ and D_2^+

B.1 Constants (from Huber and Herzberg [108])

quantity	symbol	value		unit
		H_2^+	D_2^+	
reduced mass	m	0.5038	1.0069	amu[a]
equilibrium internuclear separation	R_{eq}	1.988	1.995	a.u.
vibrational constants	ω_e	2321.7	1577.3	cm^{-1}
	$\omega_e x_e$	66.2		cm^{-1}
rotational constants	B_e	30.2	15.02	cm^{-1}
	α_e	1.68	0.56	cm^{-1}

[a] 1 atomic mass unit (amu) = 1.6605×10^{-27} kg

Energies of vibrational levels:

$$E(v) = \omega_e \left(v + \frac{1}{2}\right) - \omega_e x_e \left(v + \frac{1}{2}\right)^2 + ... \tag{B.1}$$

Energies of rotational levels:

$$\begin{aligned} F(J) &= B_v J(J+1) - ... \\ B_v &= B_e - \alpha_e(v + 1/2) + ... \end{aligned} \tag{B.2}$$

B.2 Energies and populations of vibrational levels

The energies of the vibrational levels of H_2^+ (Table B.1) and D_2^+ (Table B.2) were calculated by Cohen *et al* [122] and Dunn [123], respectively. The eigenvalues were obtained by

numerically solving the radial Schrödinger equation for the ground electronic state and the rotational quantum number $J = 0$. The given values are relative to the energy of the dissociation limit.

Tables B.1 and B.2 also give the relative populations of vibrational levels as calculated by von Busch and Dunn [89]. The authors used an electron bombardment-type ion source. They modified the Franck-Condon principle to obtain quantitative agreement between theory and experiment. The calculated vibrational population is slightly different from that given by the Franck-Condon factors between the vibrational level $v = 0$ of H_2 and the vibrational levels of H_2^+.

Table B.1: Eigenenergies and relative populations of vibrational states of H_2^+.

vibrational level	energy [eV][a]	population[b]
0	-2.646	0.119
1	-2.375	0.190
2	-2.119	0.188
3	-1.878	0.152
4	-1.652	0.111
5	-1.441	0.077
6	-1.244	0.053
7	-1.060	0.036
8	-0.891	0.024
9	-0.735	0.016
10	-0.593	0.011
11	-0.465	0.008
12	-0.351	0.005
13	-0.252	0.004
14	-0.168	0.003
15	-0.100	0.002
16	-0.049	0.001

[a] Eigenvalues calculated by Cohen *et al* [122], Table II.

[b] Populations calculated by von Busch and Dunn [89], Table II(C).

Table B.2: Eigenenergies and relative populations of vibrational states of D_2^+.

vibrational level	energy [eV][a]	population[b]
0	-2.687	0.045
1	-2.491	0.104
2	-2.304	0.141
3	-2.124	0.148
4	-1.952	0.134
5	-1.788	0.111
6	-1.630	0.086
7	-1.480	0.065
8	-1.337	0.047
9	-1.201	0.034
10	-1.072	0.024
11	-0.950	0.017
12	-0.835	0.012
13	-0.727	0.009
14	-0.625	0.006
15	-0.530	0.005
16	-0.444	0.003
17	-0.363	0.003
18	-0.290	0.002
19	-0.225	0.001
20	-0.167	0.001

[a] Eigenvalues calculated by Dunn [123], Table III.

[b] Populations calculated by von Busch and Dunn [89], Table II(C).

List of symbols and acronyms

γ	Keldysh parameter
ε	ellipticity of the laser field
ε_0	electric permittivity of free space
θ	angle between the molecular internuclear and the laser polarization axis
λ	wavelength of the laser field
ν	frequency of the laser field
τ	pulse duration
ω	angular frequency of the laser field
ω_R	Rabi frequency
1ω	one-photon dissociation
2ω	net two-photon dissociation
2D	two-dimensional
3D	three-dimensional
ATI	above-threshold ionization
ATD	above-threshold dissociation
B	magnetic field
c	speed of light in vacuum
CCD	charge-coupled device
CE	Coulomb explosion
CPA	chirped pulse amplification
CREI	charge-resonant enhanced ionization
d	diameter of the laser beam (FWHM)
$\boldsymbol{d}$	transition dipole moment
e	electron charge
E	energy
$\boldsymbol{E}$	electric field
E_0	amplitude of the electric field
E_{CE}	Coulomb explosion energy
E_{diss}	dissociation energy

E_{kin}	kinetic energy
E_p	pulse energy
f	focal length
FWHM	full width at half maximum
h	Planck's constant, aperture width along the laser polarization axis
$\hbar$	reduced Planck's constant ($h/2\pi$)
I	intensity, peak intensity
I_0	peak intensity
I_f	peak intensity at the focus
I_i	intensity of an iso-intensity shell
I_p	ionization potential
I_{thr}	threshold intensity
J	rotational quantum number
l	aperture width along the laser propagation axis
L	distance between the interaction region and the MCP detector
m	mass
m_e	electron mass
m_m	molecular mass
MCP	multichannel plate
n	number of photons, exponent in I^n
q	ion charge
r	radial coordinate, curvature radius of the sector magnet
R	internuclear separation
R_c	critical internuclear distance
R_{eq}	equilibrium internuclear separation
t	time between the moment of interaction and detection
U_a	acceleration voltage
U_p	ponderomotive potential
v	vibrational quantum number
v_0	velocity of ions in the ion beam
V	interaction volume, potential
w	laser beam radius ($1/e^2$ half-width)
w_0	laser beam radius in the focal plane (waist, $1/e^2$ half-width)
x	spatial coordinate along the ion beam axis
y	spatial coordinate along the laser propagation axis
y_R	Rayleigh range
z	spatial coordinate along the laser polarization axis

Bibliography

[1] A. H. Zewail. Femtochemistry: Atomic-scale dynamics of the chemical bond. *J. Phys. Chem. A*, 104(24):5660–5694, 2000.

[2] T. Brabec and F. Krausz. Intense few-cycle laser fields: Frontiers of nonlinear optics. *Rev. Mod. Phys.*, 72(2):545–591, 2000.

[3] C. J. Joachain, M. Dörr, and N. Kylstra. High intensity laser-atom physics. *Adv. At. Mol. Opt. Phy.*, 42:225–286, 2000.

[4] N. A. Papadogiannis, B. Witzel, C. Kalpouzos, and D. Charalambidis. Observation of attosecond light localization in higher order harmonic generation. *Phys. Rev. Lett.*, 83(21):4289–4292, 1999.

[5] P. M. Paul, E. S. Toma, P. Breger, G. Mullot, F. Auge, P. Balcou, H. G. Muller, and P. Agostini. Observation of a train of attosecond pulses from high harmonic generation. *Science*, 292(5522):1689–1692, 2001.

[6] M. Hentschel, R. Kienberger, C. Spielmann, G. A. Reider, N. Milosevic, T. Brabec, P. Corkum, U. Heinzmann, M. Drescher, and F. Krausz. Attosecond metrology. *Nature*, 414(6863):509–513, 2001.

[7] M. Drescher, M. Hentschel, R. Kienberger, M. Uiberacker, V. Yakovlev, A. Scrinizi, T. Westerwalbesloh, U. Kleineberg, U. Heinzmann, and F. Krausz. Time-resolved atomic inner-shell spectroscopy. *Nature*, 419(6909):803–807, 2002.

[8] A. Scrinzi, M. Geissler, and T. Brabec. Attosecond cross correlation technique. *Phys. Rev. Lett.*, 86(3):412–415, 2001.

[9] J. Itatani, F. Quéré, G. L. Yudin, M. Y. Ivanov, F. Krausz, and P. B. Corkum. Attosecond streak camera. *Phys. Rev. Lett.*, 88(17), 2002.

[10] S. A. Aseyev, Y. Ni, L. J. Frasinski, H. G. Muller, and M. J. J. Vrakking. Attosecond angle-resolved photoelectron spectroscopy. *Phys. Rev. Lett.*, 91(22), 2003.

[11] P. Tzallas, D. Charalambidis, N. A. Papadogiannis, K. Witte, and G. D. Tsakiris. Direct observation of attosecond light bunching. *Nature*, 426(6964):267–271, 2003.

[12] R. Kienberger, E. Goulielmakis, M. Uiberacker, A. Baltuska, V. Yakovlev, F. Bammer, A. Scrinizi, Th. Westerwalbesloh, U. Kleineberg, U. Heinzmann, M. Drescher, and F. Krausz. Atomic transient recorder. *Nature*, 427:817–821, 2004.

[13] G. G. Paulus, F. Grasbon, H. Walther, P. Villoresi, M. Nisoli, S. Stagira, E. Priori, and S. De Silvestri. Absolute-phase phenomena in photoionization with few-cycle laser pulses. *Nature*, 414(6860):182–184, 2001.

[14] A. Baltuška, T. Udem, M. Uiberacker, M. Hentschel, E. Goulielmakis, C. Gohle, R. Holzwarth, V. S. Yakoviev, A. Scrinzi, T. W. Hänsch, and F. Krausz. Attosecond control of electronic processes by intense light fields. *Nature*, 421(6923):611–615, 2003.

[15] G. G. Paulus, F. Lindner, H. Walther, A. Baltuška, E. Goulielmakis, M. Lezius, and F. Krausz. Measurement of the phase of few-cycle laser pulses. *Phys. Rev. Lett.*, 91 (25), 2003.

[16] J. Seres, A. Muller, E. Seres, K. O'Keeffe, M. Lenner, R. F. Herzog, D. Kaplan, C. Spielmann, and F. Krausz. Sub-10-fs, terawatt-scale Ti:sapphire laser system. *Opt. Lett.*, 28(19):1832–1834, 2003.

[17] D. Batani, C. J. Joachain, S. Martellucci, and A. N. Chester, editors. *Atoms, Solids and Plasmas in Super-Intense Laser-Fields.* Kluwer Academic/Plenum Publishers, New York, 2001.

[18] J. H. Posthumus and J. F. McCann. *Molecules and Clusters in Intense Laser Fields.* Cambridge University Press, Cambridge, 2001.

[19] P. Agostini, F. Fabre, G. Mainfray, G. Petite, and N. K. Rahman. Free-free transitions following six-photon ionization of xenon atoms. *Phys. Rev. Lett.*, 42(17): 1127–1130, 1979.

[20] D. N. Fittinghoff, P. R. Bolton, B. Chang, and K. C. Kulander. Observation of nonsequential double ionization of helium with optical tunneling. *Phys. Rev. Lett.*, 69(18):2642–2645, 1992.

[21] T. Weber, H. Giessen, M. Weckenbrock, G. Urbasch, A. Staudte, L. Spielberger, O. Jagutzki, V. Mergel, M. Vollmar, and R. Dörner. Correlated electron emission in multiphoton double ionization. *Nature*, 405(6787):658–661, 2000.

[22] A. McPherson, G. Gibson, H. Jara, U. Johann, T. S. Luk, I. A. McIntyre, K. Boyer, and C. K. Rhodes. Studies of multiphoton production of vacuum-ultraviolet radiation in the rare gases. *J. Opt. Soc. Am. B: Opt. Phys.*, 4(4):595–601, 1987.

[23] M. Ferray, A. L'Huillier, X. F. Li, L. A. Lompré, G. Mainfray, and C. Manus. Multiple-harmonic conversion of 1064 nm radiation in rare gases. *J. Phys. B: At. Mol. Opt. Phys.*, 21(3):L31–L35, 1988.

[24] P. H. Bucksbaum, A. Zavriyev, H. G. Muller, and D. W. Schumacher. Softening of the H_2^+ molecular bond in intense laser fields. *Phys. Rev. Lett.*, 64(16):1883–1886, 1990.

[25] A. Giusti-Suzor, X. He, O. Atabek, and F. H. Mies. Above-threshold dissociation of H_2^+ in intense laser fields. *Phys. Rev. Lett.*, 64(5):515–518, 1990.

[26] A. Giusti-Suzor, F. H. Mies, L. F. DiMauro, E. Charron, and B. Yang. Dynamics of H_2^+ in intense laser fields. *J. Phys. B: At. Mol. Opt. Phys.*, 28(3):309–339, 1995.

[27] L. J. Frasinski, J. H. Posthumus, J. Plumridge, K. Codling, P. F. Taday, and A. J. Langley. Manipulation of bond hardening in H_2^+ by chirping of intense femtosecond laser pulses. *Phys. Rev. Lett.*, 83(18):3625–3628, 1999.

[28] K. Sändig, H. Figger, and T. W. Hänsch. Dissociation dynamics of H_2^+ in intense laser fields: Investigation of photofragments from single vibrational levels. *Phys. Rev. Lett.*, 85(23):4876–4879, 2000.

[29] J. H. Posthumus, J. Plumridge, M. K. Thomas, K. Codling, L. J. Frasinski, A. J. Langley, and P. F. Taday. Dynamic and geometric laser-induced alignment of molecules in intense laser fields. *J. Phys. B: At. Mol. Opt. Phys.*, 31(13):L553–L562, 1998.

[30] R. Numico, A. Keller, and O. Atabek. Intense-laser-induced alignment in angularly resolved photofragment distributions of H_2^+. *Phys. Rev. A*, 60(1):406–413, 1999.

[31] F. Rosca-Pruna, E. Springate, H. L. Offerhaus, M. Krishnamurthy, N. Farid, C. Nicole, and M. J. J. Vrakking. Spatial alignment of diatomic molecules in intense laser fields: I. Experimental results. *J. Phys. B: At. Mol. Opt. Phys.*, 34(23): 4919–4938, 2001.

[32] H. Stapelfeldt and T. Seideman. Colloquium: Aligning molecules with strong laser pulses. *Rev. Mod. Phys.*, 75(2):543–557, 2003.

[33] M. Schmidt, D. Normand, and C. Cornaggia. Laser-induced trapping of chlorine molecules with picosecond and femtosecond pulses. *Phys. Rev. A*, 50(6):5037–5045, 1994.

[34] T. Seideman, M. Y. Ivanov, and P. B. Corkum. Role of electron localization in intense-field molecular ionization. *Phys. Rev. Lett.*, 75(15):2819–2822, 1995.

[35] J. H. Posthumus, L. J. Frasinski, A. J. Giles, and K. Codling. Dissociative ionization of molecules in intense laser fields: a method of predicting ion kinetic energies and appearance intensities. *J. Phys. B: At. Mol. Opt. Phys.*, 28(10):L349–L353, 1995.

[36] T. Zuo and A. D. Bandrauk. Charge-resonance-enhanced ionization of diatomic molecular-ions by intense lasers. *Phys. Rev. A*, 52(4):R2511–R2514, 1995.

[37] P. B. Corkum. Plasma perspective on strong-field multiphoton ionization. *Phys. Rev. Lett.*, 71(13):1994–1997, 1993.

[38] H. Niikura, F. Légaré, R. Hasbani, A. D. Bandrauk, M. Y. Ivanov, D. M. Villeneuve, and P. B. Corkum. Sub-laser-cycle electron pulses for probing molecular dynamics. *Nature*, 417(6892):917–922, 2002.

[39] C. Trump, H. Rottke, and W. Sandner. Strong-field photoionization of vibrational ground-state H_2^+ and D_2^+ molecules. *Phys. Rev. A*, 60(5):3924–3928, 1999.

[40] A. Staudte, C. L. Cocke, A. H. Prior, A. Belkacem, C. Ray, H. W. Chong, T. E. Glover, R. W. Schoenlein, and U. Saalmann. Observation of a nearly isotropic, high-energy Coulomb explosion group in the fragmentation of D_2 by short laser pulses. *Phys. Rev. A*, 65(2):020703, 2002.

[41] H. Niikura, F. Légaré, R. Hasbani, M. Y. Ivanov, D. M. Villeneuve, and P. B. Corkum. Probing molecular dynamics with attosecond resolution using correlated wave packet pairs. *Nature*, 421(6925):826–829, 2003.

[42] J. H. Posthumus and J. F. McCann. Diatomic molecules in intense laser fields. In J. H. Posthumus, editor, *Molecules and Clusters in Intense Laser Fields*, pages 27–83. Cambridge University Press, Cambridge, 2001.

[43] I. D. Williams, P. McKenna, B. Srigengan, I. M. G. Johnston, W. A. Bryan, J. H. Sanderson, A. El-Zein, T. R. J. Goodworth, W. R. Newell, P. F. Taday, and A.. J. Langley. Fast-beam study of H_2^+ ions in an intense femtosecond laser field. *J. Phys. B: At. Mol. Opt. Phys.*, 33(14):2743–2752, 2000.

[44] A. Kondorskiy and H. Nakamura. Photodissociation of H_2^+ and HD^+ in an intense laser field. *Phys. Rev. A*, 66(5):053412, 2002.

[45] V. N. Serov, A. Keller, O. Atabek, and N. Billy. Quantitative theory-versus-experiment comparison for the intense laser dissociation of H_2^+. *Phys. Rev. A*, 68(5): 053401, 2003.

[46] A. Kiess. *Elementare Moleküle in intensiven ultrakurzen Laserlichtpulsen - Experimentale Untersuchung an HD^+*. Diploma thesis, Ludwig-Maximilians-Universität München, 2003.

[47] A. D. Bandrauk, editor. *Molecules in Laser Fields*. Marcel Dekker, Inc., New York, 1994.

[48] L. D. Landau and E. M. Lifshits. *Quantum Mechanics: Non-Relativistic Theory*. Pergamon Press, Oxford; New York, 1977.

[49] M. H. Mittleman. *Introduction to the Theory of Laser-Atom Interactions*. Plenum Press, New York, 1993.

[50] D. R. Bates. The oscillator strength of H_2^+, $1s\sigma - 2p\sigma$. *J. Chem. Phys.*, 19(9): 1122–1124, 1951.

[51] C. Cohen-Tannoudji, J. Dupont-Roc, and G. Grynberg. *Atom-Photon Interactions: Basic Processes and Applications*. Wiley, New York, 1992.

[52] N. M. Kroll and K. M. Watson. Inelastic atom-atom scattering within an intense laser beam. *Phys. Rev. A*, 13(3):1018–1033, 1976.

[53] A. M. F. Lau. Radiative-dressed molecules: *Ab initio* theory and single/multiphoton dissociation with electronic transitions. *Phys. Rev. A*, 16(4):1535–1542, 1977.

[54] A. D. Bandrauk and M. L. Sink. Photodissociation in intense laser fields: Predissociation analogy. *J. Chem. Phys.*, 74(2):1110–1117, 1981.

[55] S. I. Chu. Floquet theory and complex quasivibrational energy formalism for intense field molecular photodissociation. *J. Chem. Phys.*, 75(5):2215–2221, 1981.

[56] J. H. Shirley. Solution of the Schrödinger equation with a Hamiltonian periodic in time. *Phys. Rev.*, 138(4B):B979–B987, 1965.

[57] F. Rebentrost. Private communication.

[58] T. E. Sharp. Potential-energy curves for molecular hydrogen and its ions. *Atomic Data*, 2:119–169, 1971.

[59] C. Wunderlich. *Licht-induzierte molekulare Struktur*. PhD thesis, Ludwig-Maximilians-Universität München, 1995.

[60] R. S. Mulliken. Intensities of electronic transitions in molecular spectra. II. charge-transfer spectra. *J. Chem. Phys.*, 7:20–34, 1939.

[61] E. E. Aubanel, J. M. Gauthier, and A. D. Bandrauk. Molecular stabilization and angular distribution in photodissociation of H_2^+ in intense laser fields. *Phys. Rev. A*, 48(3):2145–2152, 1993.

[62] A. Giusti-Suzor and F. H. Mies. Vibrational trapping and suppression of dissociation in intense laser fields. *Phys. Rev. Lett.*, 68(26):3869–3872, 1992.

[63] G. H. Yao and S. I. Chu. Laser-induced molecular stabilization and trapping and chemical bond hardening in intense laser fields. *Chem. Phys. Lett.*, 197(4-5):413–418, 1992.

[64] A. Zavriyev, P. H. Bucksbaum, J. Squier, and F. Saline. Light-induced vibrational structure in H_2^+ and D_2^+ in intense laser fields. *Phys. Rev. Lett.*, 70(8):1077–1080, 1993.

[65] A. Zavriyev, P. H. Bucksbaum, H. G. Muller, and D. W. Schumacher. Ionization and dissociation of H_2 in intense laser fields at 1.064 μm, 532 nm, and 355 nm. *Phys. Rev. A*, 42(9):5500–5513, 1990.

[66] G. Jolicard and O. Atabek. Above-threshold-dissociation dynamics of H_2^+ with short intense laser pulses. *Phys. Rev. A*, 46(9):5845–5855, 1992.

[67] R. Numico, A. Keller, and O. Atabek. Laser-induced molecular alignment in dissociation dynamics. *Phys. Rev. A*, 52(2):1298–1309, 1995.

[68] L. V. Keldysh. Ionization in the field of a strong electromagnetic wave. *Sov. Phys.-JETP*, 20:1018, 1965.

[69] D. Bauer and P. Mulser. Exact held ionization rates in the barrier-suppression regime from numerical time-dependent Schrödinger-equation calculations. *Phys. Rev. A*, 59 (1):569–577, 1999.

[70] T. Zuo and A. D. Bandrauk. Harmonic generation by the H_2^+ molecular ion in intense laser fields. *Phys. Rev. A*, 48(5):3837–3844, 1993.

[71] H. T. Yu, T. Zuo, and A. D. Bandrauk. Intense field ionization of molecules with ultra-short laser pulses—enhanced ionization and barrier-suppression effects. *J. Phys. B: At. Mol. Opt. Phys.*, 31(7):1533–1551, 1998.

[72] S. Chelkowski, T. Zuo, O. Atabek, and A. D. Bandrauk. Dissociation, ionization, and Coulomb explosion of H_2^+ in an intense laser field by numerical integration of the time-dependent Schrödinger equation. *Phys. Rev. A*, 52(4):2977–2983, 1995.

[73] M. Plummer and J. F. McCann. Field-ionization rates of the hydrogen molecular ion. *J. Phys. B: At. Mol. Opt. Phys.*, 29(20):4625–4640, 1996.

[74] L. B. Madsen, M. Plummer, and J. F. McCann. Multiphoton ionization of H_2^+ by intense light: A comparison of Floquet and wave-packet results. *Phys. Rev. A*, 58 (1):456–465, 1998.

[75] D. Dundas. Efficient grid treatment of the ionization dynamics of laser-driven H_2^+. *Phys. Rev. A*, 65(2), 2002.

[76] S. Chelkowski, A. Conjusteau, T. Zuo, and A. D. Bandrauk. Dissociative ionization of H_2^+ in an intense laser field: Charge-resonance-enhanced ionization, Coulomb explosion, and harmonic generation at 600 nm. *Phys. Rev. A*, 54(4):3235–3244, 1996.

[77] S. Chelkowski, C. Foisy, and A. D. Bandrauk. Electron-nuclear dynamics of multiphoton H_2^+ dissociative ionization in intense laser fields. *Phys. Rev. A*, 57(2):1176–1185, 1998.

[78] T. D. G. Walsh, F. A. Ilkov, S. L. Chin, F. Châteauneuf, T. T. Nguyen-Dang, S. Chelkowski, A. D. Bandrauk, and O. Atabek. Laser-induced processes during the Coulomb explosion of H_2 in a Ti-sapphire laser pulse. *Phys. Rev. A*, 58(5):3922–3933, 1998.

[79] B. Feuerstein and U. Thumm. Fragmentation of H_2^+ in strong 800-nm laser pulses: Initial-vibrational-state dependence. *Phys. Rev. A*, 67(4), 2003.

[80] W. Ketterle. *Spektroskopie an Heliumhydrid und am dreiatomigen Wasserstoffmolekül.* PhD thesis, Ludwig-Maximilians-Universität München, 1986.

[81] C. Wunderlich, V. Betz, R. Bruckmeier, and H. Figger. Lifetime measurements on ArH and ArD. *J. Chem. Phys.*, 98(12):9362–9371, 1993.

[82] R. Bruckmeier, C. Wunderlich, and H. Figger. New experimental insight into the ground state potential surface of triatomic hydrogen. *Phys. Rev. Lett.*, 72(16):2550–2553, 1994.

[83] C. Wunderlich, H. Figger, and T. W. Hänsch. Ar_2^+ molecules in intense laser fields. *Chem. Phys. Lett.*, 256(1-2):43–50, 1996.

[84] C. Wunderlich, E. Kobler, H. Figger, and T. W. Hänsch. Light-induced molecular potentials. *Phys. Rev. Lett.*, 78(12):2333–2336, 1997.

[85] C. Wunderlich, H. Figger, and T. W. Hänsch. Tunneling through light-induced molecular potentials in Ar_2^+. *Phys. Rev. A*, 62(2):023401, 2000.

[86] K. Sändig. *H_2^+ in intensiven Lichtfeldern.* PhD thesis, Ludwig-Maximilians-Universität München, 2000.

[87] H. Liebl and W.W. Harrison. Study of an iodine discharge in a duoplasmatron (ion source). *Int. J. Mass spectrom.*, 22(3-4):237–246, 1976.

[88] H. Zhang. *Ion Sources.* Science Press, Beijing, 1999.

[89] F. von Busch and G. H. Dunn. Photodissociation of H_2^+ and D_2^+: Experiment. *Phys. Rev. A*, 5(4):1726–1743, 1972.

[90] W. Koot, W. J. van der Zande, and D. P. de Bruijn. Rotational distribution of H_2^+ ions produced by 90 eV electron impact. *Chem. Phys.*, 115(2):297–305, 1987.

[91] H. Helm and P. C. Cosby. Photodissociation measurement of rovibrational energies and populations of molecules in fast beams. *J. Chem. Phys.*, 86(12):6813–6822, 1987.

[92] N.P.F.B. van Asselt, J. G. Maas, and J. Los. Laser induced photodissociation of H_2^+ and D_2^+ ions. *Chem. Phys.*, 5(3):429–438, 1974.

[93] J. I. Steinfeld. *Molecules and Radiation: An Introduction to Modern Molecular Spectroscopy.* MIT Press, Cambridge, Mass., 2. edition edition, 1985.

[94] R. N. Bracewell. *The Fourier Transform and Its Applications.* McGraw Hill, Boston, 2000.

[95] L. M. Smith and D. R. Keefer. Abel inversion using transform techniques. *J. Quant. Spectrosc. Radiat. Transf.*, 39(5):367–373, 1988.

[96] K. van Niekerk and A. Eppink. Abelflex512, 1996.

[97] V. Dribinski, A. Ossadtchi, V. A. Mandelshtam, and H. Reisler. Reconstruction of Abel-transformable images: The Gaussian basis-set expansion Abel transform method. *Rev. Sci. Instrum.*, 73(7):2634–2642, 2002.

[98] M. J. J. Vrakking. An iterative procedure for the inversion of two-dimensional ion/photoelectron imaging experiments. *Rev. Sci. Instrum.*, 72(11):4084–4089, 2001.

[99] A. G. Suits and R. E. Continetti. *Imaging in Chemical Dynamics.* American Chemical Society, Washington, D.C., 2001.

[100] M. von Ardenne. *Elektronenphysik, Übermikroskopie, Ionenphysik.* Deutscher Verlag der Wissenschaften, Berlin, 1962.

[101] D. E. Spence, P. N. Kean, and W. Sibbett. 60-fsec pulse generation from a self-mode-locked Ti:sapphire laser. *Opt. Lett.*, 16(1):42–44, 1991.

[102] D. Strickland and G. Mourou. Compression of amplified chirped optical pulses. *Opt. Commun.*, 56(3):219–221, 1985.

[103] J. C. Diels and W. Rudolph. *Ultrashort Laser Pulse Phenomena: Fundamentals, Techniques, and Applications on a Femtosecond Time Scale.* Academic Press, San Diego, 1996.

[104] A. E. Siegman, M. W. Sasnett, and T. F. Johnston. Choice of clip levels for beam width measurements using knife-edge techniques. *IEEE J. Quantum Electron.*, 27 (4):1098–1104, 1991.

[105] W. T. Silfvast. *Laser Fundamentals.* Cambridge University Press, New York, 1996.

[106] A. E. Siegman. *Lasers.* University Science Books, Mill Valley, California, 1986.

[107] V. Serov. *Photodissociation dynamics in laser fields: Quantitative interpretation of experimental data on NO_2 and H_2^+.* PhD thesis, Université Paris XI, U.F.R. Scientifique d'Orsay and St. Petersburg State University, 2003.

[108] K.P. Huber and G. Herzberg. *Constants of Diatomic Molecules*, volume Vol.4. Van Nostrand Reinhold, New York, 1979.

[109] G. N. Gibson, M. Li, C. Guo, and J. Neira. Strong-field dissociation and ionization of H_2^+ using ultrashort laser pulses. *Phys. Rev. Lett.*, 79(11):2022–2025, 1997.

[110] I. V. Litvinyuk, K. F. Lee, P. W. Dooley, D. M. Rayner, D. M. Villeneuve, and P. B. Corkum. Alignment-dependent strong field ionization of molecules. *Phys. Rev. Lett.*, 90(23), 2003.

[111] S. Chelkowski. Private communication, 2001.

[112] E. Constant, H. Stapelfeldt, and P. B. Corkum. Observation of enhanced ionization of molecular ions in intense laser fields. *Phys. Rev. Lett.*, 76(22):4140–4143, 1996.

[113] C. Trump, H. Rottke, and W. Sandner. Multiphoton ionization of dissociating D_2^+ molecules. *Phys. Rev. A*, 59(4):2858–2863, 1999.

[114] A. Kiess, D. Pavičić, T. W. Hänsch, and H. Figger. Manuscript in preparation.

[115] H. Hasegawa, A. Hishikawa, and K. Yamanouchi. Coincidence imaging of Coulomb explosion of CS_2 in intense laser fields. *Chem. Phys. Lett.*, 349(1-2):57–63, 2001.

[116] H. Stapelfeldt, E. Constant, and P. B. Corkum. Wave packet structure and dynamics measured by Coulomb explosion. *Phys. Rev. Lett.*, 74(19):3780–3783, 1995.

[117] S. Chelkowski, P. B. Corkum, and A. D. Bandrauk. Femtosecond Coulomb explosion imaging of vibrational wave functions. *Phys. Rev. Lett.*, 82(17):3416–3419, 1999.

[118] A. D. Bandrauk, S. Chelkowski, and I. Kawata. Molecular above-threshold-ionization spectra: The effect of moving nuclei. *Phys. Rev. A*, 67(1):013407, 2003.

[119] J. Ullrich, R. Moshammer, R. Dörner, O. Jagutzki, V. Mergel, H. Schmidt-Böcking, and L. Spielberger. Recoil-ion momentum spectroscopy. *J. Phys. B: At. Mol. Opt. Phys.*, 30(13):2917–2974, 1997.

[120] H. Rottke, C. Trump, M. Wittmann, G. Korn, W. Sandner, R. Moshammer, A. Dorn, C. D. Schroter, D. Fischer, J. R. C. Lopez-Urrutia, P. Neumayer, J. Deipenwisch, C. Hohr, B. Feuerstein, and J. Ullrich. Coincident fragment detection in strong field photoionization and dissociation of H_2. *Phys. Rev. Lett.*, 89(1):013001, 2002.

[121] T. Zuo, A. D. Bandrauk, and P. B. Corkum. Laser-induced electron diffraction: a new tool for probing ultrafast molecular dynamics. *Chem. Phys. Lett.*, 259(3-4): 313–320, 1996.

[122] S. Cohen, J. R. Hiskes, and R. J. Riddell. Vibrational states of the hydrogen molecular ion. *Phys. Rev.*, 119(3):1025–1027, 1960.

[123] G. H. Dunn. Franck-Condon factors for ionization of H_2 and D_2. *J. Chem. Phys.*, 44 (7):2592–2594, 1966.

Acknowledgments

This research was conducted at Max Planck Institute of Quantum Optics in Garching. I would like to thank all those who have helped me to complete this work in every possible way.

First of all, I want to express my gratitude to *Prof. Dr. Theodor W. Hänsch* for affording me the opportunity of pursuing my Ph.D. thesis in his group. I am indebted to him for generously providing funds for this work and for giving me the chance to present my results at various conferences. His ingenuity, enthusiasm and extreme kindness will always be in my memory. I am truly honoured that I could work in his outstanding group.

I am grateful to my advisor, *Dr. Hartmut Figger*, for inviting me to work on this interesting project. I thank him for his invaluable support, continuous encouragement and everlasting optimism. His friendly suggestions were helpful in many ways during my stay in Germany. I appreciate his ideas and criticism, from which I have learned a lot. His reviews and suggestions for improving the manuscript of this thesis are gratefully acknowledged.

I am deeply indebted to my predecessor, *Dr. Karsten Sändig*, for introducing me to the experimental setup and for being very helpful at the beginning of my work. Karsten has taught me a lot about the femtosecond system and the ion beam apparatus, without which it would be difficult to imagine the ensuing work. I thank him for his kindness and for answering my many questions, also after he had left our group.

I thank *Andreas Kiess* for his friendly help and assistance in the experiments, numerous technical improvements and many helpful comments and discussions. It was gratifying to learn from him and have the chance to explain to him what I know. Most of all, I thank him for the pleasant time I had working with him.

I am deeply indebted to *Wolfgang Simon* and *Karl Linner* for their skilful technical assistance and their willingness to help me in every situation. They always understood my needs and gave their best to find excellent solutions in the shortest time, which often seemed impossible. My gratitude also goes to *Helmut Brückner* for his help concerning electronics, for the devices he lent me and for a great deal of advice. I thank them for greatly improving the experiment and safety in the lab.

A special word of thanks goes to *Dr. Frank Rebentrost*, who performed many invaluable calculations for me. I wish to thank him for his numerous explanations and illuminating discussions.

I thank *Dr. Osman Atabek* and *Dr. Vassili Serov* from CNRS, Orsáy for very good

cooperation. Their calculations, insightful explanations and fruitful discussions were most beneficial.

I am deeply indebted to *Dr. Marc Vrakking* for providing me with his inversion algorithm and helping me with its implementation. Thanks also go to *Prof. Dr. Peter Rakitzis* and *Dr. Vladimir Dribinski* for offering me their inversion programs and support.

I am grateful to *Prof. Dr. Gerhard G. Paulus* for his kind explanations, suggestions and for lending me some optical elements.

I am indebted to *Hans-Jürgen Hechler* and *Friedrich Staudt* from Spectra Physics for their technical support, help and advice concerning the laser system.

Thanks to *Dr. Astrid Müller* for her kind help and some very useful tips regarding the laser system.

I am grateful to *Maximilian Herrmann* for proofreading this thesis and making invaluable suggestions.

I would like to thank *Birgit Henrich* for being my roommate, for her nice company and for helping me with German.

I am extremely thankful to our secretary, *Rosemarie Lechner*, for her kindness, continuous help and for taking care of many important matters. I specially thank her for her engagement with my accommodation. My thanks to *Gabriele Gschwendtner* for always being so kind and extremely helpful in making appointments.

I also warmly thank all those nice people at MPQ who helped me in one way or another.

I would like to thank all the colleagues in our group: *Peter Fendel*, *Sebastian Fray*, *Christoph Gohle*, *Birgit Henrich*, *Dr. Ronald Holzwarth*, *Dr. Nikolai Kolachevsky*, *Philipp Kubina*, *Dr. Thomas Udem*, *Dr. Jochen Walz* and *Marcus Zimmermann*. This also includes former and visiting members: *Christina Alvarez-Diez*, *Dr. Francesco Cataliotti*, *Giovanni Cennini*, *Dr. Kjeld Eikema*, *Marc Fischer*, *Dr. Xiaoming Gao*, *Dr. Savely Karshenboim*, *Matthias König*, *Dr. Michael Mei*, *Dr. Síle Nic Chormaic*, *Dr. Markus Niering*, *Claudia Nießl*, *Dr. Anette Pahl*, *Dr. Randolf Pohl*, *Dr. Jörg Reichert*, *Dr. Reinard Scheunemann*, *Andreas Voigt* and *Prof. Dr. Martin Weitz*. With all of them I had a very pleasant time at MPQ and particularly at our seminars at Ringberg Castle. I thank them for their kindness, help and support, including the part of our group at Ludwig-Maximilians University, Munich.

It is my great pleasure to thank my Croatian friends in Munich: *Tanja Bizjak*, *Nils Paar*, *Hrvoje Skenderović*, *Bojan Pečnik* and *Petar Mimica* for all the experiences we have shared. I thank them for their precious support and a connection with my home. Special thanks to *Hrvoje* for his pleasant company at MPQ and his precious help.

I am deeply grateful to my parents, *Marijana* and *Mile*, and brother *Danijel* for their great care, everlasting support and love. I thank them for believing in me and for everything they have done for me during my stay in Germany. Warm thanks also go to my relatives and friends for their interest and support.

Finally, I would like to give my special thanks to *Helena* for coming into my life, and making it a really happy one. I wish I could thank her enough for her endless love and kindness, and for her all optimism, encouraging support and patience.

Curriculum Vitae

Domagoj Pavičić

4/10/1975	Born in Zagreb, Croatia
09/1982 – 06/1990	Elementary school in Zagreb, Croatia
09/1990 – 06/1994	High school, XV. gimnazija in Zagreb, Croatia
10/1994 – 11/1999	Study of physics at the University of Zagreb, Faculty of Science, Zagreb, Croatia
04/1999 – 11/1999	Diploma work at the Institute of Physics, Zagreb, Croatia, group of Dr. G. Pichler Thesis title: "Modulation Spectroscopy of Neon Plasma" Thesis advisor: Prof. Dr. D. Veža
01/2000 – 03/2004	Ph.D. work at Max Planck Institute of Quantum Optics in Garching, Germany, group of Prof. Dr. T. W. Hänsch Thesis title: "Coulomb Explosion and Intense-Field Photodissociation of Ion-Beam H_2^+ and D_2^+ " Thesis advisors: Dr. H. Figger and Prof. Dr. T. W. Hänsch